THE FABRICATION OF THIN-WALLED STEEL ALLOYS THROUGH THE GAS CARBURIZATION OF REDUCED METAL OXIDE EXTRUSIONS

A Thesis
Presented to
The Academic Faculty

by

Laura B. Cerully

In Partial Fulfillment
of the Requirements for the Degree
Doctor of Philosophy in the
School of Materials Science and Engineering

Georgia Institute of Technology
August 2010

THE FABRICATION OF THIN-WALLED STEEL ALLOYS THROUGH THE GAS CARBURIZATION OF REDUCED METAL OXIDE EXTRUSIONS

Approved by:

Dr. Thomas H. Sanders, Jr., Advisor
School of Materials Science and Engineering
Georgia Institute of Technology

Dr. Joe K. Cochran
School of Materials Science and Engineering
Georgia Institute of Technology

Dr. Preet Singh
School of Materials Science and Engineering
Georgia Institute of Technology

Dr. Naresh Thadhani
School of Materials Science and Engineering
Georgia Institute of Technology

Dr. David McDowell
George W. Woodruff School of Mechanical Engineering
Georgia Institute of Technology

Date Approved: April 21, 2010

Dedicated to my family

ACKNOWLEDGEMENTS

I'd like to express my appreciation and a sincere thank you (though it doesn't seem to be enough) to my advisor, Dr. Sanders, for his guidance through the past five years. His support, confidence in my abilities, and encouragement do not go unnoticed, and he has made my graduate experience incredibly fulfilling. I also want to express my gratitude to Dr. Cochran, Dr. Speyer Dr. Singh and Dr. Thadhani for all of their knowledge and support in the lab. I am grateful to all of my committee members for their wisdom and for taking part in this process with me. I also want to express my appreciation to all of the office staff, especially Susan Bowman, who have made the administrative stresses associated with graduation, coursework, travel and everything in between seem to just go away.

I want to recognize my fellow graduate students who have made this both a learning and fun experience. I am grateful for the lifelong friendship that I have built with many of you. Michael Middlemas and Tammy McCoy have been endless sources of help to me, and I'm so appreciative of their guidance. I am thankful for every member of the Sanders and Cochran groups who have made most every day interesting.

This work is funded by a NIST ATP Grant with Deep Springs Technology, (Toledo, OH), Contract #70NANB7H7024. I'd like to extend my gratitude to everyone at Deep Springs Technology for the collaboration on this project. A special thanks is necessary for the financial contribution that allowed me to travel to the INNOVATE 2009 Conference. It was a trip I will never forget and was an incredible learning experience. I also want to acknowledge the Paper Science and Engineering program at Georgia Tech for providing me with funding through the Otto Kress Scholarship.

Last, but certainly not least, I want to thank my family for their love and the never-ending support that they have given me throughout my entire life. My mom and dad have

been the best parents a girl could ask for. I'm glad to be a "chip off the 'ol' block," Pops. Mom, thank you for listening every time I called to unload my stress on someone, especially since you think its not often enough! To my sisters, Jenn and Kate, it is great to have sisters who I am so close to and who understand the life of the Ph.D. student too! David, I can't thank you enough for every word of encouragement and the endless votes of confidence that you have given me when my own has waivered. You are all so special to me.

TABLE OF CONTENTS

LIST OF TABLES

LIST OF FIGURES

SUMMARY

Investigations of the production of thin-walled steel alloys through the reduction and subsequent gas carburization of structures made from metal oxide powders were performed. Batch compositions, as well as the heat treatment parameters necessary for the formation of structures with the compositions of 4140 and 316 steel without carbon, were determined through the use of thermogravimetric analysis, dilatometric measurements, and microstructural investigation.

Parameters for the high temperature carburization of thin tape of 250-300 μm thickness, as well as hollow metal spheres with 4140 composition, in a CO/CO_2 atmosphere were determined using thermodynamic data and experimental work. The research has shown that the amount of carbon in the walls of the structures can be controlled and uniform carbon contents across the cross-sections can be achieved in less than 30 minutes.

Heat treatments for carburized samples of 4140 composition were carried out using oil quench and salt bath furnaces. Mechanical property testing of heat-treated samples was carried out using Vickers microhardness testing, resulting in values similar to conventionally produced 4140 steel. Compression testing of carburized 4140 spheres was also performed, showing that crush strength of the spheres has been significantly improved through the carburization process. Studies on the decarburization behavior of similar alloys under various conditions were also performed in order to aid in the prediction of the microstructural behavior of samples during carburization and subsequent heat treatment.

Low temperature gas carburization of structures with 316 steel composition without carbon, has also been performed. Hardness variations present through the cross-section of the part after carburization suggest some transfer of carbon, though contents are not as high as anticipated. Suggestions for future work in this area are presented.

The results of these investigations yield a novel method for the production of steel parts from metal oxide powders. The speed and low cost of the process, coupled with the proven ability of the process to yield parts with similar microstructural and mechanical characteristics as conventionally made alloys, allows for the techniques presented in this study to be used for the development of alloys which could not be previously done economically.

CHAPTER I

INTRODUCTION

Advances in the formation of thin-walled metal honeycomb structures have allowed for the successful fabrication of linear cellular alloys (LCAs) in several material systems including, but not limited to, Fe-Ni-Cr [1–5], copper alloys [6], maraging steels [7, 8] and superalloys [8] through the extrusion and direct reduction of metal oxide powder mixtures. In addition, when the oxides of the metal of interest cannot be easily reduced, in the case of titanium for example, these elements can often be added through the use of metal-hydride powders, resulting in a wide range of alloys that can be manufactured through the process. Excellent compositional control of the parts has been demonstrated, and due to the high strength to weight ratios for some of the extrusion geometries used, the potential application of these materials is vast. For example, the high energy absorption capabilities of some of these alloys make the process favorable for transportation and defense related applications.

While many material systems have been created using this technique, one large restriction of the process is the inability to add carbon to the LCAs in the manner that is conventionally used to produce these structures. The ability to add carbon to these structures with precision greatly enhances the range of alloys which can be produced using the technology. Gas carburization is investigated in this study as an alloying technique for parts that are made via the reduction of metal oxide powder mixtures. Typically, gas carburization is a surface hardening technique, however, the thin-walled nature of these products allows for the adaptation of traditional techniques such that uniform carbon contents can be achieved through the cross-section of the walls of these structures. The success of this process will allow the use of LCA's as an alloy development tool, where large ranges of alloy compositions in various material systems which could otherwise not be investigated

economically can now be performed quickly and with low material costs.

One such phenomenon which occurs during gas carburization, known as metal dusting or sooting, is very important to this research. Metal dusting is a form of carburization that leads to the deterioration of the part. Metal dusting is typically not a major concern in traditional gas carburization processes, as parts are large in comparison to the extent of metal soot observed. However, the loss of material associated with metal dusting can ruin the integrity of a thin-walled structure, even if only small quantities are observed. Thus, the design of gas carburization experiments in this study are such that metal dusting is carefully avoided and thermodynamic considerations necessary for the avoidance of metal dusting are detailed.

While metal honeycomb structures could be used in many applications where a high strength to weight ratio is necessary, one such application, proppants, is the direct motivation for this research. Proppants are small spheres typically made of ceramic and glass materials that are used to enhance oil and gas recovery in fractured wells [9]. The ability to create ultra strong, light weight, metal proppants economically would allow for superior extraction compared to traditional proppants. First, the light weight nature of the proppants would allow further travel of the proppants into fissures and cracks in a well. Secondly, the mechanical properties of metal proppants, including increased ductility, are more suited to the application than current ceramic and glass technologies. Current proppants only allow the recovery of approximately 33% of available oil, thus this technology could greatly decrease the United States' dependence on foreign oil through improved recovery from existing wells on American soil.

While proppants have a spherical shape, rather than a honeycomb structure, variations on the same technology can be used to produce both geometries. In order to investigate the processing steps necessary for the gas carburization and subsequent heat treatment of proppants such that steel compositions can be achieved, extrusions of thin tape are used, which simulate the wall thickness that is desirable for hollow metal sphere proppants.

When investigating new alloys systems for use in proppants, several factors are necessary to keep in mind:

- The production must be economical, as proppants are not easily recovered, as they are crushed during usage.
- The proppants themselves must be able to withstand the highly corrosive environments that are observed during hydraulic fracturing.
- Superior mechanical properties to conventionally made glass and ceramics proppants must be achieved.

To satisfy these requirements, the production of a low alloy steel is of the highest interest to the manufacturing of proppants. Because slight changes in carbon content can significantly affect the strength and ductility of low alloy steels, it is necessary to determine the parameters necessary such that gas carburization can be used to reach carbon contents of low alloy steels with precision. In low alloy steels, compositions above approximately 0.7-0.8 wt% C are rarely exceeded. Thus, it is also the goal of this study to demonstrate that the gas carburization technique can be used to reach carbon contents above the eutectoid (0.7-0.8 wt% C) as well. In this study, a low alloy steel of 4140 composition is the key alloy of interest, though the process can be adapted easily for other low alloy steel compositions.

While the development of proppants is the direct motivation for this research, the processes which are investigated here can be adapted to the production of metal honeycomb structures with varying geometries as well as alloy composition fairly simply. Thus, the research moves to the investigation of gas carburization to produce steel alloys with significantly higher carbon contents. Specifically, an austenitic stainless steel with 316 composition is investigated. While cost limitations would likely prevent the use of 316 for proppants, the research moves in this direction in order to show the versatility of the process for the formation of products where these limitations are not as severe. It is expected that carbon contents up to approximately 3 wt% may be reached, using a gas carburization

process termed Low Temperature Colossal Supersaturation (LTCSS), also traditionally a surface hardening technique. Furthermore, the process is such that the formation of carbides that are detrimental to the mechanical and anti-corrosion properties of the steel is avoided.

The overall objective of the research is to demonstrate the ability to create thin-walled steel alloys of various compositions through the use of gas carburization of reduced metal oxide powder mixtures. Specifically, the following objectives will be addressed:

- To determine the parameters and materials necessary for the successful production of strip of iron, 4140 and 316 compositions.
- To determine gas carburization parameters such that the materials are carburized through the cross-section of the structures with repeatability, without the occurrence of metal dusting.
- To demonstrate the range of carbon compositions which may be reached through gas carburization of the alloys of interest.
- To determine the effect of heat treatment on the mechanical and microstructural properties of the carburized samples.

Thus, the research begins with the development of thin-walled structures of iron, and structures with 4140 and 316 compositions (without carbon) from metal-oxide powder mixtures. Specifically, extrusions of thin strip (approximately 250-300 μm thickness) are used in the research to mimic the wall thicknesses that are typically seen in LCAs, as well as thicknesses that may be used in the production of hollow spheres. Then, the research continues to the gas carburization of these structures at high temperatures for iron and 4140 compositions. Gas carburization is also investigated at low temperatures for structures with 316 composition. Heat treatment studies as well as mechanical property investigations of carburized samples are presented for comparison with conventionally fabricated alloys of

similar composition. Lastly, decarburization studies are presented as they are necessary for the understanding of the gas carburization processes presented.

CHAPTER II

BACKGROUND

The following section will discuss the background information necessary to understand the process of interest in this study. Figure 2.1 shows a schematic of this process where first, fabrication of thin-walled metal parts via the reduction and sintering of metal oxide powder extrusions must be understood. Next, the necessary information to understand the investigation of gas carburization as an alloying technique for thin-walled structures will be presented. Lastly, the alloys of interest to the study are summarized.

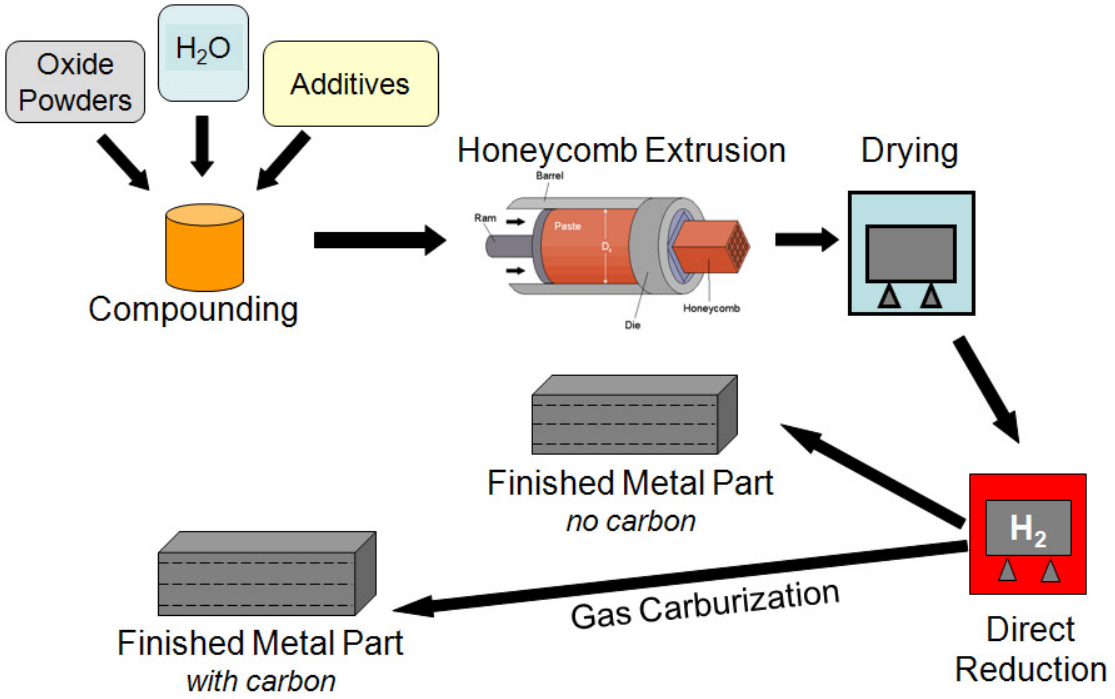

Figure 2.1: Schematic of the process of making thin-walled steel alloys through the extrusion of metal oxide powder pastes.

2.1 Fabrication of Metal Oxide Powder Extrusions

The fabrication of thin-walled extrusions from metal oxide powder mixtures has been thoroughly investigated. The following section will discuss the background information and current literature necessary to understand the process. Specifically, the information regarding paste preparation and extrusion as well as the reduction and sintering of the green extrusion to produce a metal part is detailed.

2.1.1 Paste Preparation and Shape Formation

In general, powders of metal oxide precursors are mixed with lubricant and a binder in proportion such that the final composition of interest is achieved, post-reduction of the oxides. The following method can be used to determine the amount of oxide necessary to achieve the desired composition post-reduction.

First, assume metal oxides of composition M_xO_y where $M_xO_y^i$ is the i^{th} oxide of a total of n number of oxides used in the fabrication of the alloy of interest. The metal yield from each oxide of interest (MY^i) can be determined through Equation 1.

$$MY^i = x^i \cdot \frac{MW_M^i}{MW_{M_xO_y}^i} \tag{1}$$

where MW_M^i and $MW_{M_xO_y}^i$ are the molecular weights of the metal and oxide, respectively.

From this information, the mass of each oxide ($M_{M_xO_y}^i$) necessary for a batch where there is m_{total} grams of *metal* can be determined from Equation 2.

$$M_{M_xO_y}^i = \frac{Wt\%_{M_{alloy}^i}}{100} \cdot \frac{m_{total}}{MY^i} \tag{2}$$

where $Wt\%_{M_{alloy}^i}$ is the weight percent of metal M^i desired in the final product.

To determine $M_{M_xO_y}^i$ for a batch of *oxide* powders of size m_{total}, the weight percent of each oxide ($Wt\%_{M_xO_y{}^i}$) must first be determined as shown in Equation 3. Then, Equation 4 can be used to determine the mass of each oxide necessary.

$$Wt\%_{M_xO_y{}^i} = \frac{M_{M_xO_y{}^i}}{\sum_{i=1}^{n} M_{M_xO_y{}^i}} \cdot 100 \tag{3}$$

$$M_{M_xO_y{}^i} = \frac{Wt\%_{M_xO_y{}^i}}{100} \cdot m_{total} \tag{4}$$

While the above equations are used to determine the mass of powders necessary for compositional control, Hurysz *et al*. [7] developed a model to determine the maximum solids loading allowable in the paste, such that paste properties optimal for extrusion are achieved. For example, maximum solids loading is necessary for the formation of a nearly defect-free extrusion such that the green part has sufficient strength to maintain its shape prior to subsequent processing steps. This information is thus used to determine the amount of liquid in the paste. Additionally, the size of the metal oxide powders used to make the extrusion pastes should be approximately 1/50th the size of the feature geometry such that the shapes can be extruded with precision [6].

2.1.2 Reduction and Sintering

The reduction of iron oxides through the use of hydrogen gas has been extensively studied [1, 2, 10–18]. Metal oxides are reduced in hydrogen following the thermodynamic considerations of the Ellingham diagram. An Ellingham diagram for several metal oxides is shown in Figure 2.2. For this study, investigations of the reduction of mixtures of iron and chromium oxides are most useful and will thus be detailed further. Figure 2.3 shows an Ellingham diagram for several iron and chromium oxides, along with the Gibbs free energy of formation of H_2O for differing ratios of the partial pressures of hydrogen to water vapor (P_{H_2}/P_{H_2O}).

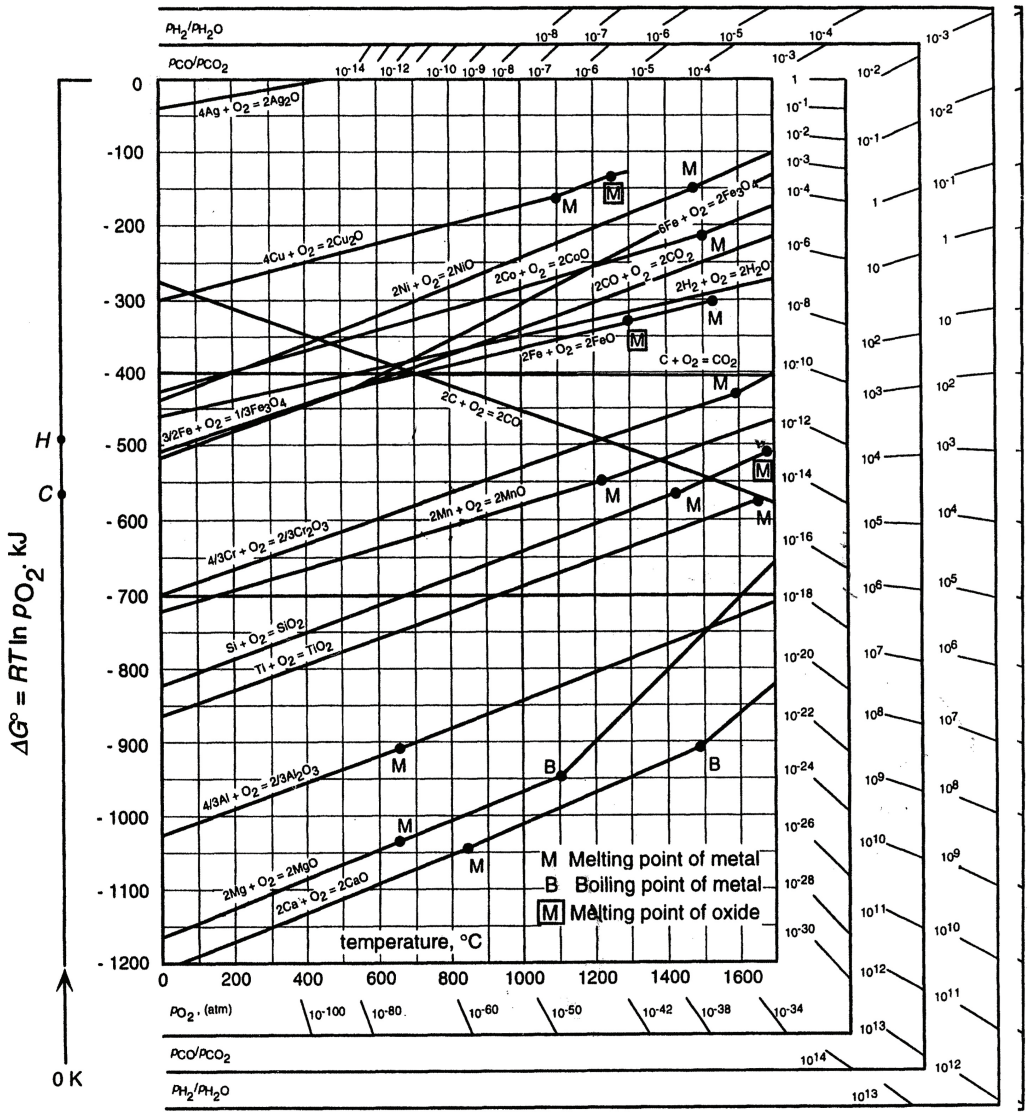

Figure 2.2: Ellingham diagram of several metal oxides [19].

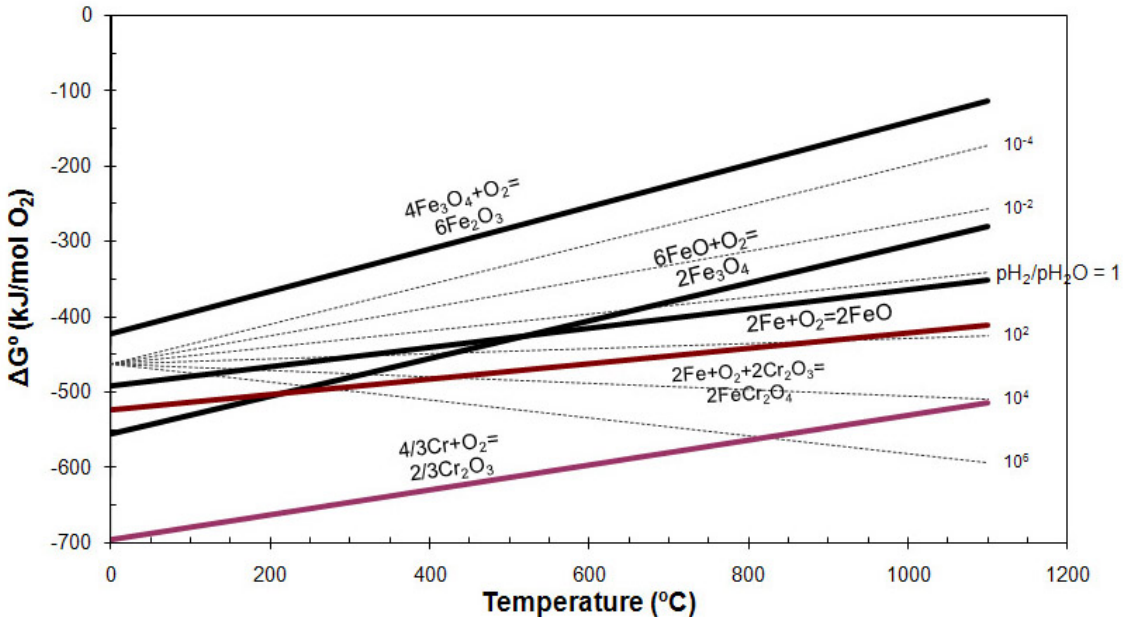

Figure 2.3: Ellingham diagram of iron and chromium oxides, including differing values of P_{H_2}/P_{H_2O}, as calculated from Kubaschewski [20] and Gaskell [19].

It can be seen in Figure 2.3 that the reduction of Cr_2O_3 requires very high P_{H_2}/P_{H_2O} values. Furthermore, the addition of Cr_2O_3 to Fe_2O_3 has been shown to delay the sintering of Fe_2O_3 to pure iron. However, it has also been noted that the addition of iron aids in the reduction of chromia as Cr particles may diffuse into the iron matrix [2, 21]. Research by Nadler et al. [1, 3] found that upon heating in hydrogen, pure Fe_2O_3 can be fully reduced by approximately 525°C and sintered by approximately 1275°C when heated at a rate of 5°C/min. Fe_2O_3 reduces following Equation 5.

$$Fe_2O_3 \longrightarrow Fe_3O_4 \longrightarrow FeO \longrightarrow Fe \tag{5}$$

Nadler [1, 3] used dilatometric and thermogravimetric analysis to study the reduction of Fe-Cr mixtures. Figure 2.4 shows the displacement, weight loss, and concentration of chromium in a 25 wt% Cr_2O_3 mixture with Fe_2O_3 during reduction in H_2. Dilatometric measurements show thermal expansion upon reduction from Fe_2O_3 to Fe_3O_4, causing

cracking of the extrusion during reduction. Thus, the use of magnetite (Fe_3O_4) is necessary to form nearly defect-free extrusions. Additionally, when studying the reduction of Fe_2O_3−Cr_2O_3 mixtures, it was determined that extruded strips of up to 570 μm thickness and up to 25 wt% chromia could be fully reduced and sintered at 1300°C. As chromia content increases, the temperature at which densification occurs also increases. Figure 2.5 shows the extent of reduction of Fe-25Cr oxide strips as thickness is increased. Increased thickness results in a more open porosity and thus decreased bulk density, hindering the full reduction of the strip.

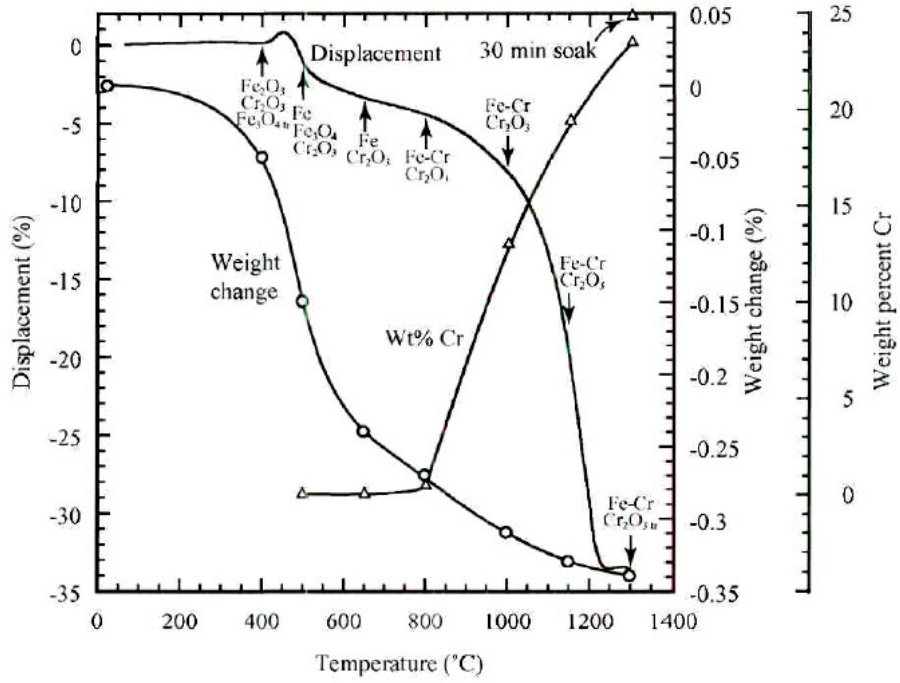

Figure 2.4: Weight loss, displacement, and Cr content of Fe_2O_3-25Cr_2O_3 powder mixtures during reduction [1, 3].

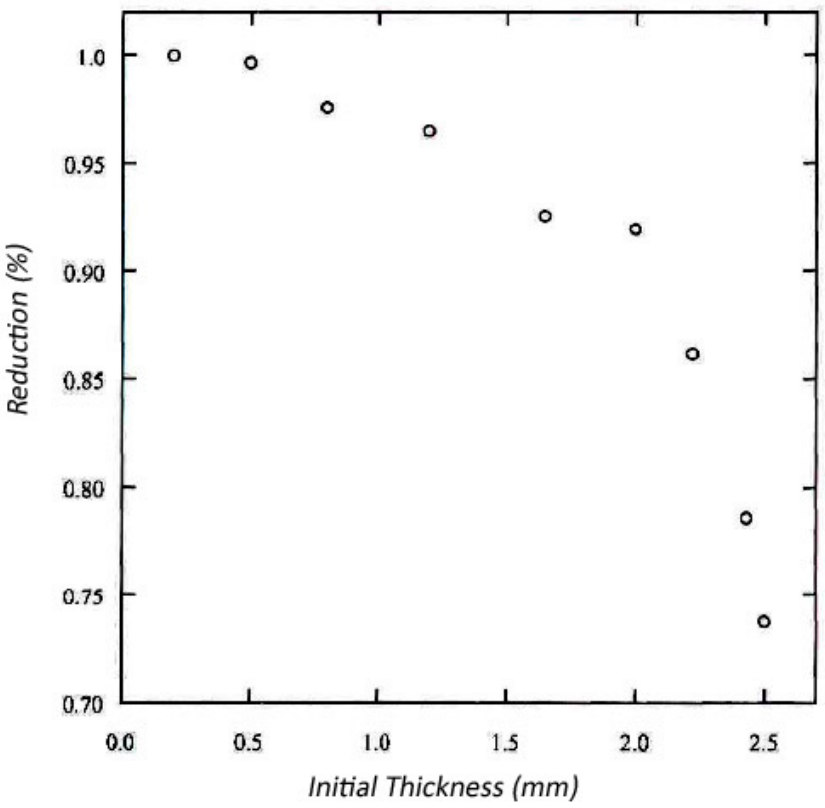

Figure 2.5: Extent of reduction of Fe-25Cr extrusions of varying thickness [3].

While it has been shown that strips of up to 25 wt% chromia can be reduced completely, Khedr [21] shows that small amounts of chromium can greatly inhibit the reduction of Fe_2O_3 during the early stages of reduction (approximately 25% reduction). Small amounts of Cr_2O_3 result in a large increase in the amount of the $(Fe,Cr)_2O_3$ phase, which is much less reducible than Fe_2O_3. However, beyond approximately 2.5 wt% Cr_2O_3 and up to 10 wt% Cr_2O_3, a slight increase in the reduction kinetics during early stages is observed because the amount of $(Fe,Cr)_2O_3$ does not increase directly with Cr_2O_3 content. Alternately, during the final stages of reduction (approximately 75% completion), the presence of 1 wt% Cr_2O_3 greatly increases reduction rates, followed by a sharp decrease with Cr_2O_3 contents up to 10 wt%. This information is summarized in Figure 2.6.

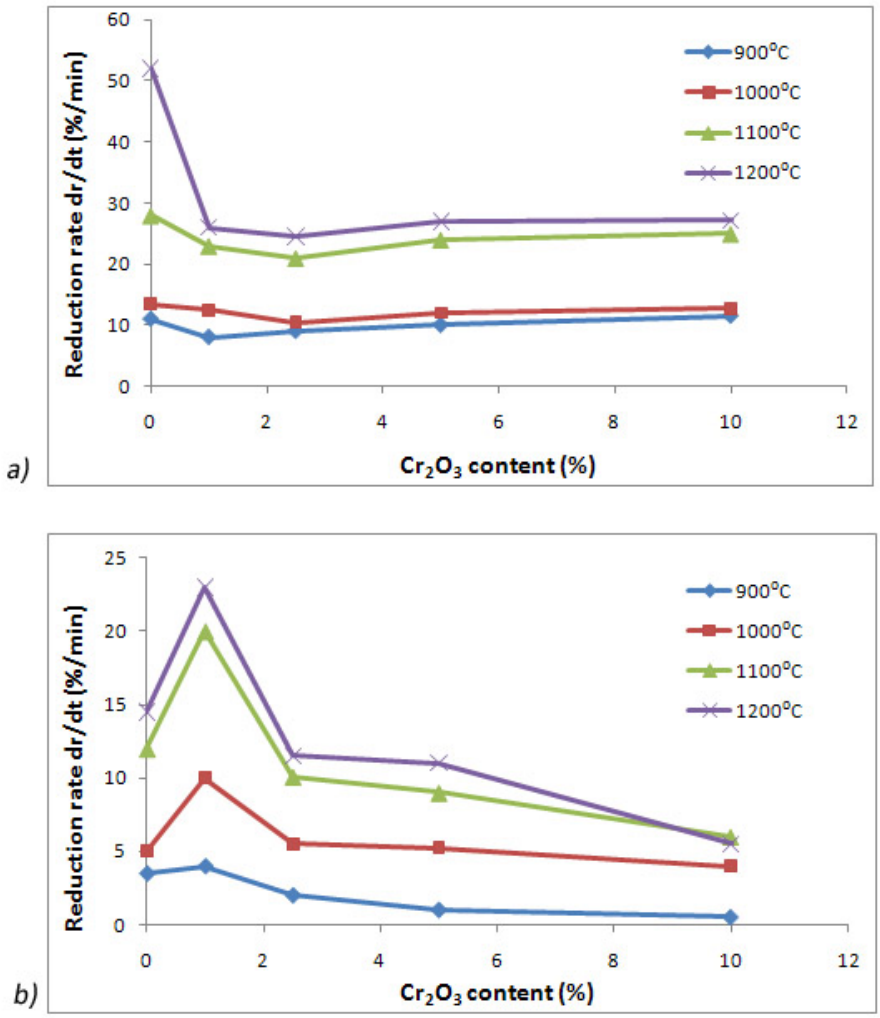

Figure 2.6: Effect of Cr_2O_3 content on the rate of reduction at: a) Initial stages (25% reduction) and b) Final stages (75% reduction). Data taken from Khedr [3, 21].

2.2 Gas Carburization

Traditional gas carburization techniques, as well as a more recent technique termed low temperature colossal supersaturation (LTCSS), will be discussed in the following section. Specific carburization information for the atmosphere of interest in this study, CO/CO_2, is also detailed.

2.2.1 Traditional Gas Carburization

Gas carburization is most typically used to increase the surface hardness of highly alloyed steels, termed *case hardening*. The process is used in many different industries for such parts as gears, bearings, screws, saw blades, and more [22–24]. Traditionally, gas carburization consists of two main stages: a carbon enrichment stage and a carbon diffusion stage. Generally, carburization of iron-based alloys is carried out at temperatures between approximately 870°C and 940°C, such that the part lies in the austenite phase field, though carburization can occur when the part is in the ferrite or delta phase field as well [25].

The carbon enrichment stage begins as the part is saturated with carbon, typically through the introduction of gases such as butane, methane, propane, or through mixtures of CO/CO_2 or $CO/H_2/H_2O$ [26–29]. In general, the carbon diffusion stage then begins as the sample is held at a high temperature, *without* the introduction of more carbon, in order to allow diffusion of carbon into the sample surface. For complex gas mixtures, the rate of carbon transfer to the surface of the part is governed by the rate of the following reaction (Equation 6) [29]:

$$CO + H_2 \longrightarrow C + H_2O \tag{6}$$

As carbon is adsorbed on the surface, transfer of additional carbon will slow if diffusion is not sufficiently fast to allow for carbon atoms to move to the interior of the sample. Thus, carburization rates also increase with increasing temperature as diffusion and reaction rates of Equation 6 increase [29, 30].

Though alloying elements can affect carburizing rates, for low-alloy steels carbon diffusivity at typical carburizing temperatures is not strongly affected by the addition of small amounts of alloying elements, provided stable carbides are not formed [31, 32]. However, some carbide forming elements can have an effect on the diffusivity of carbon. Specifically, chromium additions have shown to decrease the carbon diffusivity in austenite by about 10% per at% of Cr additions, due to trapping of the carbon by Cr. However, a small maximum in carbon diffusivity has been reported at approximately 1 at% Cr [33].

Because carburization is not a steady-state diffusion process, Fick's second law, as shown in Equation 7, must be solved for the boundary conditions applicable to the carburization process in order to estimate the parameters necessary for carburization experiments in this study. In general, Ficks second law is solved for the carburization process assuming the part being carburized is a semi-infinite solid, meaning the carbon will not reach the end of the part during the process. Using this information, the solution to Ficks second law is given by Equation 8 [25, 34, 35].

$$\frac{dC}{dt} = \frac{d}{dx}(D\frac{dC}{dx}) = D\frac{d^2C}{dx^2} \tag{7}$$

where $\frac{dC}{dx}$ represents the concentration gradient of the diffusing species.

$$\frac{C(x,t) - C_0}{C_s - C_0} = 1 - erf\frac{x}{2\sqrt{Dt}} \tag{8}$$

where C_s is the surface carbon concentration, C_0 is the initial carbon content, x is the depth into the surface, D is the diffusion coefficient at the temperature of interest and t is time.

In addition to the general equations which can be used to predict carburization depth, studies have also been performed to determine how several parameters specifically affect the hardness and integrity of carburized steel. The four main parameters that affect the quality and thickness of a case hardened layer during gas-carburizing processes are holding time, carburizing temperature, carbon potential, and quench time. These variables affect the surface hardness and diffusion depth differently. For example, in a study on AISI

3310 [26], an alloyed carbon steel, quench time has the largest effect on surface hardness (60%). This is to be expected, as quenching time will determine the microstructure of the steel, which will be further discussed in Section 2.5.1.1. Additionally, carbon potential and holding time, parameters more generally associated as gas carburization parameters, both have a 20% effect. Carburizing temperature was not found to significantly affect the surface hardness of the steel tested in the study, though, as would be expected, does have an effect on diffusion depth. In the case of AISI 3310, the carburizing temperature had a 15% effect on diffusion depth, where holding time at the elevated temperature had the largest effect (67%). Quench time and carbon potential had a smaller reported effect on case depth of 8% and 9%, respectively.

Variations on the carburizing cycle, as well the composition of the part being carburized, are important to the final carbon gradient achieved during carburization as well. For example, the addition of even small amounts of alloying elements which stabilize the austenite phase field, such as Ni and Si, results in increased carbon diffusivity, attributed to the weaker bonding energy between these elements and carbon. However, significantly lower carbon transfer from the carburizing atmosphere is also observed, which ultimately decreases the rate of carburization of the part. Alternately, the addition of carbide forming elements, such as Cr and Mo, lower the carbon diffusivity due to their positive attraction with carbon, but they significantly increase the mass transfer of carbon onto the surface, thus resulting in faster carburization [36, 37].

2.2.1.1 Carburization in a CO/CO_2 Atmosphere

When a CO/CO_2 atmosphere is used for carburization, the following reaction occurs at the surface (Equation 9):

$$2\,CO + Fe \longrightarrow C_{(in\ Fe)} + CO_2 \tag{9}$$

The equilibrium constant, K, for this reaction can be determined from Equation 10.

$$K = \frac{[N_c][P_{CO_2}]}{[N_{Fe}][P_{CO}^2]} \tag{10}$$

where N_c and N_{Fe} are the mole fractions of carbon and iron and P_{CO} and P_{CO_2} are the partial pressures of carbon monoxide and carbon dioxide, respectively.

Using this information, the carbon content in equilibrium with the atmosphere at a constant temperature and 1 atm pressure can be determined. Figure 2.7 shows the ratio of CO/CO_2 in equilibrium with carbon in iron at different temperatures in the austenite phase field and at 1 atm pressure, using Equation 11 for the value of K. If the pressure is not 1 atm, the pressure effect on carbon equilibrium can be calculated using Equation 12 [25].

$$log_{10}K = -8.43 + 6582\frac{1}{T} \tag{11}$$

where T is the temperature, in Kelvin.

$$K = \frac{\frac{[N_c]}{[N_{Fe}]}\frac{[P_{CO_2}]}{[P_{CO}]}(1 + \frac{[P_{CO_2}]}{[P_{CO}]})}{P} \tag{12}$$

where P is the total pressure.

It is important to note that there are some discrepancies between the results of mathematical calculations shown in Figure 2.7 than with the earlier, experimental findings of R. Smith [38]. For example, Figure 2.8 shows the calculations as presented by Stanley vs. the experimental results of Smith at 1000°C. In general, Smith found that the equilibrium surface concentration of carbon (C_s) at a given P_{CO_2}/P_{CO}^2 ratio was slightly higher than those determined mathematically by Stanley. Besides Smith, several other researchers have observed the carbon content in austenite at 1000°C, as is shown in Figure 2.9, as summarized by Smith.

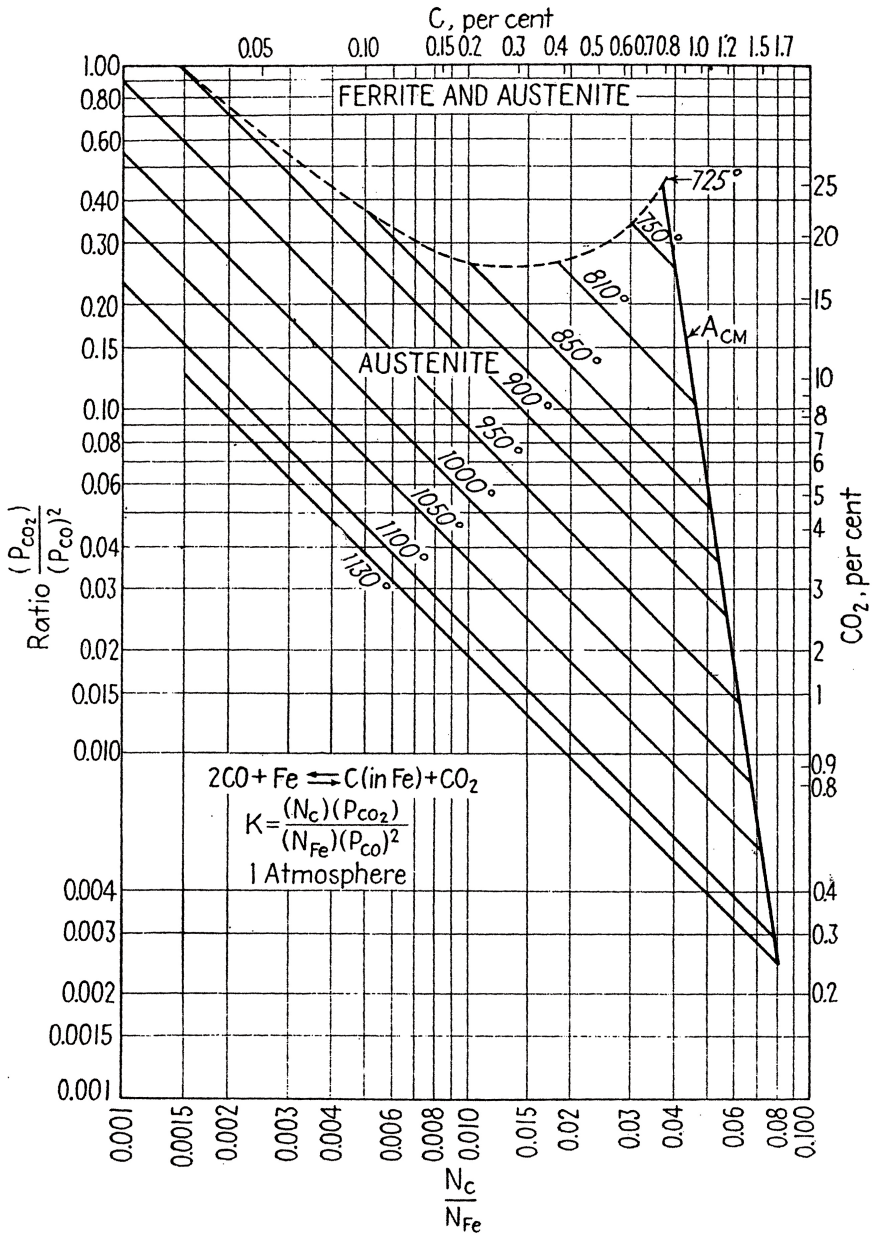

Figure 2.7: Carbon content of austenite with respect to atmosphere composition, as determined from Equations 10 and 11 [38].

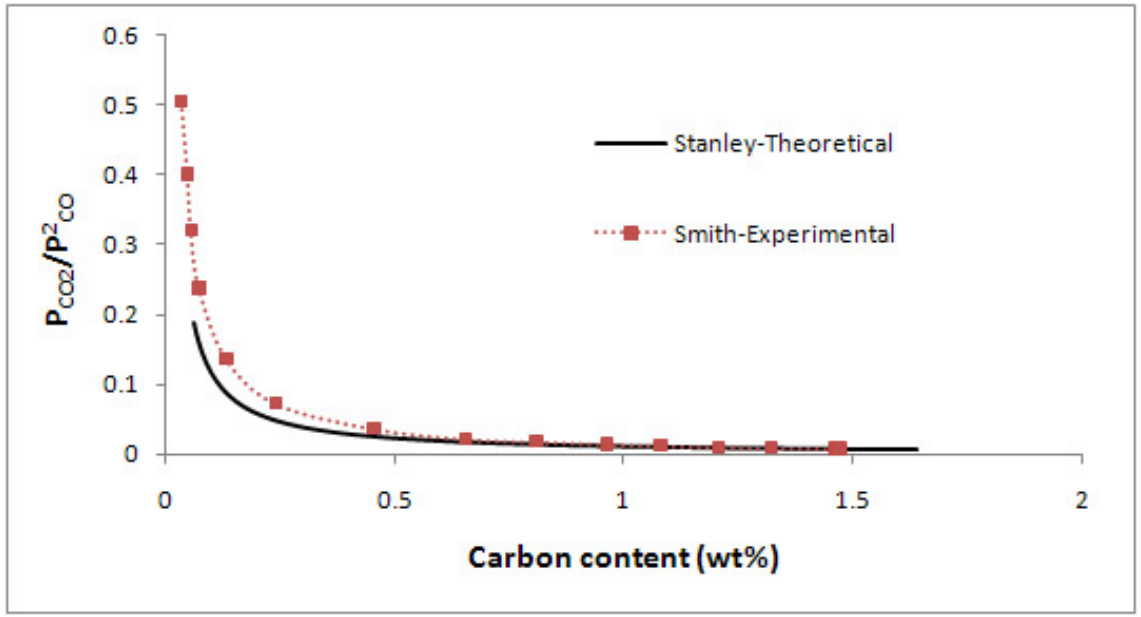

Figure 2.8: Carbon content in equilibrium with austenite with respect to atmosphere composition at 1000°C, as determined experimentally by R. Smith [38] and theoretically by Stanley [25].

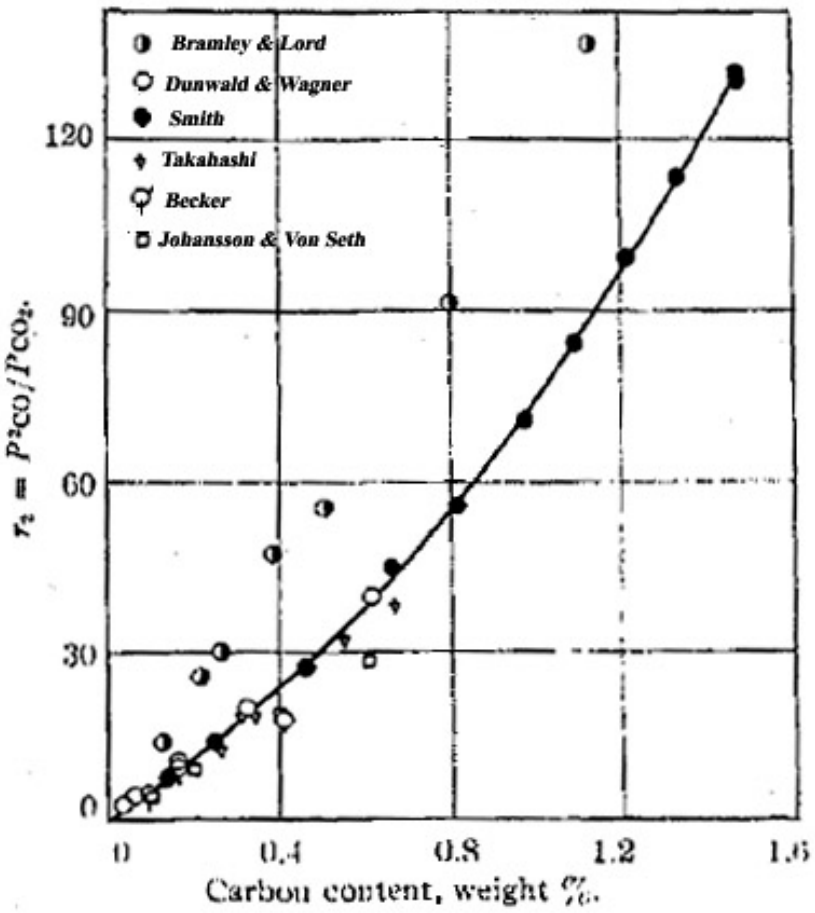

Figure 2.9: Carbon content in equilibrium with austenite with respect to atmosphere composition at 1000°C, as determined experimentally by R. Smith [38]; Dunwald and Wagner [39]; Bramley and Lord [40]; Becker [41]; Johansson and Von Seth [42]; and Takahashi [43] as reported by R. Smith.

2.2.2 Carburization of Stainless Steels

Surface carburizing of stainless steels has been investigated to improve hardness and wear resistance with the aim of retaining corrosion resistant properties. In general, high temperature carburization processes for stainless steels often yield the formation of chromium carbides, which decrease the corrosion resistance of the material. Additionally, it has been shown that carburization is only possible via the migration of carbon through pores and

cracks in the chromium oxide scale, due to the near-zero solid solubility of carbon in Cr_2O_3 [44]. Thus, carburization of stainless steels at high temperatures is both difficult to achieve and can be detrimental to corrosion performance.

In recent years, carburization techniques for stainless steels at temperatures below approximately 600°C have been investigated, such that the solid solubility of carbon in the part is increased. The formation of a metastable "expanded austenite" phase on the surface of the part has proven successful to case-harden stainless steel [45]. Additionally, a technique referred to as low temperature colossal supersaturation (LTCSS) has proven to successfully case-harden an austenitic stainless steel (316L) to a surface carbon concentration of approximately 14 at% (3.3-3.4 wt%) without the formation of carbides [46]. LTCSS has shown to greatly improve wear resistance, fatigue resistance, and pitting corrosion resistance of austenitic stainless steels as well as result in surface microhardness values exceeding 1000HV [47–49]. The following section will describe LTCSS in further detail, as it is the basis for stainless steel carburization used in this research.

2.2.2.1 LTCSS

In general, LTCSS is used for the carburization of austenitic stainless steels, and most recently, duplex and ferritic stainless steels [50]. The process is carried out at temperatures high enough such that carbon diffusion can proceed, while avoiding temperatures so high where significant amounts of carbides can form. This is possible due to the faster interstitial diffusion of carbon atoms as compared to carbide forming, substitutional atoms such as chromium and nickel. Figure 2.10 shows a time-temperature-transformation (TTT) diagram for 316L stainless steel with varied carbon contents, illustrating the regimes in which carbides form. Additionally, the temperature range for which LTCSS is performed is shown in the figure.

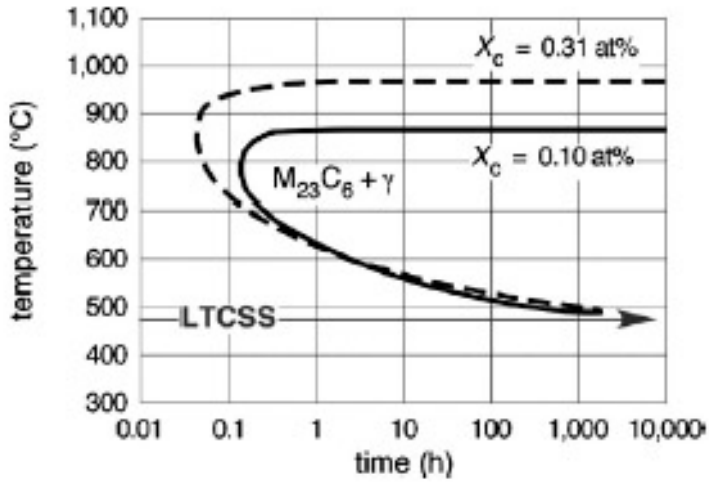

Figure 2.10: Time-temperature-transformation diagram for 316 stainless steel showing the regime for LTCSS, where X_c is the starting carbon content of the steel [46].

It is evident from Figure 2.10 that the carbide forming regime decreases to lower temperatures as time progresses, thus LTCSS is ideally carried out at higher temperatures at earlier times, then decreased at longer times. This allows for the fastest diffusion possible without the formation of carbides at all temperatures. In the general sense, the carburizing temperature is typically kept at approximately 15-30°C below the temperature at which carbides form. The carburization process can theoretically take place using any of the common mixtures used for carburization, though researchers have specifically tested $CO/CO_2/N_2$ as well as $CO/H_2/N_2$ [51].

In order to successfully carburize a stainless steel part, the protective chromium oxide layer must be removed. Several methods have proven successful in depassivating the surface of 316 stainless steel prior to carburization, including the use of gases such as HCl and HF at elevated temperatures, electroplating with iron, contact with a molten salt bath including sodium cyanide, contact with liquid sodium and contact with a strong base [49, 51–53].

Results of carburization experiments using this technique have shown carbon profiles

that are not consistent with error function solutions to Fick's second law, as was discussed in Section 2.2.1. Research by Ernst *et al*. [54] theorizes that actual carbon profiles are due to increased carbon diffusion as carbon content increases through the carburization process. Ernst suggests that the most likely reason for this phenomena is due to the increase of the lattice parameter as a result of increased amounts of interstitial carbon. As such, there is less metal to metal interaction and the activation energy for carbon diffusion thus decreases during carburization.

2.3 Metal Dusting

Metal dusting, the catastrophic form of carburization, has the potential to occur in carburizing processes. Metal dusting causes serious material deterioration as a result of the disintegration of typically iron, nickel, and cobalt - based alloys into metal particles and carbon [55–60]. In iron-based alloys, metal dusting typically occurs due to the separation of iron carbide into iron and carbon particles following Equation 13 [61, 62]. Most often, metal dusting is observed as a uniformly corroded layer on iron and low-alloy steels [60], and it is often termed "sooting" due to its appearance.

$$Fe_3C \longrightarrow 3\,Fe + C_{graphite} \tag{13}$$

Specifically, metal dusting has five reaction steps [60, 63, 64]:

1. Supersaturation of iron with dissolved carbon
2. Precipitation of cementite at the iron surface as well as grain boundaries, thus blocking carbon diffusion into the sample
3. Deposition of graphite on the cementite surface, causing the instability of cementite
4. Decomposition of cementite to graphite and metal particles
5. Diffusion of metal atoms to form clusters that act as catalysts for further deposition of carbon from the atmosphere

As can be seen in Figure 2.11, an Ellingham diagram for carbides, iron carbide (Fe_3C) is a metastable compound, as the standard Gibbs free energy of formation (ΔG°) of Fe_3C crosses $\Delta G^\circ = 0$ at approximately 1000°C. This temperature is believed to be the upper limit for which metal dusting can occur, as Fe_3C becomes more stable.

Generally, it is believed that metal dusting occurs most often in the temperature range 400-800°C [56–58] and that carbon monoxide is the strongest metal dusting molecule. However, it is important to note that the presence of hydrogen will often increase metal dusting corrosion by allowing for faster oxygen removal from the surface [62, 66].

The decomposition of carbon monoxide into carbon and carbon dioxide as shown in Equation 14, known as the Boudouard reaction, allows for carbon to be transferred to the metal surface and thus the metastable, Fe_3C carbide can be formed.

$$2\,CO \longrightarrow C + CO_2 \tag{14}$$

Theorized by Hochman [58] and confirmed by Grabke [56], as carbon continues to deposit on the surface, the Fe_3C becomes less stable, thus decomposing into fine metal and graphite particles. Figure 2.12 shows a schematic of the metal dusting mechanism, including carbon activity, and SEM images during the process, using a CO/H_2 atmosphere for an example [64]. More specifically, upon decomposition of Fe_3C to its constituents, iron diffuses through the space between adjacent graphite planes and agglomerate to form metal particles, while carbon atoms attach to graphite protrusions [44].

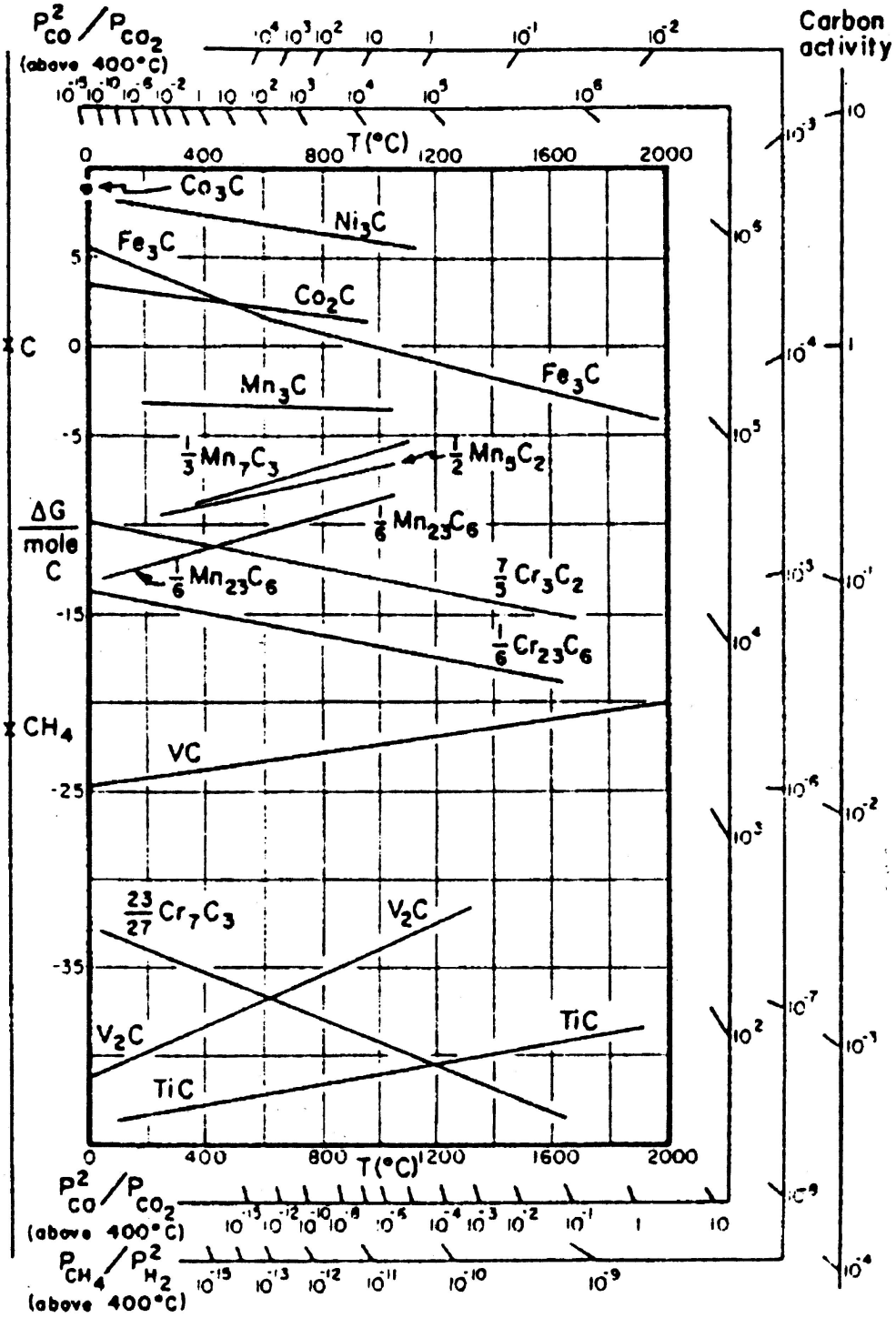

Figure 2.11: Ellingham diagram of various carbides [65].

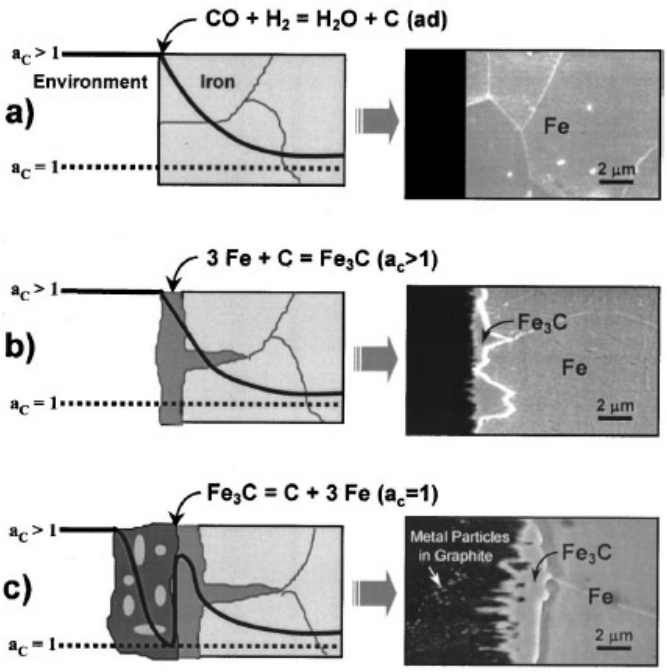

Figure 2.12: The various stages of metal dusting of iron: (a) Carbon transfer to the surface, (b) Precipitation of metastable Fe_3C at the surface and (c) Decomposition of iron carbide after carbon deposition [62, 64].

Chun *et al*. [62] further explained the specific mechanisms for metal dusting corrosion of iron in different temperature regimes:

1. 350°C-500°C: The rupture and reformation of metastable Fe_3C is the dominant corrosion mechanism.

2. 500°C-575°C: The main metal dusting mechanism is the rapid growth of Fe_3C particles and its subsequent dissociation. More specifically iron atoms (as a result of Fe_3C dissociation) diffuse outwardly into graphitic carbon deposits that are oriented perpendicular to the Fe_3C surface. When the iron reaches the carburizing atmosphere at the surface, this acts as a catalyst for the growth of filaments of carbon.

3. 575°C-775°C: The same mechanism, the dissociation of metastable Fe_3C, is dominant. However, corrosion rates decrease at temperature increases because Fe_3C becomes more stable.

4. 775°C and above: The surface layer of Fe_3C evident in other temperature regimes is not present due to the rapid diffusion of carbon in iron at elevated temperatures. The dominant metal dusting mechanism in this case is the deposit of carbon on the surface of the metal.

Zhang *et al*. [67] confirmed the observation of filamentous carbon deposits, a schematic of which is shown in Figure 2.13. Additionally, a faceted structure during metal dusting was observed, illustrating the phenomenon's dependence on crystallographic orientation. Specifically, it has been shown that carbon deposits located such that the graphite planes are perpendicular to the existing cementite surface accelerate metal dusting. This is due to the fact that carbon, which is dissociated from the cementite layer, can more readily attach to graphite in this orientation [66], thus finer grain structure at the surface accelerates cementite nucleation and subsequent decomposition [67]. In general, metal dusting can be catastrophic very quickly, as it has been determined that the growth of carbonaceous deposits during metal dusting follows a t^2 dependence, as is shown in Equation 15 [60].

$$\frac{\Delta m_c}{A} \approx t^2 \tag{15}$$

where Δm_c is the change in mass of deposited carbon, A is the area of the sample, and t is time.

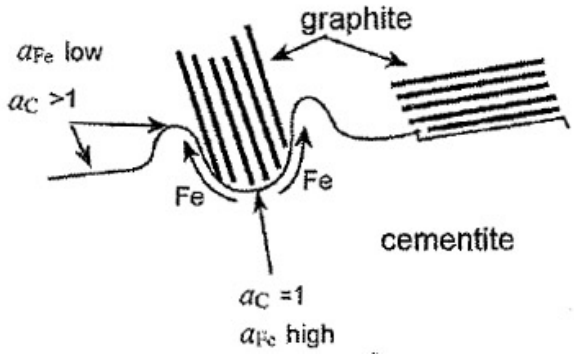

Figure 2.13: Illustration of the formation of graphite filaments and subsequent cementite protrusions during gas carburization of iron [67].

In order to avoid metal dusting, thermodynamic studies can be used to predict the parameters necessary such that metal dusting is not favored. For example, Figures 2.14 and 2.15 illustrate the dependence of temperature for metal dusting in a CH_4/H_2 and a CO/CO_2 atmosphere, respectively. Additionally, both plots show the dependence of volumetric ratio of the carburizing gas as well as total pressure dependence on the size of the metal dusting regime. In general, metal dusting can occur if the chemical potential of carbon in the atmosphere is greater than the chemical potential of carbon in Fe_3C. From Figure 2.14(a), it is shown that the metal dusting temperature regime increases with increasing volumetric ratio of CH_4, due to the fact that the chemical potential of carbon in the atmosphere increases with increasing temperature. In Figure 2.14(b), it can be seen that an increase in pressure further inhibits metal dusting attack. On the contrary, in CO/CO_2 atmospheres (Figure 2.15), increasing volumetric ratio of CO results in an increased metal dusting temperature regime, as the chemical potential of carbon in the atmosphere decreases with increasing temperature. As can also be seen in Figure 2.15, as total pressure of the atmosphere increases in the case of CO/CO_2, the temperature regime for metal dusting expands [61].

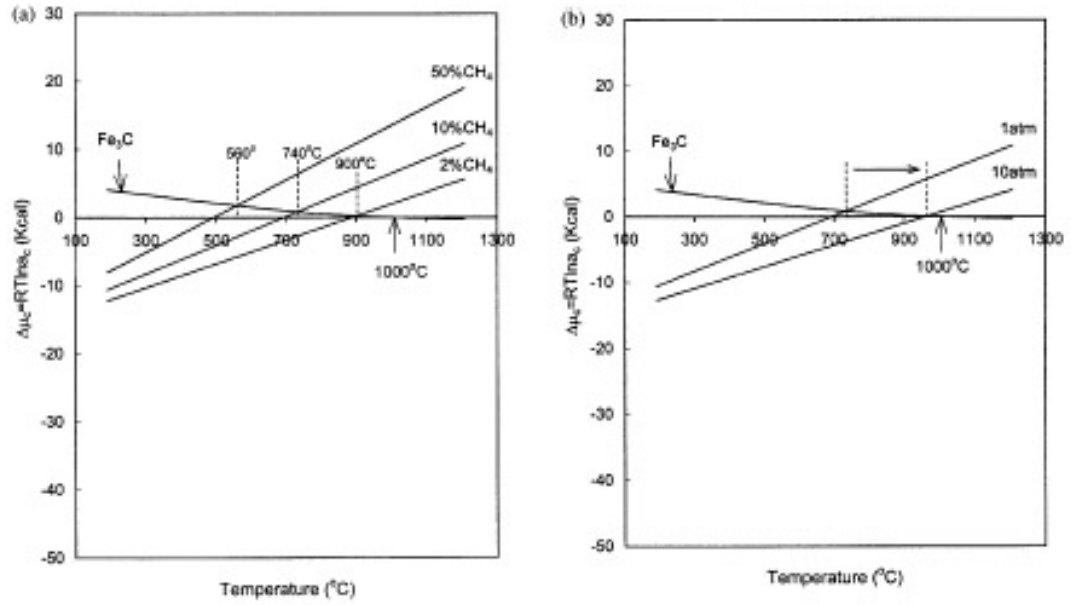

Figure 2.14: Temperature regime for metal dusting as (a) volumetric ratio of CH_4 expands and (b) total pressure increases [61].

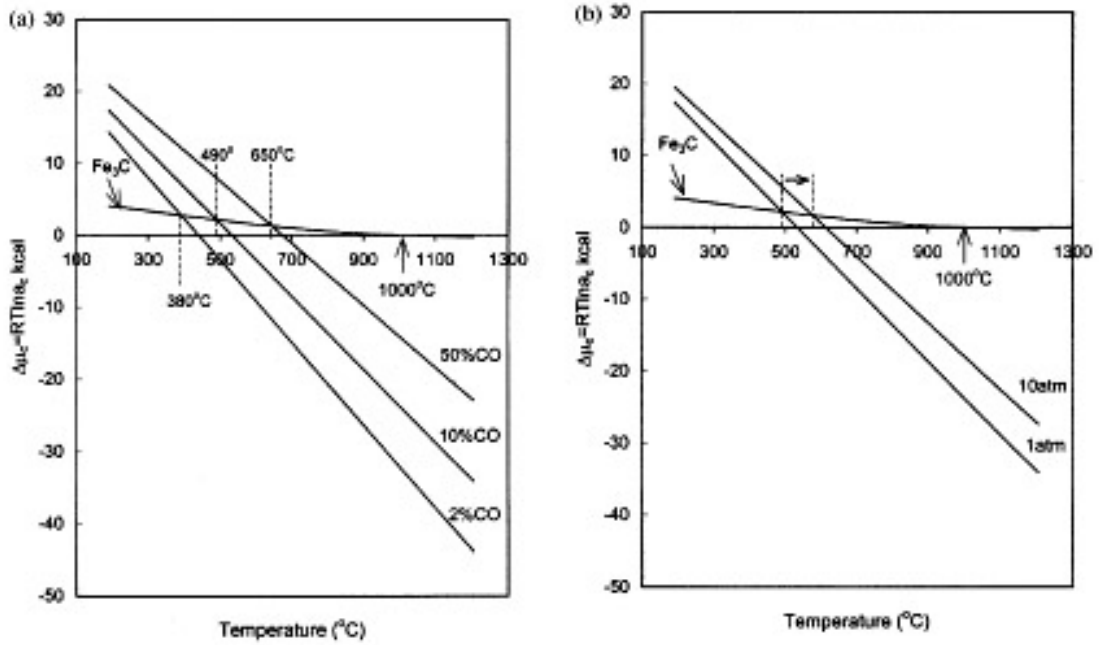

Figure 2.15: Temperature regime for metal dusting as (a) volumetric ratio of CO_2 expands and (b) total pressure increases [61].

2.3.1 Metal Dusting in Stainless Steels

In stainless steels, a protective Cr_2O_3 layer is naturally formed. Due to the fact that the solid solubility of carbon in Cr_2O_3 is essentially nil, metal dusting can be avoided as carbon cannot diffuse through the surface layer for carburization times less than approximately 12 hours [44, 68]. However, Chun *et al*. [66] have found the Cr_2O_3 layer may only provide initial protection against metal dusting in certain cases, as cracking in the film allows for rapid carbon diffusion and the subsequent formation of M_7C_3 carbides, which can also dissociate into metal particles and graphite. This results in localized areas of metal dusting, observed as pits in the surface [60]. Chun suggests that metal dusting in stainless steels with nickel contents higher than 10 wt% can occur without the formation of M_3C carbides at the surface, as with most metal dusting cases. On the contrary, Grabke [64] suggests that in chromium steels, metal dusting still occurs via the disintegration of M_3C carbides, as the formation of stable M_7C_3 and $M_{23}C_6$ carbides leads to the formation of the metastable M_3C carbide, as is illustrated in Figure 2.16.

In the case of both stainless and low-alloy steels, sulfur has proven to be useful in the protection of parts against metal dusting in carburizing atmospheres. When even very low amounts of sulfur are adsorbed onto the surface of iron, a monolayer is created, which slows the diffusion of carbon into the part and thus protects again the nucleation of graphite filaments as well [63, 69]. Also, the addition of silicon has shown to protect against metal dusting, due to the formation of a protective silica-rich oxide layer [70]. Both of these measures prevent the formation of metal dusting through the prevention of carburization, the first step in the metal dusting process. Thus it is important in this study to avoid the conditions where it is thermodynamically favorable for metal dusting to occur, as the Cr_2O_3 films are removed such that carburization can take place in this study.

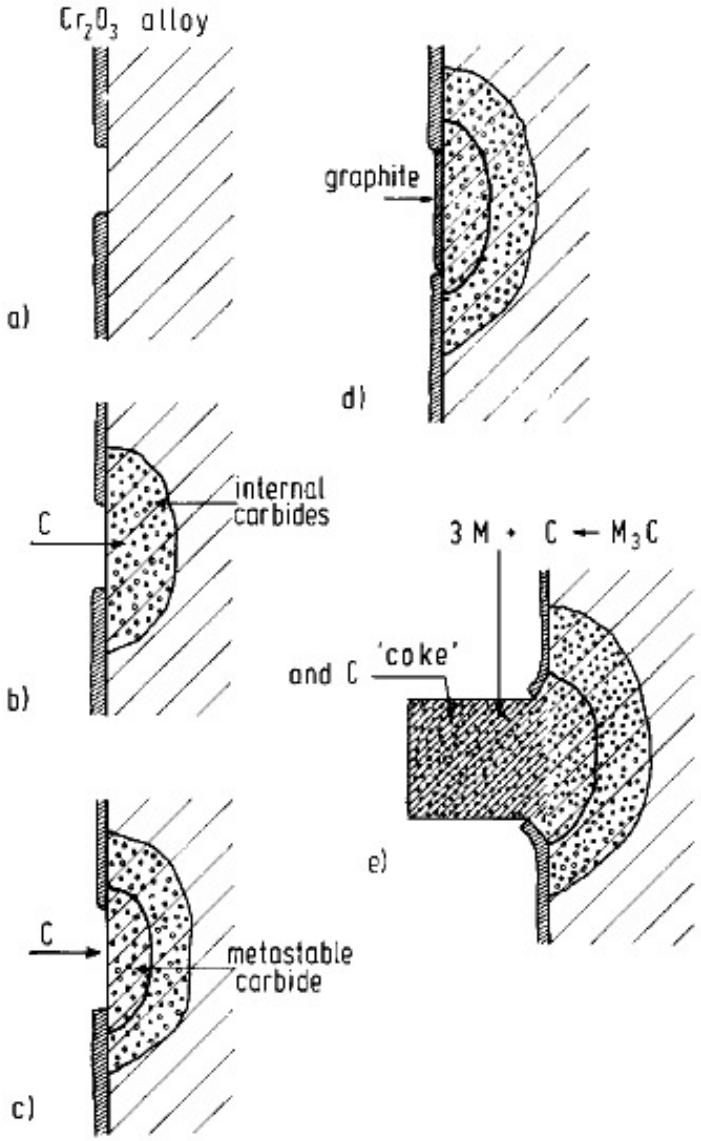

Figure 2.16: Mechanism of metal dusting on chromium steels: (a) The formation of a defective Cr_2O_3 scale, (b) entrance of carbon through the defect and formation of stable carbides ($M_{23}C_6$, M_7C_3), (c) supersaturation and subsequent formation of metastable carbide (M_3C), (d) graphite deposition causing (e) decomposition of metastable carbide to graphite and metal particles [64].

2.4 Decarburization

Decarburization, the loss of carbon atoms from the surface of steel, often occurs at high temperatures in atmospheres where oxidizing species are present [71]. For example, the presence of hydrogen has shown to decarburize iron alloys through the production of methane gas, as shown in Equation 16 [72]. In the case of a hydrogen atmosphere, methane bubbles do not readily diffuse through steel and as such, accumulate as growing bubbles along the grain boundaries of the part [72].

$$Fe_3C + 2\,H_2(g) \longrightarrow 3\,Fe + CH_4(g) \tag{16}$$

Alternately, the presence of hydrogen and water vapor has shown to decarburize steels through Equation 17 [73].

$$C + H_2O \longrightarrow CO + H_2 \tag{17}$$

Removal of carbon from the surface of a steel part results in the reduction of the mechanical properties of the part. For example, significant drops in fatigue resistance are often observed [74]. Also contributing to the weakening of the part is the observed grain growth that is evident upon carbon removal [75]. It has been shown, however, that the addition of alloying elements in large amounts, including chromium (18%) and nickel (8%) reduce the decarburization behavior of iron alloys [75].

For the case of decarburization through a ferrite matrix, a schematic of a carbon profile is shown in Figure 2.17, which can be used to estimate the decarburization depth. Specifically, decarburization depth in ferrite of Fe-C alloys held at constant temperature in air can be predicted through Equation 18 [76, 77].

$$X = \sqrt{\frac{6C_b \cdot D \cdot t}{3C_t - 2C_b}} \tag{18}$$

where X is the ferrite decarburizing depth, D is the diffusion coefficient of carbon in ferrite, C_b is the solubility of carbon in ferrite, C_I is the initial carbon composition of the alloy and t is the time.

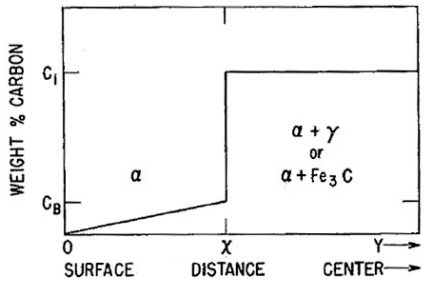

Figure 2.17: Schematic of the carbon profile of a partially decarburized sample [38].

The presence of carbides in a steel part can greatly affect the decarburization rate of the sample, and the dissolution of precipitates has been well studied [78–80]. A simple schematic depicting the dissolution of a spherical cementite particle is shown in Figure 2.18. In this case, it is not simply the diffusion of carbon through the lattice and reaction at the surface which determine the rate of decarburization. Some of the most important factors which control carbide dissolution are temperature, size effects, chemistry, and distribution of alloying elements [80]. Research has shown that increased curvature generally tends to increase dissolution rates when the composition difference between the precipitate and the matrix is small [81]. However, it has also been shown that the curvature of Fe_3C precipitates, specifically, does not significantly affect the dissolution kinetics of cementite precipitates [82]. The dissolution rate can be significantly slowed through the presence of overlapping diffusion particles as well as the presence of additional alloying elements [80].

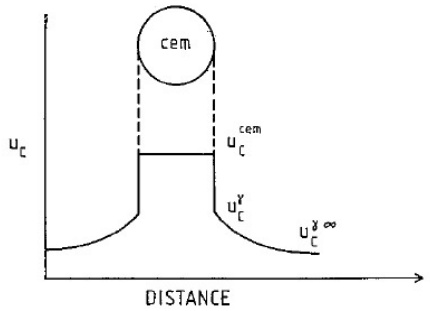

Figure 2.18: Schematic of the dissolution of a spherical cementite particle [80].

2.5 Alloys of Interest

The alloys of interest in this study are of low alloy steel and austenitic steel compositions. Because the use of steel dates back to as far as 1200BC [83] and has been heavily investigated, the following section will provide a brief background of steel and its microstructures, while focusing on the alloys of interest in this research.

2.5.1 The Fundamentals of Steel

Steels are, in general, alloys of iron, carbon and other elements that typically contain less than 2.1 wt% carbon. Figure 2.19 shows a Fe-Fe_3C phase diagram (carbon contents up to 6.7 wt%), which is most pertinent to the study of steels [34]. Through the heat treatment of steel, several different phases and thus microstructures can be observed, all with varying mechanical properties. Figure 2.20 shows an isothermal transformation diagram for a eutectoid Fe-C steel, illustrating some of the microstructures that can be produced. The following section will discuss, in brief, the different phases of steel that are pertinent to this research.

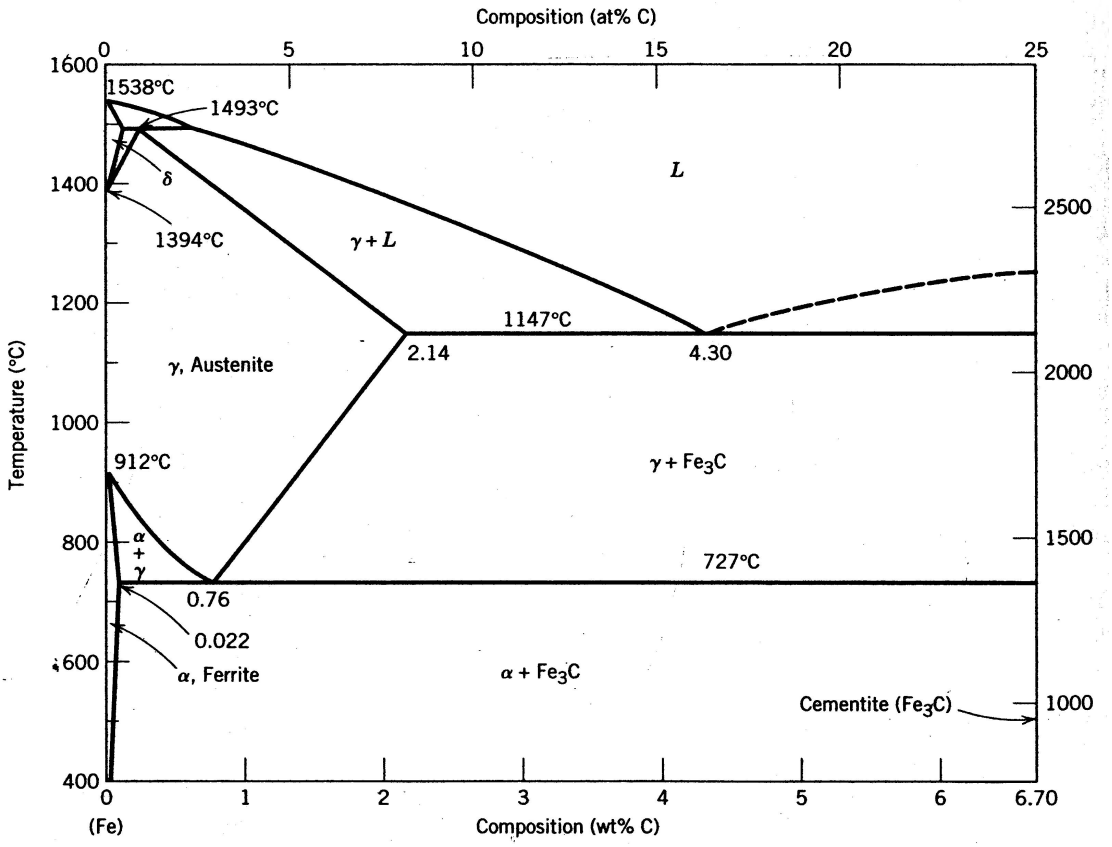

Figure 2.19: The Fe-C phase diagram, as shown up to 6.7 wt% C [34].

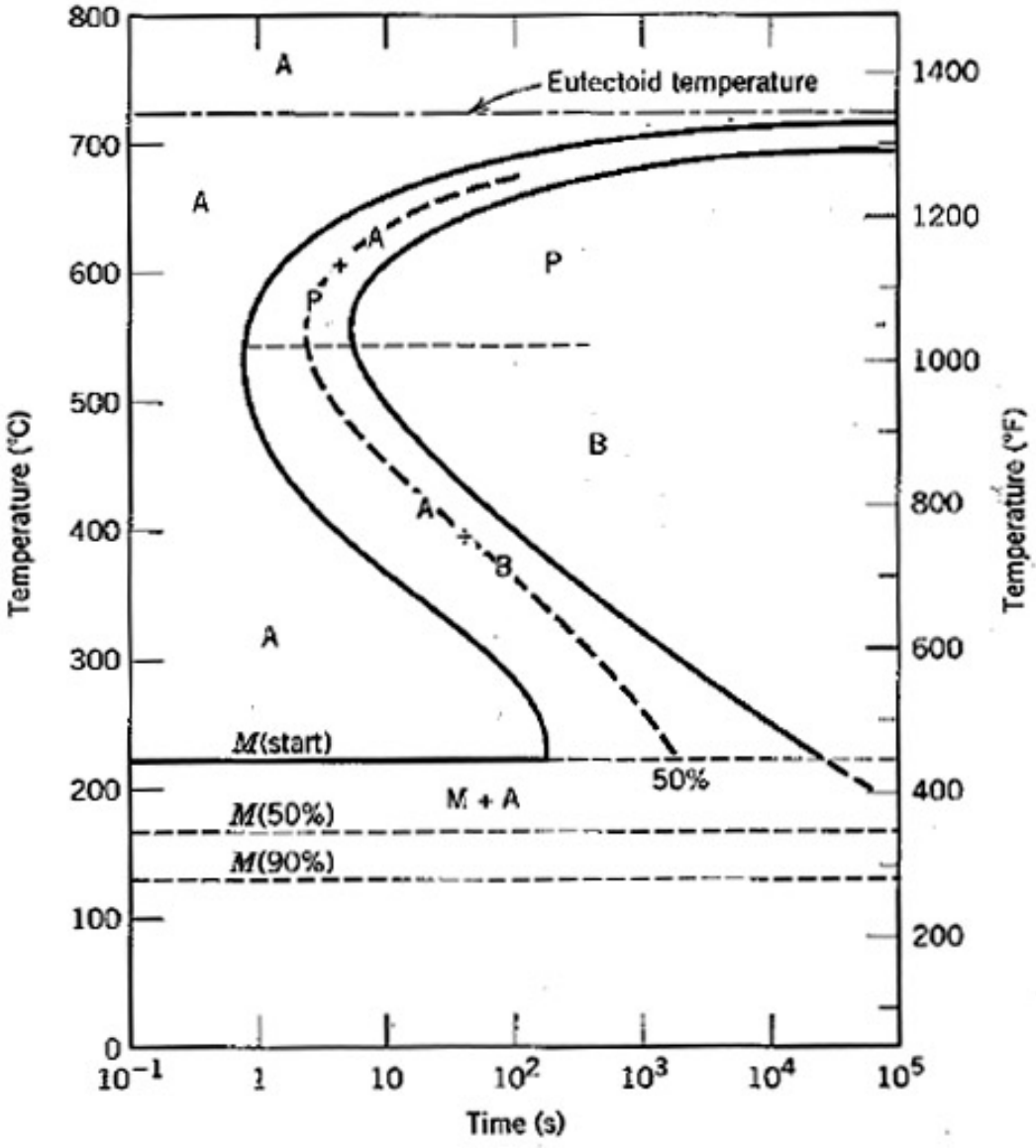

Figure 2.20: Isothermal transformation diagram for a eutectoid Fe-C steel where A, P, B, and M represent austenite, pearlite, bainite and martensite, respectively [34].

2.5.1.1 Phases of steel

Ferrite, or α-iron, is the room temperature stable form of most steels, having a body centered cubic (BCC) crystal structure. Upon heating, the solid solubility of carbon in steel is increased as ferrite undergoes a polymorphic transformation to face-centered cubic, austenite (γ-iron). At even higher temperatures, the delta phase of iron, δ-ferrite, also with a BCC structure, is formed prior to the melting temperature of iron at 1538°C. Cementite, or Fe_3C, is formed at 6.7 wt%C, as is shown in Figure 2.19.

Pearlite, the lamellar structure of ferrite and cementite, develops under slow cooling conditions and during isothermal heat treatment at temperatures between approximately 550-720°C [84]. Upon rapid quenching from the austenite phase, steel massively transforms to a body centered tetragonal structure, termed martensite. Martensite can exist in lath (compositions less than 0.6 wt%C) and plate form (compositions greater than 0.6 wt%C), or a mixture of the two. It is known for its high hardness and brittleness [84], both of which are highly dependent on the carbon content of the alloy. Figure 2.21 illustrates the effect of carbon on the hardness of martensite as compared to austenite.

At intermediate temperatures, between the pearlite and martensite transition temperatures, upper and lower bainite can form. Bainite is the term for the microstructure where ferrite plates or laths are formed *with* cementite particles. Upper bainite transformations occur between approximately 400°C and 550°C, while lower bainite transforms in the temperature range from approximately 250°C to 400°C. The microstructures of upper and lower bainite are very similar, with the major difference being that cementite particles precipitate inside the ferrite plates of lower bainite rather than between the ferrite plates in upper bainite [84].

Spheroidite, a uniform distribution of spherical cementite particles in a ferrite matrix, is also of interest. Spheroidizing is associated with more ductile steels and is achieved through prolonged heating, as there is a thermodynamic driving force for cementite to form spheres, in order to decrease its interfacial energy with the ferrite matrix.

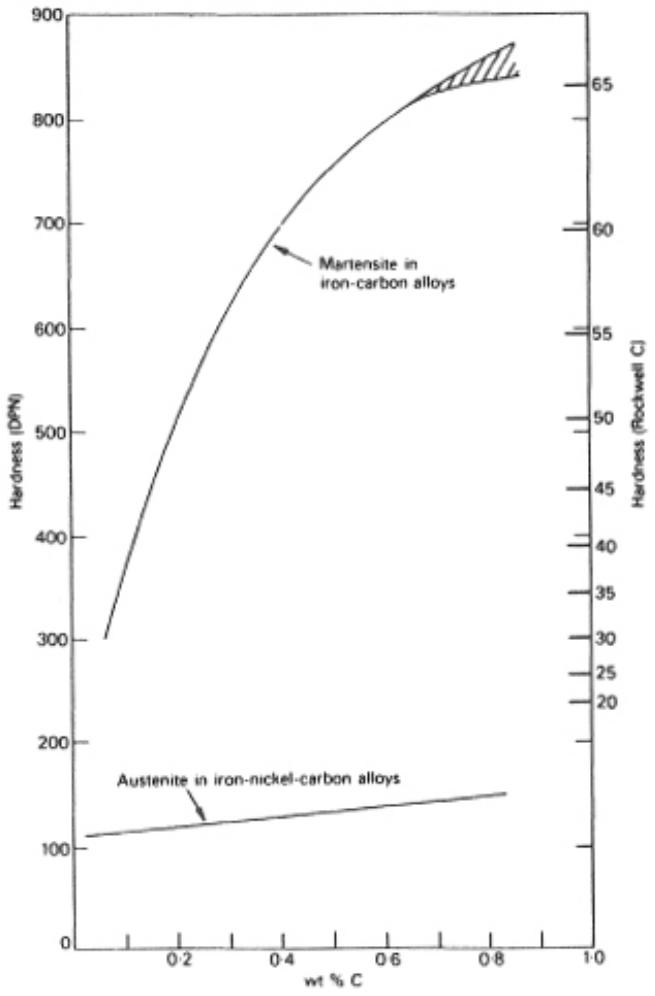

Figure 2.21: The effect of carbon on the hardness of martensite and austenite [84].

2.5.2 Steel of 4140 Composition

4140 is a low alloy steel, with composition listed in Table 2.1. The low material cost associated with 4140, as well as its high hardenability, make it particularly attractive as an alloy which may be used for the fabrication of proppants.

Table 2.1: Composition of AISI 4140 steel.

Element	Composition (wt%)
C	0.37-0.43
Mn	0.75-1.00
Cr	0.80-1.10
Mo	0.15-0.35

Figure 2.22 shows a diagram of hardness values associated with percent transformed to martensite in a 4140 steel. An isothermal transformation diagram for 4140 steel is shown in Figure 2.23, depicting the martensite start (M_s) temperature to be at approximately 350°C. As with all steels, heat treatment is essential to the final material properties of the alloy. Table 2.2 shows the various mechanical properties which can be achieved in a 4140 steel in the quenched and tempered condition.

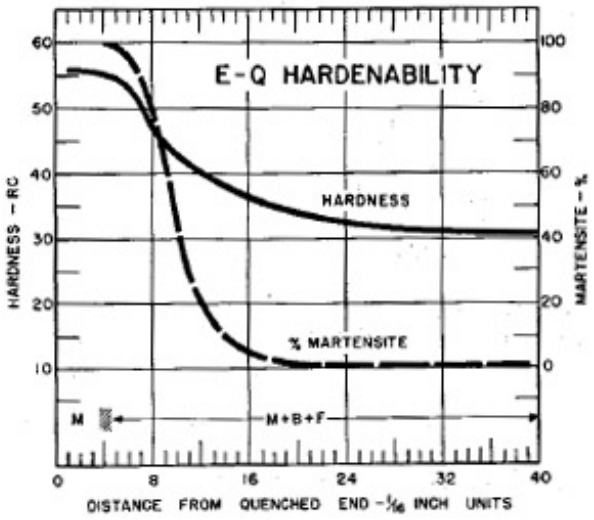

Figure 2.22: Diagram illustrating the hardenability of 4140 steel as related to the percent transformed to martensite [85].

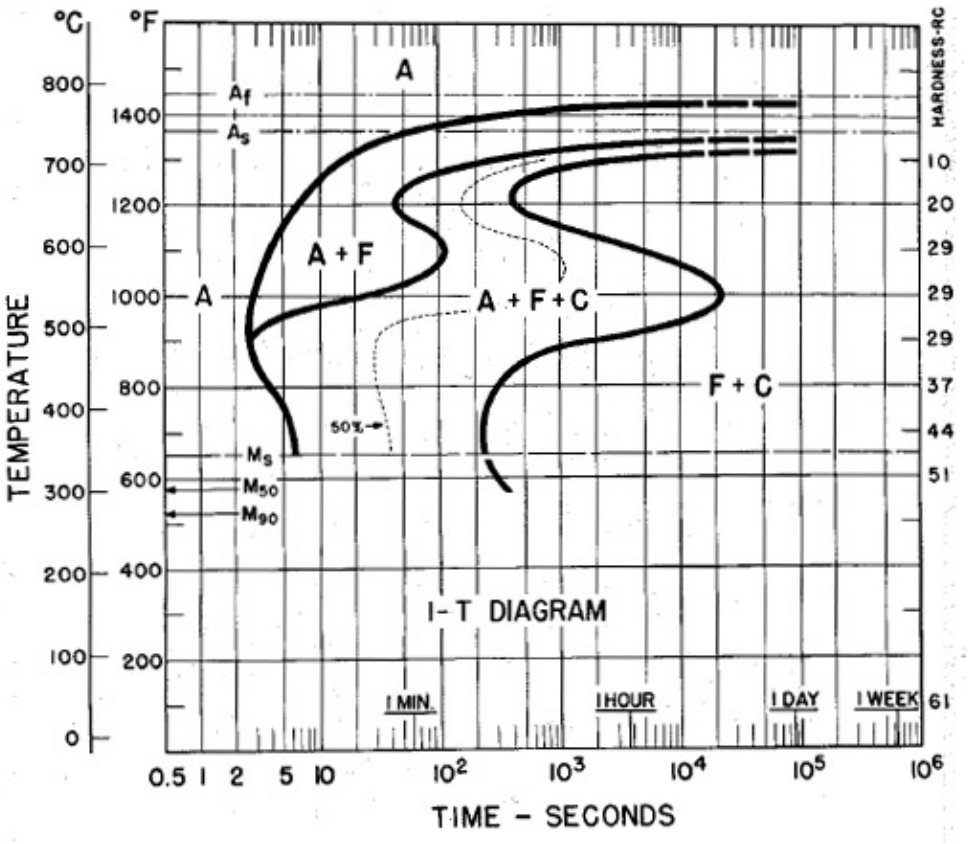

Figure 2.23: Isothermal transformation diagram for 4140 steel where A is austenite, F is ferrite, C is cementite, and M is martensite [85].

Table 2.2: Mechanical properties of oil-quenched and tempered 4140 steel [86].

Tempering Temp. (°C)	Tensile Strength (MPa)	Yield Strength (MPa)	Elongation (%)	Reduction in Area (%)	Hardness (HB)
205	1772	1641	8	38	510
315	1551	1434	9	43	445
425	1248	1138	13	49	370
540	951	834	18	58	285
650	758	655	22	63	230

2.5.3 Steel of 316 Composition

AISI 316 is an austenitic stainless steel, meaning that the crystal structure is FCC at room temperature rather than the more common BCC structure. The composition of 316L, a low carbon form of 316, is given in Table 2.3. The Fe-Cr phase diagram is shown in Figure 2.24, where a γ-Fe loop is evident at chromium contents below approximately 20 wt% Cr

and temperatures between approximately 820°C and 1400°C. In 316 steel, the addition of nickel expands the austenite phase field, such that increased solid solubility of carbon is possible at room temperature [84], while large chromium contents results in the formation of a passive Cr_2O_3 surface layer that protects the steel from corrosion. Furthermore, molybdenum additions in 316 alloys provide pitting resistance in such environments as phosphoric and acetic acids and dilute chloride solutions [86].

Table 2.3: Composition of AISI 316L steel.

Element	**Composition (wt%)**
Cr	16-18.5
Ni	10-14
Mo	2-3
Mn	<2
C	0.05

The 550°C isotherm of the ternary Fe-Ni-Cr diagram can be seen in Figure 2.25 and can be used as an estimate of the structure of 300 series stainless steels, in which four phases can be have been identified through previous research [87, 88].

1. Gamma (γ) fcc - based on (γ) Fe and Ni
2. Alpha (α) bcc based on (α)-Fe
3. Alpha' (α') bcc based on chromium
4. Beta (β) phase or sigma (σ) phase

The composition of 316 steel is denoted in Figure 2.25, showing that the γ phase (austenite) is the equilibrium phase at that temperature.

Table 2.4 shows some of the mechanical properties associated with 316 stainless steel. It is important to note that this composition is associated with a carbon content of approximately 0.08 wt% C. Variations in carbon content will significantly affect the mechanical properties of the alloy, and it is the goal in this study to achieve carbon contents much greater than 0.08 wt%.

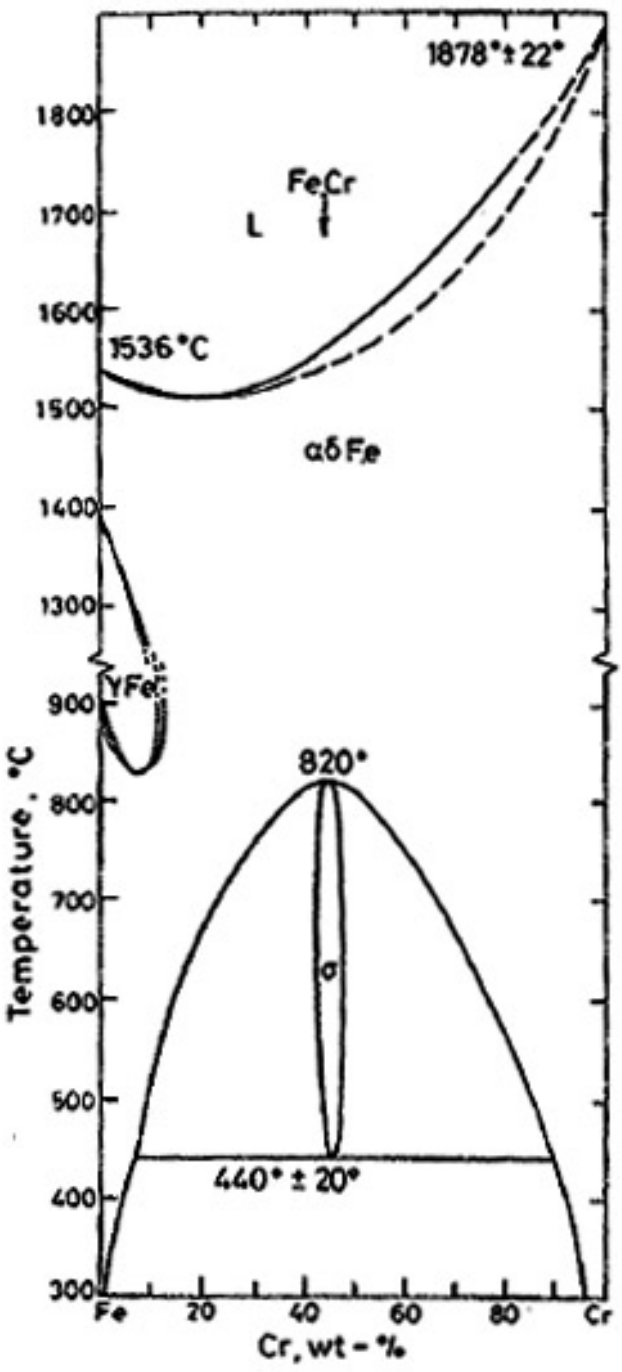

Figure 2.24: Fe-Cr phase diagram [87, 88].

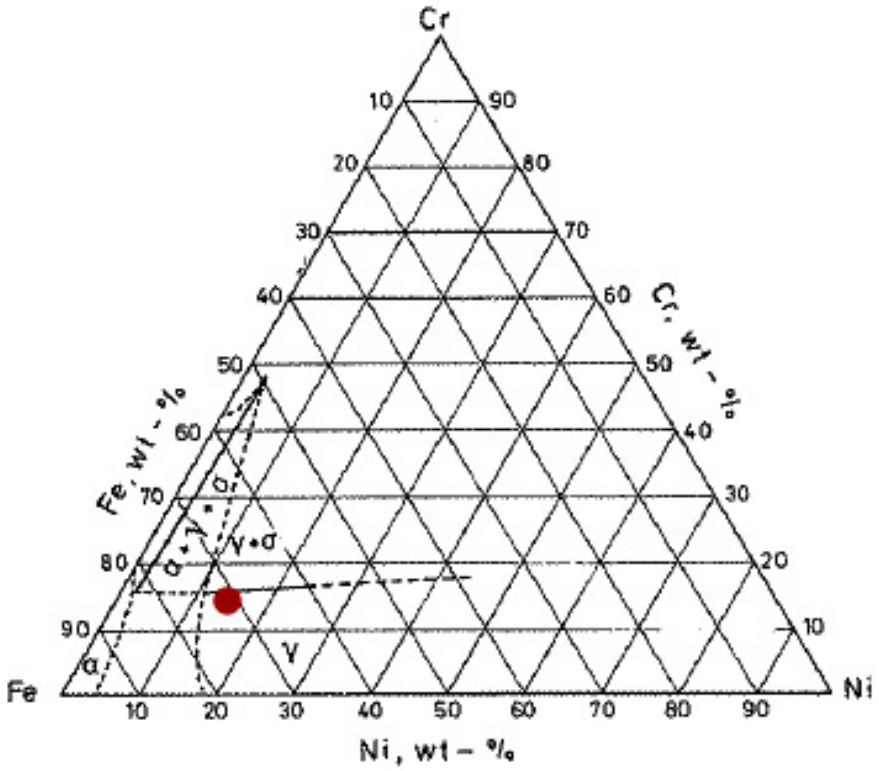

Figure 2.25: 550°C isotherm of the Fe-Ni-Cr phase diagram [87, 88]. A circle represents the area in which the composition for 316 stainless steel lies.

Table 2.4: Mechanical properties of AISI 316 steel [86].

316 Mechanical Properties	
Tensile Strength	515 MPa
Yield Strength	205 MPa
Elongation	40 %
Hardness	95 HRB

2.5.4 Steel of 1074 Composition

AISI 1074, a low-alloy steel with a eutectoid carbon content, will be useful in this research for heat treatment studies involving decarburization. Because of the eutectoid composition of the alloy (see Table 2.5), a fully pearlitic microstructure is observed upon slow cooling, thus allowing for simple measurement of decarburization depth through microstructural observation. In the case of AISI 1074, upon decarburization, ferrite grains are observed rather than a pearlitic microstructure.

Table 2.5: Composition of AISI 1074 steel.

Element	Composition (wt%)
C	0.7-0.8
Mn	0.5-0.8
P	0.04 (max)
S	0.05 (max)

CHAPTER III

EXPERIMENTAL METHODS

The following chapter discusses the methods employed to address the objectives of the research, as listed in Chapter I. First, sample fabrication methods are presented, followed by several methods to study the reduction behavior and properties of the reduced strip. This includes density and porosity measurements, as well as thermogravimetric analysis and dilatometry. Next, methods necessary for the determination of gas carburization parameters, including thermodynamic considerations to avoid metal dusting, are presented. Techniques for heat treatment studies, as well as mechanical property and microstructural investigations, are then outlined. Lastly, the details regarding decarburization studies are presented.

3.1 Sample Fabrication

For extrusions of iron strip and strip with 4140 and 316L compositions, metal oxide and metal powders were mixed such that after reduction, the composition of interest, without the presence of carbon, would be achieved. Samples were made following the method of Hurysz *et al*. [7], though some deviations from the original method were made. The powders were mixed in 1000g batches and ball-milled for 24 hours with 20 mm mixing media. Powders were then mixed with binder (A4M Methocel®, Dow Chemical Co., Midland MI) and lubricant (100S Pegosperse®, Lonza, Fair Lawn, NJ), and ball-milled for an additional 24 hours. The powder mixture was then blended in a commercial mixer and deionized water was sprayed into the mixture to form a paste. The paste was removed from the mixer and compounded manually before being placed in a hand extruder with a circular cross-section of approximately 2 cm. The hand extruder was sealed and a roughing pump was used to pull a vacuum on the paste for 2 minutes to compact the paste prior to

the final extrusion process. The paste was hand extruded and then stored in vacuum sealed bags until extrusion through the die of interest could be performed. The paste was then extruded using a SATEC® (Norwood, MA) compression testing machine and laid flat to dry for 48 hours prior to heat treatment. Strip samples were covered with foam blocks and were weighted to ensure that the strip would not curl upon drying. Unless otherwise stated, the green extrusions were placed in a tube furnace under a flowing 10% H_2/Ar atmosphere and heated such that full reduction and sintering of the sample was complete. Figures 3.1 and 3.2 show schematics of the two extrusion geometries of interest in this study, a thin strip extrusion with wall thickness of 400 μm, and a waffle shape extrusion with diameter of 11 mm and wall thickness of 310 μm, repectively.

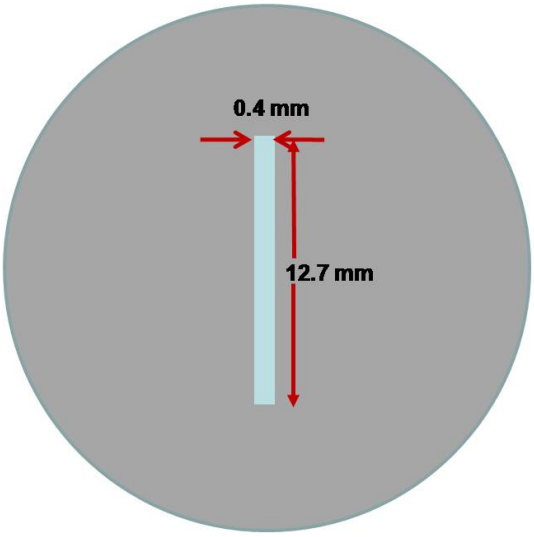

Figure 3.1: Schematic of the strip extrusion die used in this study.

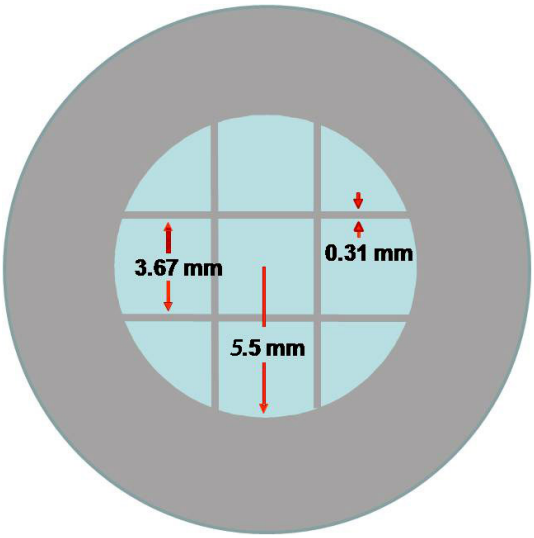

Figure 3.2: Schematic of the waffle extrusion die used in this study.

3.1.1 Fabrication of Iron Strip

Paste for the fabrication of iron strip was made using Fe_3O_4 powder (Ceramic Color and Chemical Manufacturing Co., New Brighton, PA), as well as lubricant and binder that was described previously. The batch composition necessary for optimal extrusion is listed in Table 3.1. After extrusion and air drying, the samples were heated under the schedule that is shown in Table 3.2.

Table 3.1: Batch requirements to produce a 1000g batch of Fe_3O_4 paste.

Raw Material	Weight (g)
Fe_3O_4	1000
Methocel	45.00
Pegosperse	4.50

Table 3.2: Heating schedule for the reduction and sintering of Fe_3O_4 extrusions.

Rate (°C/min)	Temperature (°C)	Dwell Time (min)
2	450	30
3	850	480
3	1300	180
5	25	–

3.1.2 Fabrication of Strip with AISI 4140 Composition (without carbon)

Two batch compositions were tested for the fabrication of strip with 4140 composition. In both batches, Fe_3O_4, Cr_2O_3 (Fisher Scientific, Hampton, NH), SiC (Atlantic Equipment Engineers, Bergenfield, NJ) and Mo metal (H.C. Stark Group, Newton, MA) powders were used. Manganese additions were achieved through the use of MnO_2 powder in the first batch, while Mn metal powder was used in the second batch. Batch requirements, including the mass of metal oxide powders and additives for Batch 1 and 2 are shown in Table 3.3 and 3.4, respectively.

Table 3.3: Batch requirements to produce a 1000g batch of 4140 paste (Batch 1 - MnO_2 powder used).

Raw Material	**Weight (g)**
Fe_3O_4	971.23
Cr_2O_3	10.62
MnO_2	12.65
SiC	2.59
Mo	2.91
TOTAL	**1000**
Methocel	45.00
Pegosperse	4.50

Table 3.4: Batch requirements to produce a 1000g batch of 4140 paste (Batch 2 - Mn powder used).

Raw Material	**Weight (g)**
Fe_3O_4	976.16
Cr_2O_3	11.67
Mn	7.26
SiC	3.11
Mo	1.81
TOTAL	**1000**
Methocel	45.00
Pegosperse	4.50

Samples were heated following three different schedules, all in a 10% H_2/Ar atmosphere, to study the reduction and sintering of the strip. These schedules are shown in

Table 3.5.

Table 3.5: Heating schedules for the reduction and sintering of 4140 extrusions.

Schedule	Rate (°C/min)	Temperature (°C)	Dwell Time (min)
A	3	900	0
	0.2	950	0
	2	1250	240
	4	RT	–
B	3	450	30
	3	850	480
	1	1300	240
	5	25	–
C	3	450	30
	1	850	480
	1	1300	240
	5	25	–

3.1.3 Fabrication of Strip with AISI 316 Composition (without carbon)

For the production of paste with 316L composition (without carbon), Fe_3O_4, Cr_2O_3, Mo, and NiO (Ceramic Color and Chemical Manufacturing Co., New Brighton, PA) powders were mixed with binder and lubricant. Batch requirements for 316 steel are shown in Table 3.6.

Table 3.6: Batch requirements to produce a 1000g batch of 316 paste.

Raw Material	Weight (g)
Fe_3O_4	689.57
Cr_2O_3	180.99
NiO	111.24
Mo	18.21
TOTAL	**1000**
Methocel	45.00
Pegosperse	4.50

For the case of 316 strip, heat treatment was first attempted in a 10% H_2/Ar atmosphere. However, reduction moved to a pure hydrogen atmosphere to allow for the reduction of the sample in a timely manner. The heating parameters investigated for the full reduction of

316 strip of 400 μm green thickness are given in Table 3.7. In general, samples were heated to 1350°C and allowed to soak for between 2 and 50 hours to determine the time necessary for full reduction of the strip.

Table 3.7: Heating schedules for the reduction and sintering of 316 extrusions.

Schedule	Rate (°C/min)	Temperature (°C)	Dwell Time (min)	Atmosphere
a	1	1350	2	10% H_2/Ar
	1	RT	–	
b	3	450	30	10% H_2/Ar
	1	850	600	
	1	1300	240	
	5	25	–	
c	3	450	30	100% H_2
	1	1350	120	
	5	25	–	
d	3	450	30	100% H_2
	1	1350	600	
	5	25	–	
e	3	450	30	100% H_2
	1	1350	720	
	5	25	–	
f	3	450	30	100% H_2
	1	1350	1200	
	5	25	–	
g	3	450	30	100% H_2
	1	1350	1800	
	5	25	–	
h	3	450	30	100% H_2
	1	1350	2400	
	5	25	–	
i	3	450	30	100% H_2
	1	1350	3000	
	5	25	–	

3.2 Density and Porosity Measurements

Density measurements of reduced and sintered Fe, 4140 and 316 strip were performed using the Archimedes method. Individual samples were first weighed dry, in air (W_D). Traditional methods of vacuuming the sample while immersed in water had to be altered to prevent oxidation of the samples during measurement. Samples were thus placed in a weigh boat, floated on top of water in a vacuum canister and a roughing pump was used to pull a vacuum in the canister. After 20 minutes, the sample was allowed to drop into the water before venting the canister. The sample was then weighed while suspended in water (W_{SS}). Lastly, surface moisture on the sample was removed using a damp towel and the sample was weighed again in dry air (W_S). In order to determine the percent theoretical density of the reduced and sintered samples, the following steps were taken:

1. The bulk fired volume was determined following Equation 19

$$BFV = \frac{W_S - W_{SS}}{\rho_L} \tag{19}$$

   where ρ_L is the density of the liquid

2. The fired bulk density was determined using Equation 20

$$FBD = \frac{W_D}{BFV} \tag{20}$$

3. The percent theoretical density was determined using Equation 21

$$\%\rho_{th} = \frac{FBD}{\rho_{th}} \times 100 \tag{21}$$

   where ρ_{th} is the theoretical density.

Additionally, the closed porosity (ϕ_C) and open porosity (ϕ_O) can also be determined from this information, following Equations 22 and 23. The total porosity (ϕ_T) is the sum of these two values, shown in Equation 24.

$$\phi_C = 1 - \frac{W_D}{\rho_{th}(W_D - W_{SS})} \tag{22}$$

$$\phi_O = \frac{W_S - W_D}{W_S - W_{SS}} \tag{23}$$

$$\phi_T = \phi_C + \phi_O \tag{24}$$

3.3 Thermogravimetric Analysis

The reduction behavior of the metal oxide powders necessary for the formation for 4140 and 316L pastes, as well as the Methocel® binder, were investigated using thermogravimetric analysis (TGA). Samples of 4140 and 316L extruded tape, as well as Fe_3O_4, Cr_2O_3, NiO, and Methocel® powder, were investigated using a Jupiter® (Netzsche Instruments, Germany) simultaneous TG-DSC. Samples of each, weighing approximately 60mg, were heated in a 2% H_2/Ar atmosphere flowing at approximately 50 mL/min. The samples were heated at 1°C/min to 1350°C. Due to the sensitivity of the TGA, atmospheres with higher hydrogen contents, which would increase the reduction rate, were unable to be investigated.

3.4 Dilatometry

The shrinkage of 4140 extrusions upon heating in H_2/Ar gas mixtures was determined using a contact dilatometer. A Linseis (Robbinsville, NJ) L76 Platinum single pushrod dilatometer with an alumina pushrod was used for these experiments. Dilatometric measurements were done on waffle shaped extrusions (see Figure 3.3), as strip samples do not provide the structural support necessary for use in the dilatometer. Waffle-shaped samples were first extruded using the methods described in Section 3.1. Then, the extrusions were cut to lengths of approximately 8-9 mm using a vertical band saw. The cut ends were then sanded by hand using a fine-grained SiC grinding paper, such that the ends were parallel. Samples were placed in the dilatometer, using small alumina plates on each end to ensure even

contact with the pushrod and heated under the schedules and atmospheres that are listed in Table 3.8. Samples weighed approximately 0.5-0.6 grams prior to treatment.

Figure 3.3: Photograph of a green 4140 waffle extrusion. The scale is in millimeters.

Table 3.8: Heating schedules for dilatometric studies of 4140 extrusions.

Schedule	Rate (°C/min)	Temperature (°C)	Dwell Time (min)	Atmosphere
1	1	1350	0	2% H_2-Ar
	1	1350	0	
2	3	450	30	10% H_2-Ar
	3	850	480	
	1	1300	240	
	5	25	–	

Dilatometric measurements on the shrinkage of 316 extrusions in 100% H_2 could not be performed due to the limitations of the equipment. The dilatometer used in this study requires an S-type thermocouple (Pt, Pt-10%Rh), which subsequently embrittles in hydrogen at elevated temperatures.

3.5 Gas Carburization

In most traditional gas carburization techniques, the sample is enriched with carbon and then held at a high temperature to allow for diffusion to occur (see Section 2.2.1). However,

due to the thin nature of the samples and expected fast carburization times, carburization experiments in this study do not have a separate "carbon diffusion" step. Thus, the carburizing gas is introduced and remains unchanged until cooling of the samples. The following section will first detail the thermodynamics involved in determining the gas carburization parameters that would not result in metal dusting of iron and 4140 strip. Further sections will detail the specific gas carburization parameters used for experiments with iron, 4140 and 316L strip.

3.5.1 Thermodynamic Considerations to Avoid Metal Dusting

In order to avoid metal dusting, it is essential to choose parameters such that the formation and subsequent disintegration of Fe_3C does not occur. Thus, the chemical potential of carbon in various CO/CO_2 atmospheres was plotted along with the standard Gibbs free energy of formation (ΔG^o) of Fe_3C, as can be seen in Figure 3.4. The chemical potential of carbon in the atmosphere was determined through Equation 25.

$$\Delta\mu_C = -\Delta G^o + RTln\frac{X_{CO}^2}{X_{CO_2}} \cdot P \tag{25}$$

where X_{CO} and X_{CO_2} are the mole fractions of carbon monoxide and carbon dioxide in the atmosphere, respectively. P is the total pressure of the system, and ΔG^o is the standard Gibbs free energy of formation of CO, following the equation $C + CO_2 \longrightarrow 2\,CO$.

Provided the chemical potential of carbon in the atmosphere is lower than the standard Gibbs free energy of formation for Fe_3C, metal dusting is not thermodynamically favorable, as the formation of Fe_3C is not favored. As such, 1000°C was chosen for the carburization temperature for the gas carburization experiments of iron and 4140, such that high CO-containing atmospheres could still be used with limited threat of metal dusting. Additionally, it can be seen in the figure that at 1000°C, ΔG^o for Fe_3C crosses 0, indicating that the carbide becomes more stable. Thus, it is expected that if Fe_3C is formed, at 1000°C it will not deteriorate, thus avoiding metal dusting in this manner as well.

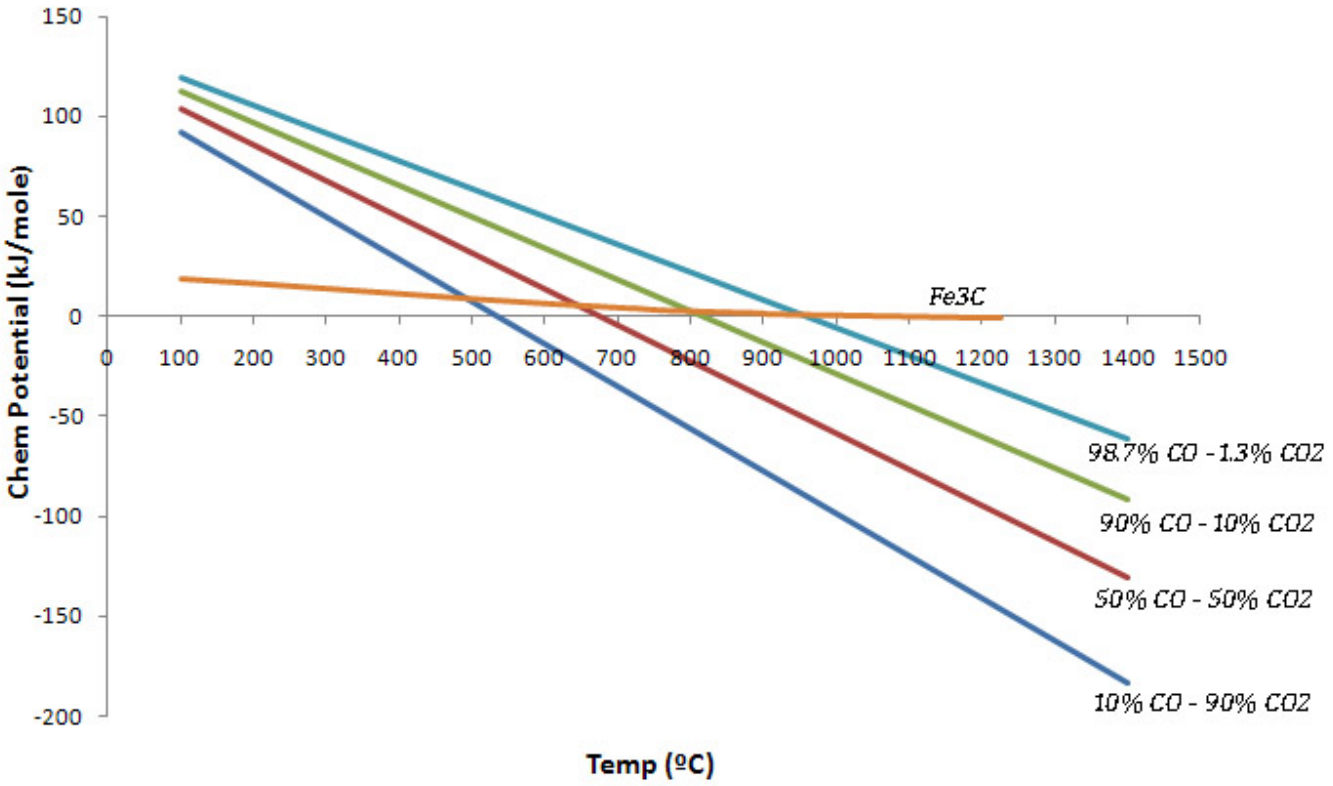

Figure 3.4: Standard Gibbs free energy of formation of Fe_3C plotted with the chemical potential of carbon for several CO/CO_2 atmosphere compositions. Metal dusting has the potential to occur if ΔG^o for Fe_3C is lower than the chemical potential of carbon in the atmosphere at the specified temperature.

3.5.2 Gas Carburization of Iron Strip

To investigate that the parameters chosen were such that gas carburization was successful and metal dusting was avoided, preliminary gas carburization investigations were carried out on iron strip. A TGA apparatus with a Cahn Microbalance design, as is shown in Figure 3.5, was used such that weight changes during carburization could be observed.

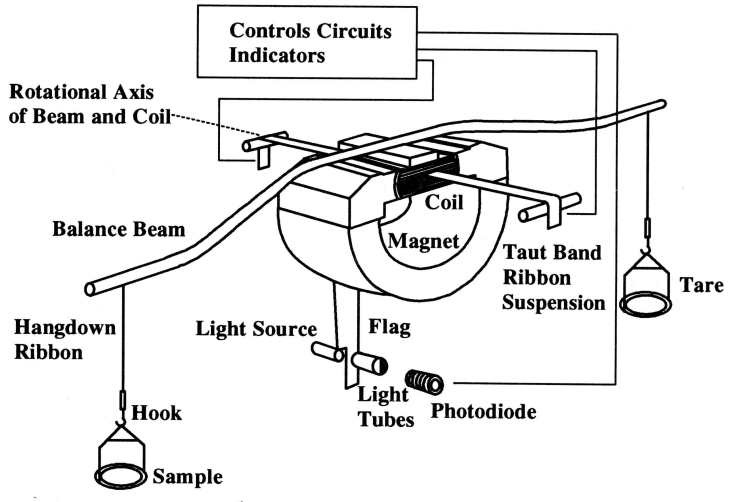

Figure 3.5: Cahn microbalance apparatus [89].

In order to prevent oxidation, samples were heated to 1000°C in a premixed 4% H_2/Ar atmosphere. At 1000°C, the carburizing atmosphere of carbon monoxide and carbon dioxide corresponding to the equilibrium carbon surface concentration of interest is introduced. Figure 3.6 shows a plot of the percent of CO in a CO/CO_2 atmosphere necessary to reach a certain equilibrium surface concentration at 1000°C, as was determined by R. Smith [38]. Unless otherwise stated, the atmospheres used for the carburization of samples in this study were determined through Smith's results. For this particular case, it was the goal to carburize the sample such that the microstructure was fully pearlitic, thus showing that compositions around the eutectoid could be reached. Subsequently, a 98.7% CO/ 1.3% CO_2

atmosphere was used, corresponding to C_s = 1.0 wt% C. Mass flow controllers (MKS Instruments, Andover, MA) were used to control the carburizing atmosphere composition.

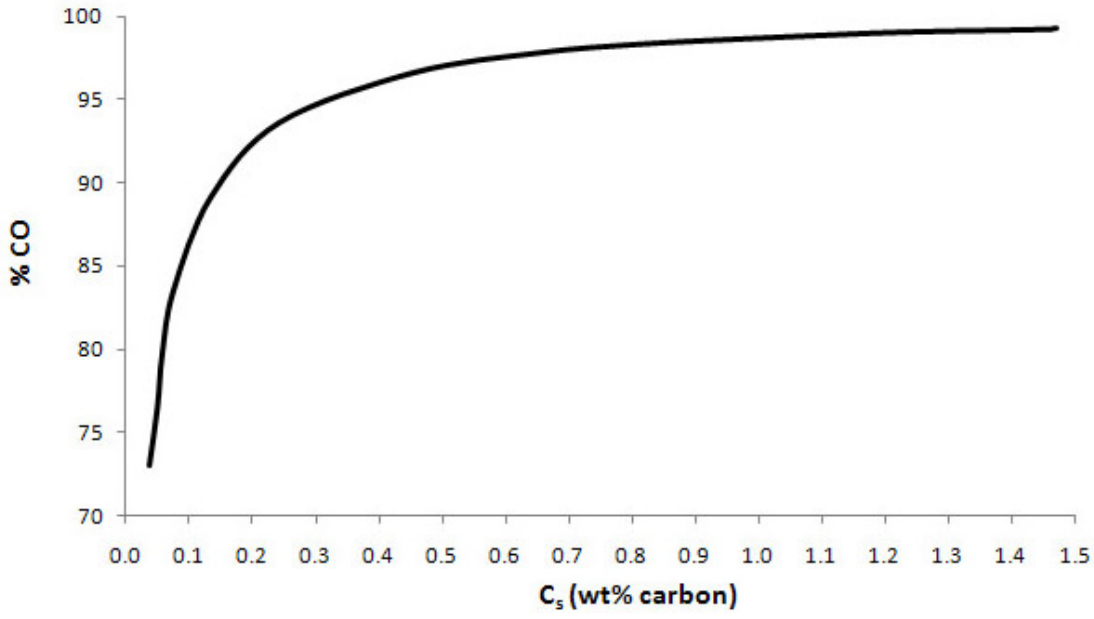

Figure 3.6: Equilibrium surface concentration of carbon (C_s) associated with the percentage of carbon monoxide in a CO/CO_2 atmosphere, after Smith [38].

The time necessary for the carbon content to reach 0.8 wt% C half way through the sample was estimated through the use of the erf solution to Ficks second law (Equation 8), which is most commonly used as an estimate in carburization practices. This resulted in a predicted carburization time of 65 minutes necessary to surpass the eutectoid composition in the center of the sample. To this end, the sample was held in the carburizing atmosphere for 2 hours and 15 minutes to allow ample time for equilibration of the system while data was taken in the TGA. Samples were then cooled in a 4% H_2/Ar atmosphere at a rate of 4°C/min.

3.5.3 Gas Carburization of Samples with 4140 Composition

3.5.3.1 4140 Strip

Samples of 4140 strip were carburized in a tube furnace with atmospheres corresponding to an equilibrium surface concentration of approximately 0.4 wt% C and 1.0 wt% C. Like the iron strip, samples were heated to 1000°C at a rate of 3°C/min in a premixed 4% H_2/Ar atmosphere flowing at approximately 70 mL/min to prevent oxidation of the sample. At 1000°C, the carburizing atmosphere corresponding to the equilibrium carbon surface concentration of interest was introduced. Specifically, the following two atmospheres were investigated:

- 98.7% CO - 1.3% CO_2 such that C_s = 1.0 wt% C
- 96.15% CO - 3.85% CO_2 such that C_s = 0.40 wt% C

Samples were then cooled under high purity argon, rather than 4% H_2/Ar as was done with iron strip (Section 3.5.2), at a flow rate of approximately 70 mL/min. The argon was run through a Drierite® (W. A. Hammond Drierite Co. Ltd , Xenia, OH) canister in order to scrub any water vapor from the gas. Additionally, the argon gas was run through a Gatekeeper® (Entegris Inc., Chaska, MN) inert gas purifier to further prevent oxidation and significant decarburization upon cooling. Samples were cooled at a rate of 4°C/min. Flow of CO and CO_2 were controlled using mass flow controllers (Aalborg, Orangeburg, NY), while Ar and premixed 4%H_2/Ar gas flows were controlled using glass tube, variable flow meters (Key Instruments, Trevose, PA).

In order to demonstrate that eutectoid compositions could be reached quickly in a low alloy steel using the gas carburization process, 4140 tape samples carburized with C_s = 1.0 wt% C were first held in the carburizing atmosphere for 65 minutes, as this was the time necessary as estimated through the erf solution to Fick's second law. Results from these experiments resulted in further carburization experiments in which samples were held in the carburizing atmosphere for 30 minutes, where the total flow rate of the CO/CO_2 atmosphere

was 400 or 800 mL/min.

4140 tape samples were then carburized with C_s = 0.40 wt% C, for times ranging from 15 to 60 minutes under flow rates of 400 and 800 mL/min in order to determine the time necessary in the carburizing atmosphere to reach the carbon composition of a 4140 steel (0.37-0.43 wt% C). In addition, several samples were carburized where C_s = 0.40 wt% C as determined mathematically by Stanley [25], rather than through experiments reported by Smith [38] (see Section 2.2.1.1) in order to determine whose predictions were closer to the experimental results in this study. In this case, the atmosphere was 97.2% CO - 2.8% CO_2. This corresponds to C_s = 0.56 wt% C according to R. Smith. In this case, all samples were carburized for 30 minutes. Experimental parameters, as well as samples names, are summarized in Table 3.9. Sample names beginning with the prefix "4140_2_..." were made from Batch 2, as given in Section 3.1.2, while all others are from Batch 1.

Table 3.9: Gas carburization parameters for 4140 strip samples.

Sample Name	**Carburization Time (min)**	**CO(%)**	C_s **(Smith)**	C_s **(Stanley)**	**Flow Rate (mL/min)**
4140_carb_15	30	96.15	0.4	0.28	400
4140_carb_16	45	96.15	0.4	0.28	400
4140_2_carb_4	15	96.15	0.4	0.28	800
4140_2_carb_15	15	96.15	0.4	0.28	800
4140_2_carb_31	15	96.15	0.4	0.28	800
4140_carb_23	30	96.15	0.4	0.28	800
4140_2_carb_26	30	96.15	0.4	0.28	800
4140_2_carb_27	30	96.15	0.4	0.28	800
4140_2_carb_28	30	96.15	0.4	0.28	800
4140_carb_24	45	96.15	0.4	0.28	800
4140_2_carb_3	60	96.15	0.4	0.28	800
4140_2_carb_25	60	96.15	0.4	0.28	800
4140_2_carb_29	60	96.15	0.4	0.28	800
4140_2_carb_30	60	96.15	0.4	0.28	800
4140_2_carb_13	30	97.2	0.56	0.4	400
4140_2_carb_17	30	97.2	0.56	0.4	800
4140_2_carb_33	30	97.2	0.56	0.4	800
4140_2_carb_34	30	97.2	0.56	0.4	800

3.5.3.2 4140 Hollow Spheres

Hollow spheres of 4140 composition without carbon were made at Deep Springs Technology (Toledo, OH) through a proprietary coating process. The carburized spheres had a size range of approximately 1.3-2.0 mm in diameter and wall thicknesses of approximately 25-75 μm. For carburization experiments on hollow spheres, approximately 40-50 spheres were chosen randomly for each heat treatment condition. Twenty spheres from each batch were reserved for compression testing and the remainder were used for microscopy. Table 3.10 shows the carburization parameters used for experiments on 4140 hollow spheres. Spheres were carburized for 60 minutes to ensure that carbon reached through the sample wall.

Table 3.10: Gas carburization parameters for 4140 hollow sphere samples.

Sample Name	**Carburization Time (min)**	**CO(%)**	**Flow Rate (mL/min)**
4140_p_11	60	98.7	800
4140_p_12	60	97	800

3.5.4 Gas Carburization of Samples with 316 Composition

Prior to carburization of austenitic stainless steels, the passive Cr_2O_3 layer was first removed from the samples through the electroplating of iron onto the surface of the samples. Samples were electroplated under a current of 2-3 Amps in a 24% (w/v) $FeSO_4 \cdot 7\,H_2O$ (Fisher Scientific, Hampton, NH), Deionized H_2O solution at approximately 40°C. Previous research [51–53] suggests that a 15 μm layer of iron is all that is necessary to sufficiently depassivate the surface of 316 prior to carburization. Faraday's law, as shown in Equation 26, was thus used to determine the time necessary for electroplating.

$$W = \frac{I \cdot t \cdot A}{n \cdot F} \tag{26}$$

where W is the weight of the plated metal (g), I is the current (Amperes), t is time (seconds), A is the atomic weight of the metal, n is the valence of the dissolved metal (equivalents/-mole), and F is Faraday's constant.

To determine the thickness of the plating, Equation 27 can then be combined with Faradays Law (Equation 26) to give Equation 28.

$$T = \frac{W \cdot 10000}{\rho \cdot S} \tag{27}$$

where T is the thickness of the coating (μm), ρ is the density of the metal (g/cm^3) and S is the surface area of the sample being plated (cm^2).

$$T = \frac{I \cdot t \cdot A \cdot 10000}{n \cdot F \cdot \rho \cdot S} \tag{28}$$

316 samples that were carburized had a surface area of approximately 4-5 cm^2 and were thus electroplated with a current of 2-3 Amps for 90-120 seconds to reach the desired electroplated thickness of approximately 15 μm.

Calculations based on the carburization data of Stanley [25] were used to estimated the atmosphere necessary for the carburization of 316 samples such that C_s = 3.4 wt% C. From this information, the P_{CO}^2/P_{CO_2} ratio necessary at any temperature can be determined. It was calculated from this information that 61.1% CO - 38.9% CO_2 was the required atmosphere. To keep CO levels out of explosive limits, it was necessary to use an Argon carrier gas in 316 gas carburization experiments as well, while maintaining the same P_{CO}^2/P_{CO_2} ratio. As such, carburization was carried out at 525°C for times up to 25 hours in a 7.6% CO - 2.4% CO_2 - 90% Ar atmosphere. Table 3.11 shows the carburization parameters for the samples in this study.

Because the temperature range where carburization of 316 steel can be performed without the formation of carbides is limited, the carburization parameters are not able to be chosen such that metal dusting is not thermodynamically favorable. The chemical potential of carbon in the CO/CO_2 atmosphere necessary for these experiments was plotted in

Figure 3.7 along with the standard Gibbs free energy of formation (ΔG^o) of Fe_3C, similarly to what was shown in Section 3.5.1. It is evident from the figure that at 525°C, the formation of Fe_3C is thermodynamically favorable, thus metal dusting has the potential to occur in carburization experiments of 316 samples.

Table 3.11: Gas carburization parameters for 316 samples.

Sample Name	**Carburization Time (hrs)**	C_s **(Stanley)**	**Flow Rate (mL/min)**
316_carb_3	25	3.4	1000
316_carb_4	7	3.4	1000

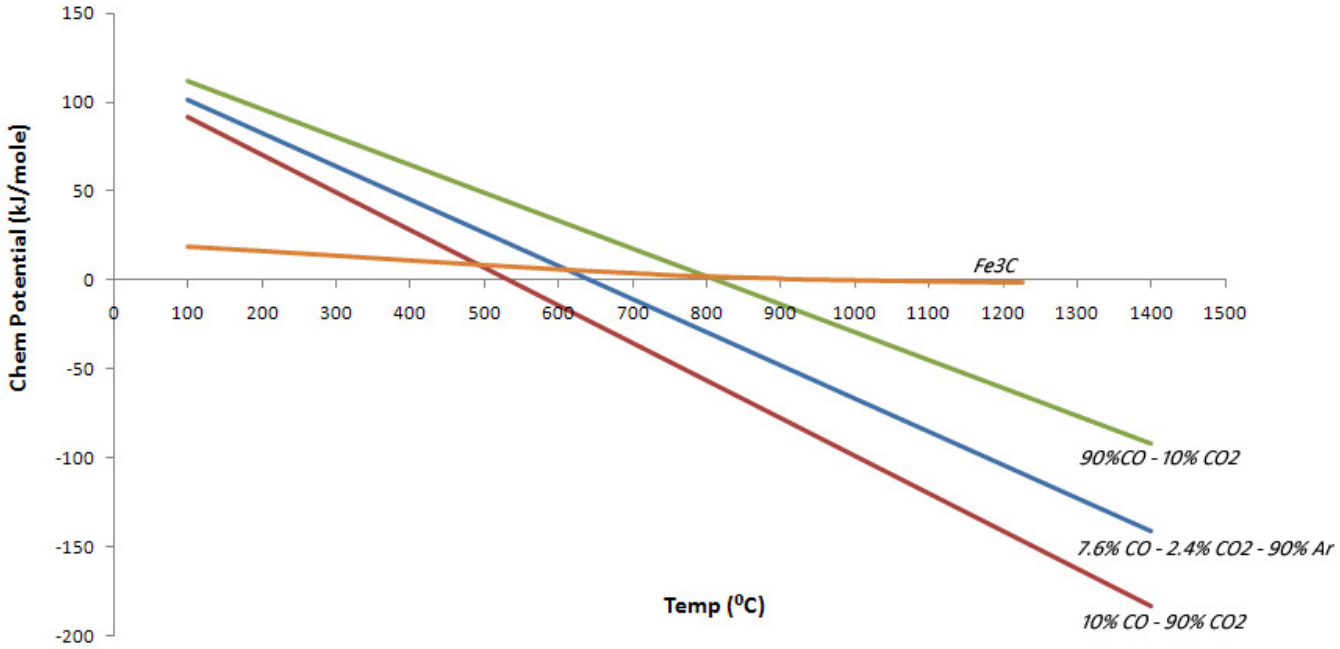

Figure 3.7: Standard Gibbs free energy of formation of Fe_3C plotted with the chemical potential of carbon for several CO/CO_2 atmosphere compositions, including that which is necessary for the carburization of 316 steel at 525°C.

3.6 Heat Treatment Studies

Heat treatment experiments of previously carburized 4140 strip samples were performed using a salt bath and oil quench furnace. The quenching furnaces were manufactured by Upton Industries (Roseville, MI) for the planned experiments. The salt bath furnace was filled with Ausquench salt (Park Metallurgical Corp., Detroit, MI), a propriety blend of nitrate and nitrite based salts. The working temperature range of this salt mixture is 190°C - 590°C. Marquench oil (Park Metallurgical Corp., Detroit, MI) was used in the oil quench furnace, where the working temperature range is up to 176°C.

The samples were first austenitized in a vertical tube furnace (MTI Corp., Richmond, CA) that was mounted on a trolley such that it could be moved over both the salt bath and oil quench furnaces. Figure 3.8 shows a photograph of the laboratory setup. The samples were hung in the vertical tube furnace using stainless steel wire and were austenitized at 850°C for 10 minutes. Then, the samples were lowered into the quenching media as fast as possible and allowed to soak for varying times such that bainitic and martensitic structures would be observed. This information was estimated through the isothermal heat treatment diagram that was shown in Figure 2.23 in Section 2.5.2. Table 3.12 shows the parameters used for heat treatment studies of carburized 4140 samples.

All samples were heat-treated simultaneously with a scrap of conventionally produced 4140 steel (labelled ”control” in Table 3.12), such that the mechanical properties of the samples could be compared . Three of the control samples, 4140_M3_Control, 4140_B1_Control and 4140_B2_Control, were heated to 1000°C and held for 30 minutes in Argon, prior to the experiments, such that grain growth that occurs during carburization of 4140 samples could also be replicated.

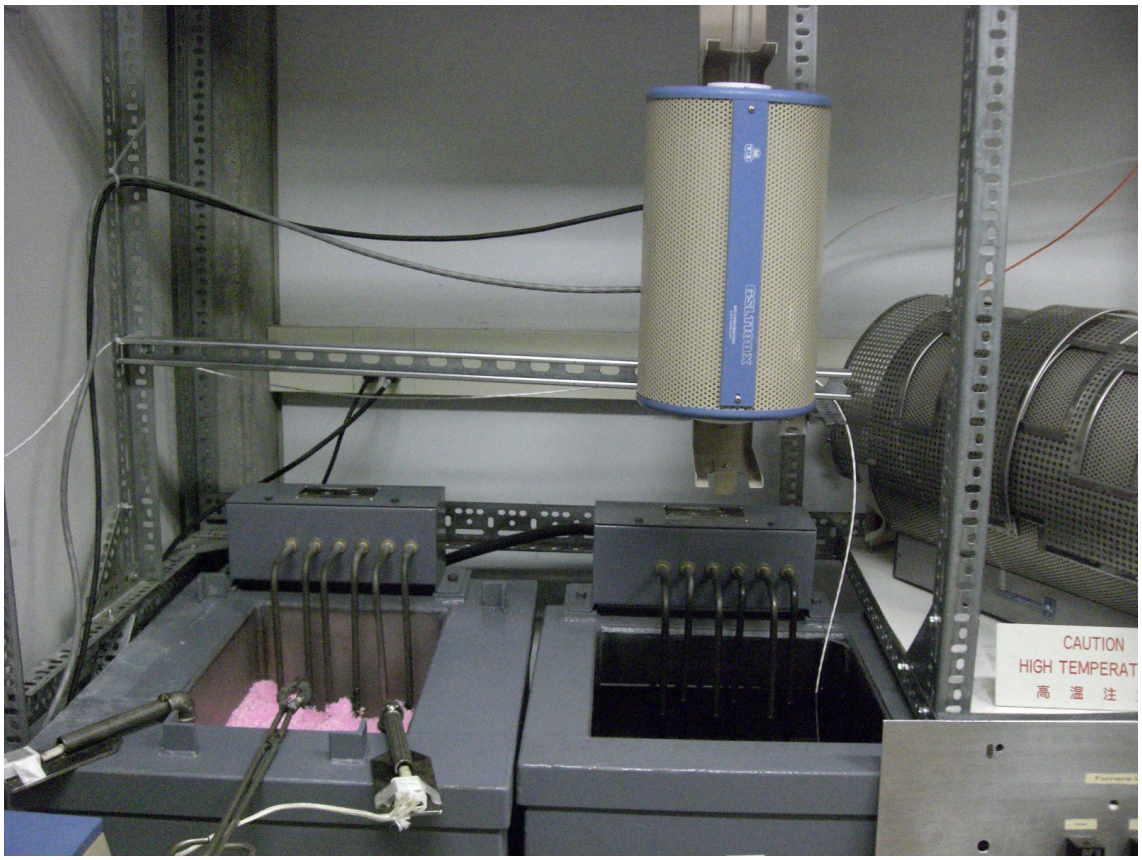

Figure 3.8: Laboratory setup of salt bath (left) and oil quench (right) furnaces. A vertical tube furnace is mounted on a trolley such that samples can be heat-treated then dropped into the baths when necessary.

Table 3.12: Heat treatment parameters of carburized 4140 steel.

Sample Name	Treatment Temp. (°C)	Treatment Time (min)	Furnace Used
4140_2_carb_27 4140_M1_Control	50	5	Oil Quench
4140_carb_16 4140_M2_Control	50	2	Oil Quench
4140_carb_23 4140_M3_Control	50	2	Oil Quench
4140_carb_23 4140_B1_Control	400	60	Salt Bath
4140_carb_23 4140_B2_Control	375	60	Salt Bath

3.7 Microstructural Analysis

Thin tape samples were prepared for microscopic inspection using standard metallographic techniques. Samples were hot mounted such that their cross-section was visible using IsoFast® (Struers Inc., Cleveland, OH) mounting resin. Hollow sphere samples were cold mounted using Epofix® (Struers Inc., Cleveland, OH) mounting resin, and polished such that the cross-sections were exposed. Samples were polished with SiC grinding paper of grit size 320, 800, 1200, 2400 and 4000, consecutively. Final polishing was done using 1.0, 0.3 and 0.05 μm alumina suspensions, and samples were then rinsed in ethanol to prevent oxidation of the polished surface. Prior to microscopic investigation, 4140 samples were etched using a 2% Nital (2% nitric acid, balance ethanol) solution for approximately 40 seconds. 316 samples were etched with a 40mL HCl, 5g $CuCl_2$, 30mL H_2O, 25mL ethanol mixture for approximately 2 minutes and 45 seconds.

Optical microscopy was carried out using a LEICA DM IRM inverted research microscope (LEICA Microsystems Inc., Deerfield, IL), while scanning electron microscopy

(SEM) was done using both a LEO 1530 and LEO 1550 field emission SEM (Carl Zeiss SMT Inc., Peabody, MA), in which both were equipped with energy dispersive spectroscopy (EDS) capabilities. Carbon contents, post carburization, were determined using a stereographic analysis. Point counting was used to determine the volume fraction of pearlite in the microstructures, and errors were calculated using the t-distribution, as is given by the probability density function shown in Equation 29. Then, volume fraction measurements were used to estimated carbon contents through the use of the lever rule.

$$F(z) = k_m \int_{-\infty}^{z} (1 + \frac{u^2}{m})^{-\frac{m+1}{2}} \, du \tag{29}$$

where there are m degrees of freedom.

Specifically, to determine the volume fraction of pearlite colonies, the following steps were taken:

1. A test grid of 56 points was placed N times on several fields of view of the specimen cross-section.

2. The average number of times a single test grid intersected a pearlite colony (P^{Pearl}) was calculated.

3. P^{Pearl} was divided by the total number of points on the test grid ($P_T = 56$) to determine the volume fraction of pearlite colonies (V_v^{Pearl}).

To determine the error associated with the measurements using the t-distribution, the following calculations are necessary:

1. Based on the significance level chosen ($\gamma = 0.95$ in this case), the parameter c is determined using t-distribution tables such that $F_m(c) = \frac{1}{2}(1 + \gamma)$ where $m = N - 1$.

2. The term k is calculated, as $k = c\sqrt{\frac{s^2}{N}}$ where s^2 is the sample variance.

3. The error associated with the volume fraction measurement can then be calculated as $\frac{k}{P_T}$.

Thus, there is a 95% probability that the volume fraction of pearlite lies within the range $V_v^{Pearl} \pm \frac{k}{P_T}$ for the calculations used in this study.

3.8 Mechanical Properties Testing

3.8.1 Microhardness Testing

3.8.1.1 4140 Samples

Vickers microhardness of carburized 4140 samples that were cooled slowly were performed on a LECO MHT Series 200 Vickers/Knoop hardness tester (LECO Corp., St. Joseph, MI) with a test load of 100 gmf, indented over 15 seconds. Unless otherwise stated, each sample was indented four times to obtain an average microhardness value. In addition, the size of each indent was measured three times for accuracy. Vickers hardness tests were performed on several samples carburized at C_s = 0.40 wt% C. For comparison, a sample of conventionally made 4140 steel was heat-treated similarly to those that were carburized. The control sample was heated in Argon at 3°C/min to 1000°C and held at 1000°C for 30 minutes. The sample was then cooled at 4°C/min to room temperature and indented in the same manner as carburized samples.

Samples treated in the oil and salt bath furnaces were also indented along with control samples in the same manner. In the case of samples quenched in the oil bath furnace, a 300gmf test load was used, while a 100gmf test load was used for those treated in the salt bath furnace. Additionally, due to the porosity of the 4140 strip, several additional indentations were taken on sample 4140_carb_23 in areas where porosity seemed to be the lowest, such that further comparison with the hardness of the control sample could be made.

3.8.1.2 316 Samples

316 samples that were carburized at low temperatures were indented through the cross-section to determine if variations in hardness were present due to carbon diffusion into the sample. The indents were taken under a 100 gmf test load and measured three times for

accuracy. A sample of 316 strip that had not been carburized was also indented through the cross-section for comparison.

3.8.2 Compression Testing

Prior to compression testing, measurements of the mass (m) and average diameter (d_{avg}) were made on 20 spheres for each batch of tests, allowing for calculation of the sphere density (ρ_s) following Equation 30. Using the sphere density and the density of the wall material ($\rho_o \approx 8.03 g/cm^3$), the relative density (f_v) for each sphere was calculated from Equation 31. From this information, the wall thickness (t) of each sphere can be calculated through Equation 32.

$$\rho_s = \frac{m}{\frac{4}{3} \cdot \pi \cdot (\frac{d_{avg}}{2})^3} \tag{30}$$

$$f_v = \frac{\rho_s}{\rho_o} \tag{31}$$

$$t = \frac{\frac{d_{avg}}{2} \cdot f_v}{3} \tag{32}$$

Compression testing of 4140 hollow spheres was carried out on as-received samples (no carbon) and carburized samples where load (F) and displacement (D) data were collected. An MTS Insight^{TM} 2 (MTS Systems Corp., Eden Prairie, MN) testing system was used for compression tests and testing was performed under a rate of 0.8 mm/min. The strain (ϵ) on the spheres was calculated using Equation 33. In order to calculate the stress (σ), also referred to as *wall stress*, the load bearing area (LBA) was first calculated following Equation 34 such that the stress is normalized (due to varying sphere diameters). The observed data was corrected for compliance using a polynomial fit for measured compliance curves. From this information, a corrected displacement and thus corrected strain was calculated.

$$\epsilon = \frac{D}{d_{avg}} \tag{33}$$

$$LBA = \pi \cdot d_{avg} \cdot t \tag{34}$$

3.9 Chemical Analysis of Carbon Content

Several carburized samples were sent to Applied Technical Services, Inc. (Marietta, GA) for chemical analysis of carbon content, such that true carbon contents could be compared with that which was estimated through point counting. Carbon contents were determined using LECO combustion analysis techniques on samples weighing approximately 0.25-0.35g.

3.10 Decarburization Experiments

Because samples produced via the gas carburization technique most likely require subsequent heat treatment processes before reaching their desired microstructures and properties, samples of AISI 1074 steel of approximately 500 μm thickness were placed in a furnace in two different atmospheres; air and 4% H_2/Ar to study its decarburization behavior. The eutectoid composition of the steel, and thus fully pearlitic microstructure, allows for straightforward observation of decarburized areas of the sample after heat treatment. AISI 1074 samples were purchased (McMaster-Carr, Elmhurst, IL) as made through conventional techniques and not made via the metal oxide reduction process. Samples treated in air were placed in a preheated box furnace (Paragon Industries, Mesquite, TX) for 100 minutes at 700°C, 800°C, 850°C, 900°C, and 950°C. After 100 minutes, they were removed from the furnace and allowed to cool in air.

Because even low partial pressures of oxygen can result in the catastrophic oxidation of thin-walled structures, samples were also heat-treated at four different temperatures in a flowing 4% H_2/Ar atmosphere to study the decarburization kinetics and any microstructural changes that may occur during heat treatment while avoiding oxidation of the sample surface. Samples treated in 4% H_2/Ar were heated following the schedules as shown in

Table 3.13 in a tube furnace. With the exception of the samples heated to 700°C (heating schedule A), all samples were heated to the temperature of interest at a rate of 3°C/min, allowed to dwell for 60, 120 or 180 minutes and then cooled to room temperature at 4°C/min, resulting in a total of 12 heat-treated specimens. Samples held at 700°C (heating schedule A) had to first be austenitized in order to form a pearlitic microstructure, thus requiring the initial heating to 850°C before cooling to 700°C and being allowed to dwell for 60, 120, or 180 minutes.

Table 3.13: Heat treatment schedule for samples treated in 4% H_2/Ar.

Heating Schedule	**Rate (°C/min)**	**Temp (°C)**	**Dwell (min)**	**Rate (°C/min)**	**Temp (°C)**	**Dwell (min)**	**Rate (°C/min)**	**Temp (°C)**
A	3	850	30	4	700	60, 120, 180	4	25
B	3	850	60, 120, 180	4	25	–	–	–
C	3	950	60, 120, 180	4	25	–	–	–
D	3	1050	60, 120, 180	4	25	–	–	–

CHAPTER IV

RESULTS & DISCUSSION

The following chapter presents and discusses the results of experiments described in Chapter III. The results of thermogravimetric analysis, dilatometry and microstructural observations that were used to study the reduction of thin strip extruded from metal oxide powder mixtures are first presented. Next, results of gas carburization experiments of thin tape samples as well as for hollow sphere geometries are presented through microstructural observation, compositional analysis and mechanical properties testing. Observations from heat treatment studies are then shown through the use of SEM microscopy as well as through microhardness testing. Lastly, the results of decarburization studies are presented using microstructural investigation.

4.1 Thermogravimetric Analysis

Figure 4.1 shows the results for the TGA experiments for Fe_3O_4, NiO, Cr_2O_3 and Methocel powders heated in a 2% H_2/Ar atmosphere. Figure 4.1 a) shows the reduction of Fe_3O_4. From the figure, it can be seen that large amounts of weight loss begin at approximately 600°C. In Figure 4.1 b), it can be seen that NiO reduction begins at approximately 375°C and is completed by 1000°C. As evidenced by Figure 4.1 c), Cr_2O_3 powder cannot be be reduced without the presence of additional elements, due to its high stability. Thus, small amounts of weight loss shown in Figure 4.1 c) are due to the volatization of Cr_2O_3 at high temperature and are not due to the reduction of the oxide. Lastly, Figure 4.1 d) shows that Methocel reduction is completed very quickly at approximately 250°C. From the TGA data for Fe_3O_4, Methocel, and NiO powders, an explanation for TGA data collected for 4140 and 316L tape of 400 μm green thickness can be deduced.

Figures 4.2 and 4.3 show a plot of the percent original weight vs. temperature for the

reduction of 4140 and 316L green strip, respectively. Initial, small amounts of weight loss at low temperatures for both samples is likely due to evaporation of water from the green strip, while the weight loss step starting at approximately 225°C is due to the onset of burnout of the methocellulose binder in the strip. This can be confirmed through Figure 4.1 d).

In comparing Figures 4.2 and 4.3, a weight loss step occurring at approximately 375°C is evident for the reduction of 316L (Figure 4.3) due to the reduction of NiO, as nickel is not an alloying element necessary to achieve 4140 composition and is thus not in the 4140 powder mixture. In both cases, Fe_3O_4 and Cr_2O_3 reduction continue until all of the oxygen has been removed from the samples. Significant weight loss starting at approximately 600°C, in both cases, can be explained through the Ellingham diagram that was shown in Figure 2.3. At approximately 600°C, FeO becomes more stable than Fe_3O_4, thus reduction is more favorable. Due to lower amounts of Cr_2O_3 in the 4140 strip, reduction appears to be completed by approximately 1000°C, while for 316L, weight loss continues through to the end of the run. It is important to note that because only 2% H_2/Ar could be used for TGA experiments, reduction will be slower than what is observed when higher hydrogen ratios are used in the atmosphere. As such, the data gathered here serves only as an estimate to the temperatures and times necessary for the reduction of 4140 and 316L extruded tape. Results of further experimentation done on tape to determine the parameters necessary for full reduction of the strip is discussed in Section 4.4.

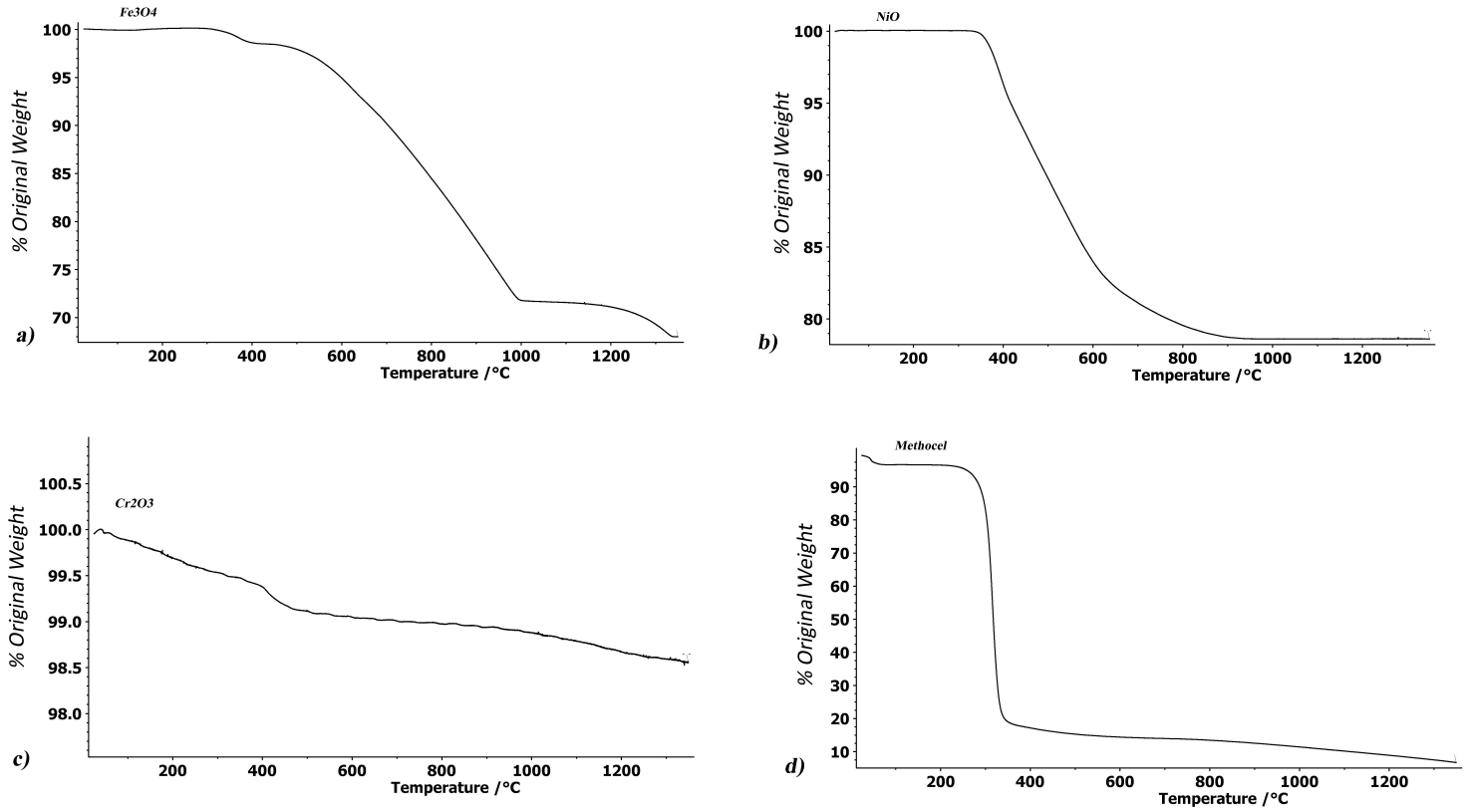

Figure 4.1: TGA data for a) Fe_3O_4, b) NiO, c) Cr_2O_3 and d) Methocel binder

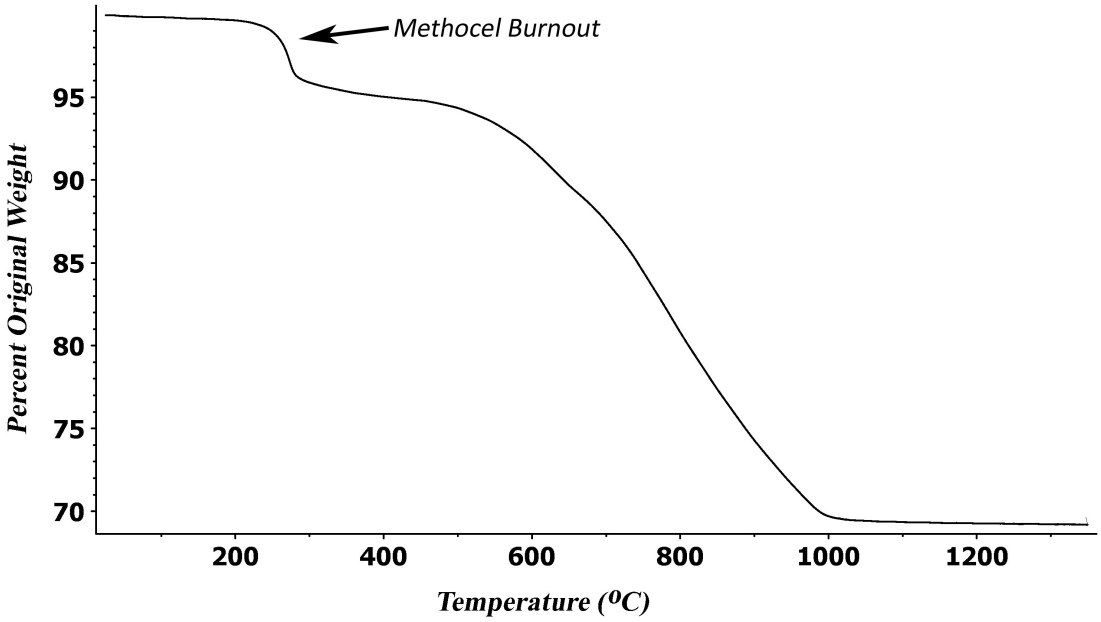

Figure 4.2: TGA data for the reduction of 4140 strip in 2% H_2/Ar.

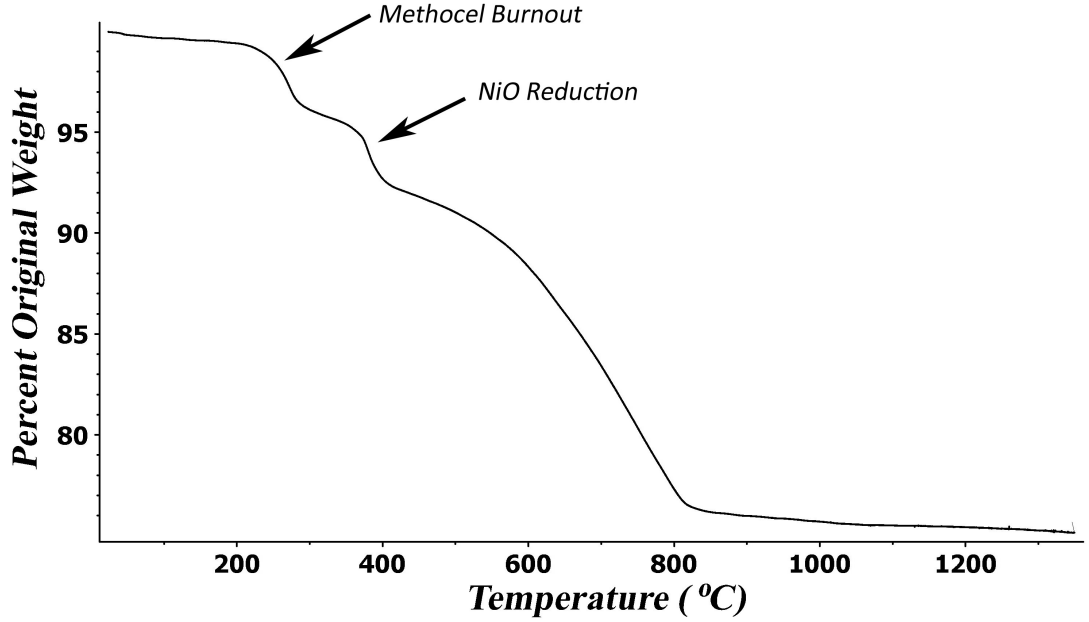

Figure 4.3: TGA data for the reduction of 316 strip in 2% H_2/Ar.

4.2 Density and Porosity Measurements

Achimedes density measurements on small strip (approximately 0.1 g fired dry weight) of reduced and sintered Fe_3O_4 and 4140 strip (without carbon) showed that, on average, the 4140 strip reached 82.79 ± 9.99% theoretical density while the Fe strip reached an average of 87.60 ± 14.28% theoretical density. 316 strip that was soaked for 40 hours at 1350°C (heating schedule 'i') reached an average density of 94.14 ± 7.23% theoretical density. Table 4.1 shows the average values for bulk density, theoretical density, and minimum and maximum values for the % theoretical density and bulk density for the strips tested.

Table 4.1: Density measurements on reduced and sintered Fe, 4140 and 316 strip, all without carbon.

Material	**Theoretical Density (g/cm^3)**	**Bulk Density (g/cm^3)**			**% Theoretical Density**		
		Avg	Max	Min	Avg	Max	Min
Fe	7.86	6.89	7.81	5.00	87.60	99.40	63.61
4140	7.75	6.42	7.52	5.04	82.79	97.11	65.02
316	8.00	7.53	7.92	6.69	94.14	99.04	83.65

Note in the table that the maximum % theoretical density for Fe, 4140, and 316 strip are 99.40%, 97.11%, and 99.04%, respectively. Because samples nearing 100% theoretical density have been achieved, it can be concluded that porosity is likely due to inadequate packing of the paste prior to extrusion, resulting in air bubbles in the paste. Table 4.2 shows the average values for open, closed, and total porosity as measured through the archimedes method.

Table 4.2: Measured porosity on reduced and sintered Fe, 4140 and 316 strip, all without carbon.

Material	**Average Porosity (Vol%)**		
	Open	Closed	Total
Fe	5.16	5.36	10.52
4140	10.46	7.49	17.95
316	2.18	2.84	5.02

4.3 Dilatometry

Figure 4.4 shows a plot of the shrinkage of 4140 extrusions when treated under the schedules listed in Table 3.8 (Section 3.4). The general shape of the curves are similar though shrinkage occurs at lower temperatures in a 10% H_2/Ar atmosphere (heating schedule 2). The trace taken in 2% H_2/Ar, was taken under the same heating schedule as was used for TGA experiments (Section 4.1). Comparison of the curves (Figure 4.2 and 4.4) shows that shrinkage of the waffle shaped extrusion appears sluggish compared to the observed weight loss in TGA experiments. This is simply due to the larger amount of material used in dilatometric measurements (approximately 0.006 g vs. 0.30 g). Thus the dilatometry trace as was taken in 10% H_2/Ar more closely matches what would be expected from the TGA data. This is due to the increased hydrogen in the system, allowing for faster reduction of the sample.

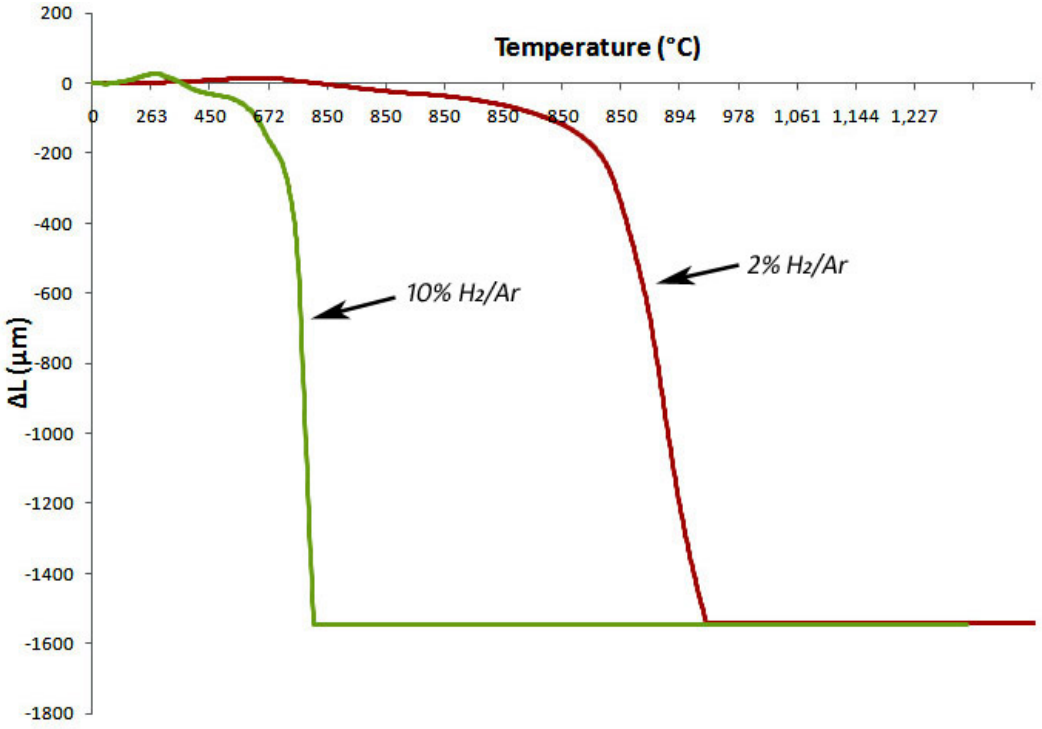

Figure 4.4: Shrinkage vs. Temperature of 4140 waffle extrusions in different atmospheres.

4.4 Microscopy of Reduced and Sintered Samples

Prior to gas carburization experiments, the microstructure of the reduced and sintered strip was evaluated in order to determine the heat treatment parameters necessary to reduce and sinter the extrusions. The following sections will detail microstructural observations, as well as results from EDS analysis on iron, 4140 and 316L tape prior to gas carburization.

4.4.1 Iron Strip

Figure 4.5 shows an optical micrograph of the cross-section of Fe_3O_4 strip after reduction following the heating schedule given in Table 3.2 (Section 3.1.1). The final thickness of the sample after heat treatment was approximately 180 μm. Ferrite grain boundaries are evident in the figure, due to a nital etch prior to inspection. Also, pores are evident through the cross-section. It is believed that the porosity is due to inadequate compaction of paste prior to the extrusion of these samples, as experiments in the reduction of iron oxide powder compacts have shown that densities up to 99.40% of the theoretical density can be achieved (see Section 4.2). The grain size of the sample was calculated using the mean intercept method, and the resulting ASTM grain size number was found to be between approximately 5.4 and 6.5 with 95% confidence.

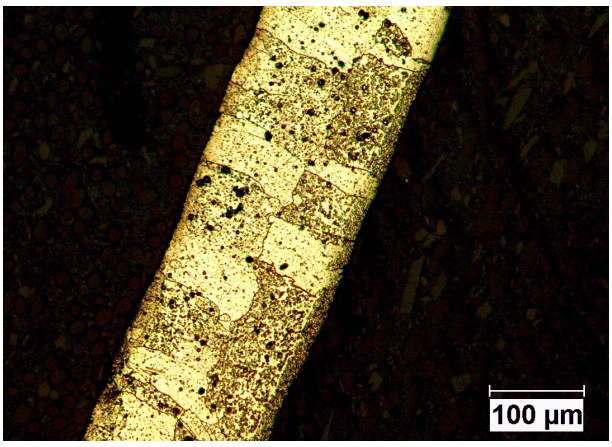

Figure 4.5: Optical micrograph of the cross-section of reduced and sintered Fe_3O_4 strip of approximately 180 μm thickness.

4.4.2 4140 Strip

Final thicknesses of reduced and sintered 4140 strip prior to carburization were approximately 240-250 μm. In the case of samples made using Batch 1 composition (using MnO_2 powder) as was detailed in Section 3.1.2, large amounts of unreduced MnO_2 were observed under even the longest heating schedule, thus only a few samples were carburized from this batch. Figure 4.6 shows an EDS map of the cross-section of 4140 strip made from Batch 2 (using Mn metal powder) reduced following heating schedule 'A' (240 min hold at 1250°C), as was given in Table 3.5. From the map, it is evident that reduction has not completed, as large amounts of oxygen and chromium are still seen through the cross-section. It is clear from the map that iron reduced first while Cr_2O_3 is still left unreduced. Figure 4.7 shows the SEM image and corresponding EDS map for a sample treated under heating schedule 'B' (30 min hold at 450°C, 480 min hold at 850°C and 240 min hold at °C). From the figure, it is shown that further reduction of Cr_2O_3 has occured, though it has not completed in the time allotted. Lastly, Figure 4.8 shows the SEM image and corresponding EDS map for a sample treated under heating schedule 'C' (slower heating rate than schedule B). Similar amounts of unreduced Cr_2O_3 are observed and microstructures look very similar.

Through the comparison of Figures 4.6, 4.7 and 4.8, it can be deduced that though chromium contents up to 25 wt% can be reduced (Section 2.1.2), very low contents cannot. This is the due to the fast reduction of Fe_3O_4 relative to that of Cr_2O_3. Because Fe_3O_4 reduces so quickly, it creates a barrier to the diffusion of oxygen in Cr_2O_3 to the surface of the green strip, thus Cr_2O_3 cannot fully reduce at such low contents. At higher Cr_2O_3 contents, the amount of chromia prohibits the iron from enclosing the Cr_2O_3 particles, such that diffusion of oxygen can still proceed fairly quickly. In alloys where low amounts of chromium are necessary, it may be possible to use chromium carbides rather than Cr_2O_3, as these are also reduceable by hydrogen.

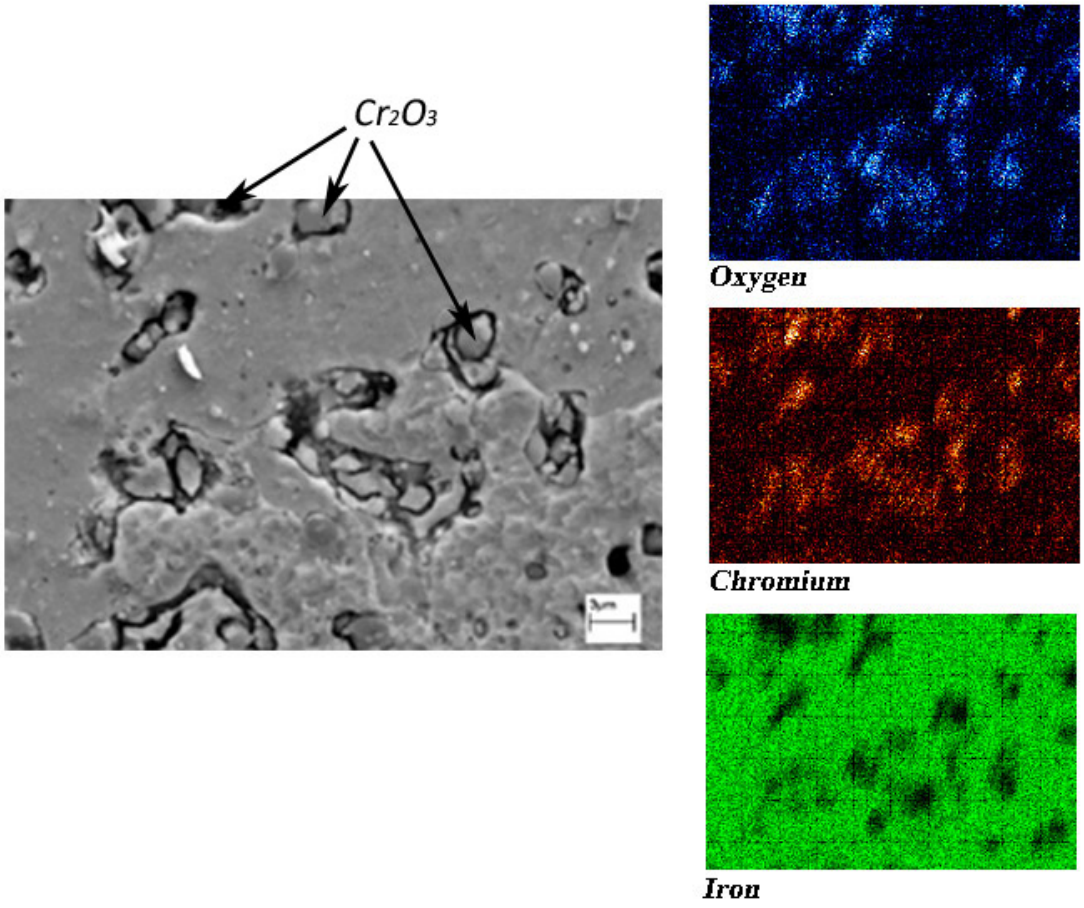

Figure 4.6: EDS mapping of 4140 strip reduced following heating schedule A (240 min hold at 1250°C).

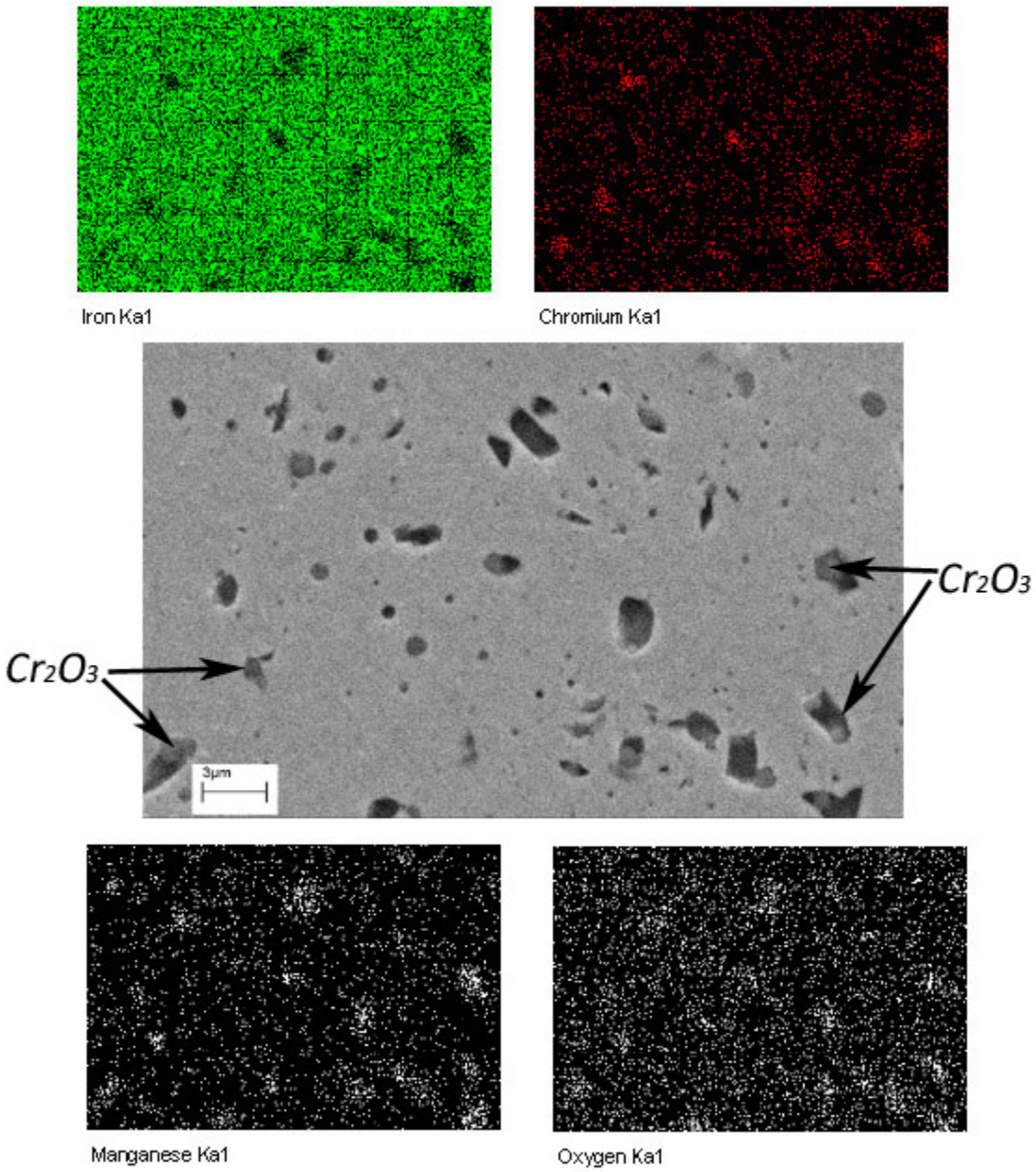

Figure 4.7: EDS mapping of 4140 strip reduced following heating schedule B (30 min hold at 450°C, 480 min hold at 850°C and 240 min hold at 1300°C).

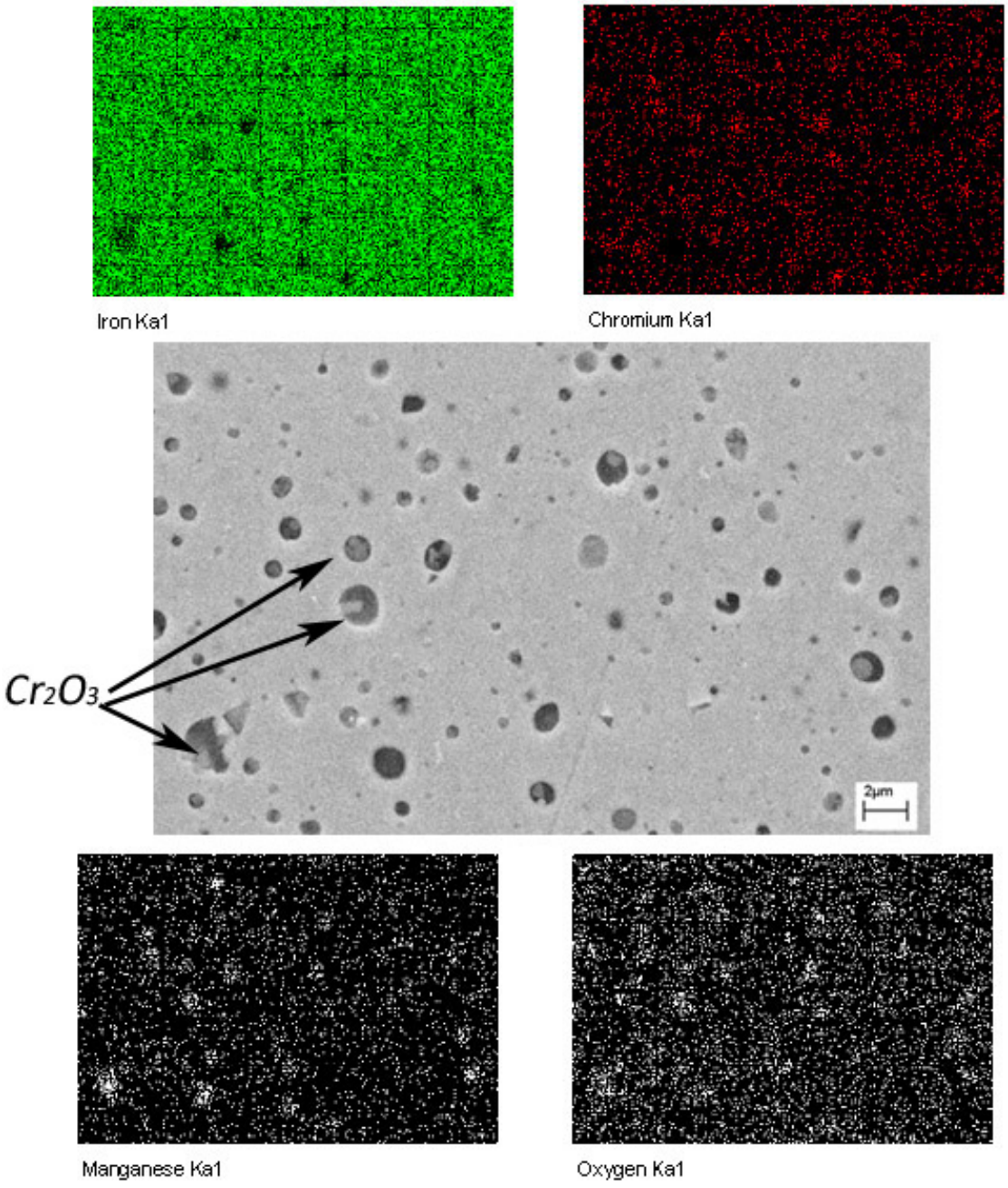

Figure 4.8: EDS mapping of 4140 strip reduced following heating schedule C (same as schedule B, with a slower heating rate).

4.4.3 316 Strip

Figure 4.9 shows an SEM micrograph and corresponding EDS maps for chromium, iron and oxygen for a sample of 316 tape heat-treated following schedule 'a' (10% H_2/Ar atmosphere), as was shown in Table 3.7 (Section 3.1.3). From the figure, it is evident that chromium has not fully reduced, while iron has completed reduction. A second sample heated in 10% H_2/Ar, under schedule 'b' is shown in Figure 4.10, and it is evident from the figure that the sample also has not fully reduced. Consequently, experiments moved to the use of pure H_2, as it can be concluded that a 10% H_2/Ar atmosphere is not sufficent to reduce 316 strip in a reasonable amount of time.

Samples of unreduced 316 strip treated following heating schedules 'c' through 'e' in Table 3.7 (2 hour soak to 30 hour soak at 1350°C, 100% H_2) all showed signs of unreduced Cr_2O_3, though the volume of unreduced Cr_2O_3 in the samples decreased with soak time, as expected. Figure 4.11 shows an SEM image and corresponding EDS mapping of a sample treated under heating schedule 'e' (12 hour soak), showing unreduced Cr_2O_3 particles.

Figures 4.12, 4.13 and 4.14 show relatively low magnification images of the cross-sections of samples soaked in 100% H_2 for 2, 30 and 40 hours, respectively. It is evident in comparison of the three figures that full reduction has only occurred after 40 hours of soaking at 1350°C. Figure 4.15 shows the center of the cross-section of a sample heated following schedule 'h' (40 hr soak) at a higher magnification, showing that pores are evident in the sample, but there is no evidence of Cr_2O_3 particles. Once fully reduced and sintered, 316 tape resulted in a final thickness of approximately 270-280 μm, and a weight loss of approximately 31%. It is evident in the micrographs that porosity is present through the samples, which is likely due to the sluggish reduction of Cr_2O_3 particles.

Image J software, developed by the National Institutes of Health, was used to analyze the area fraction of pores in samples that were fully reduced. A montage of the cross-section of the samples, like what is shown in Figure 4.15, was used for the measurements. The sample heated follow schedule 'i' (50 hour soak) showed a lower amount of porosity

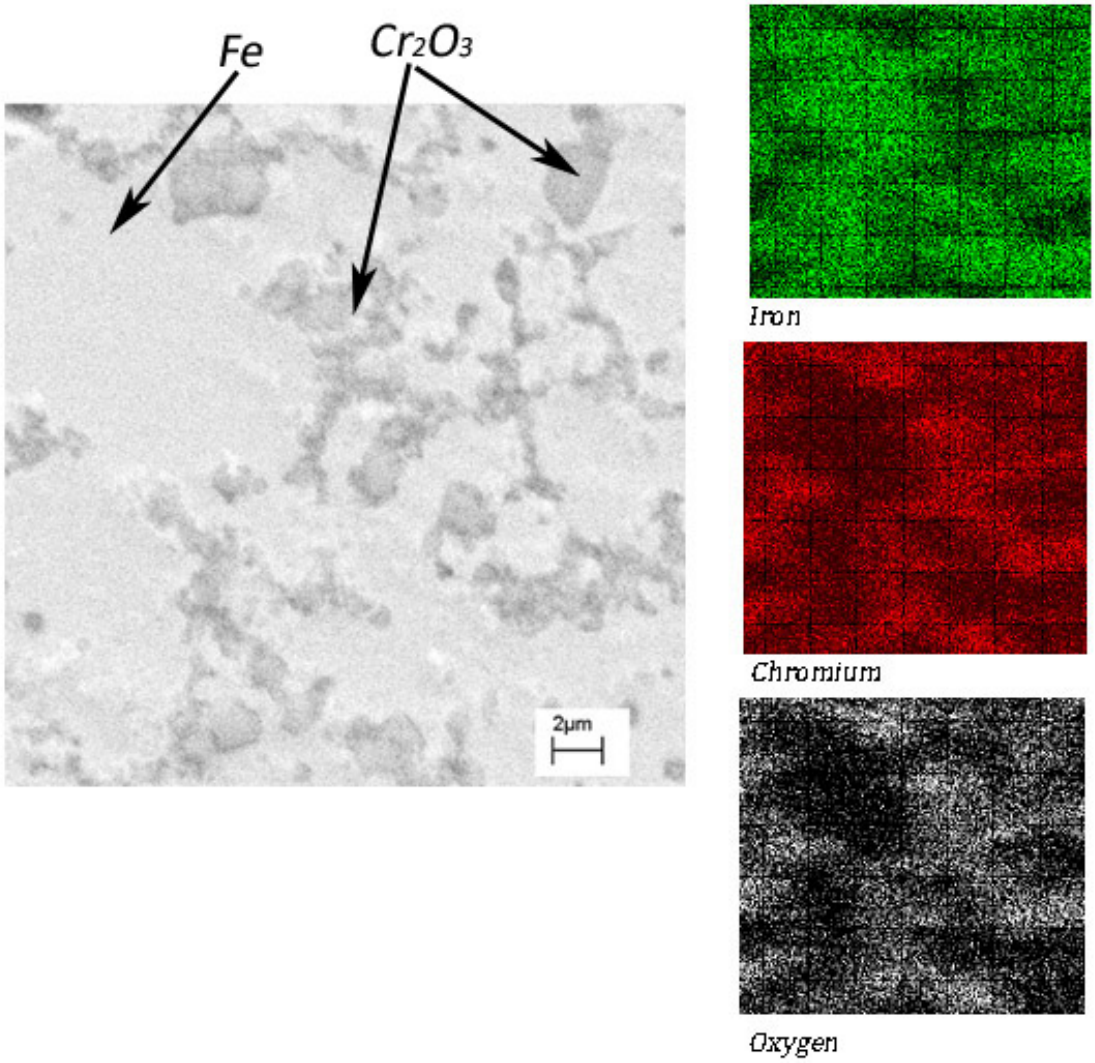

Figure 4.9: EDS mapping of 316 strip reduced following heating schedule 'a' (10% H_2/Ar atmosphere).

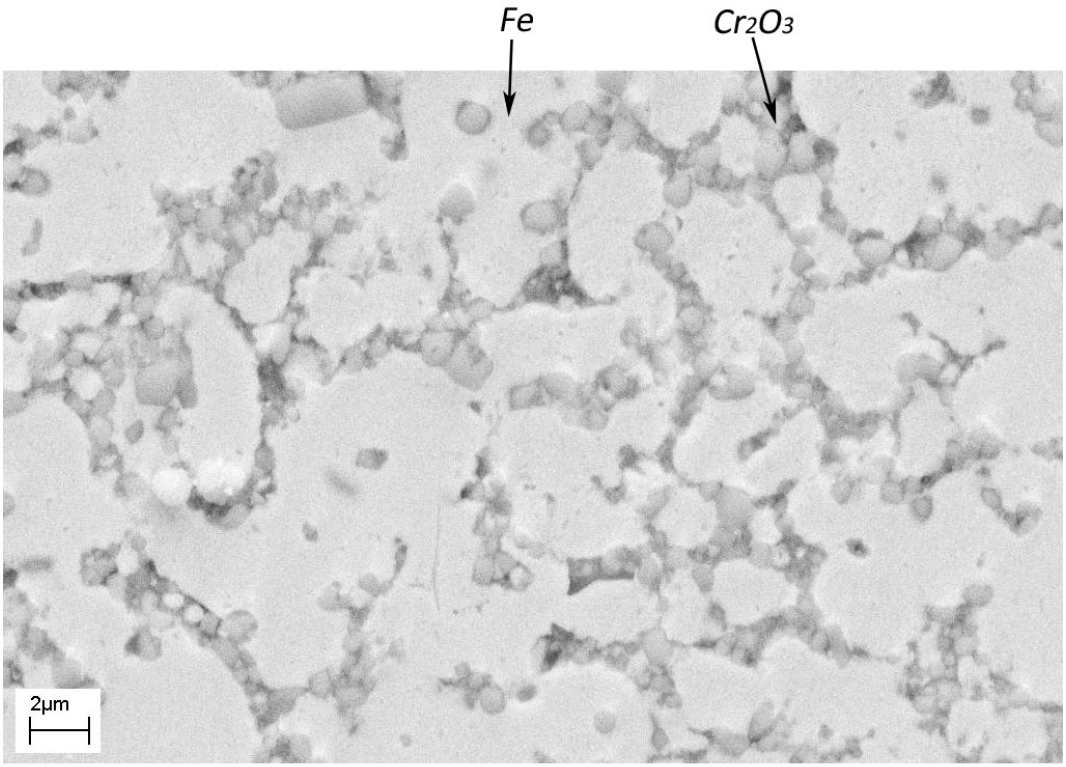

Figure 4.10: SEM micrograph of 316 strip reduced following heating schedule 'b' (10% H_2/Ar atmosphere).

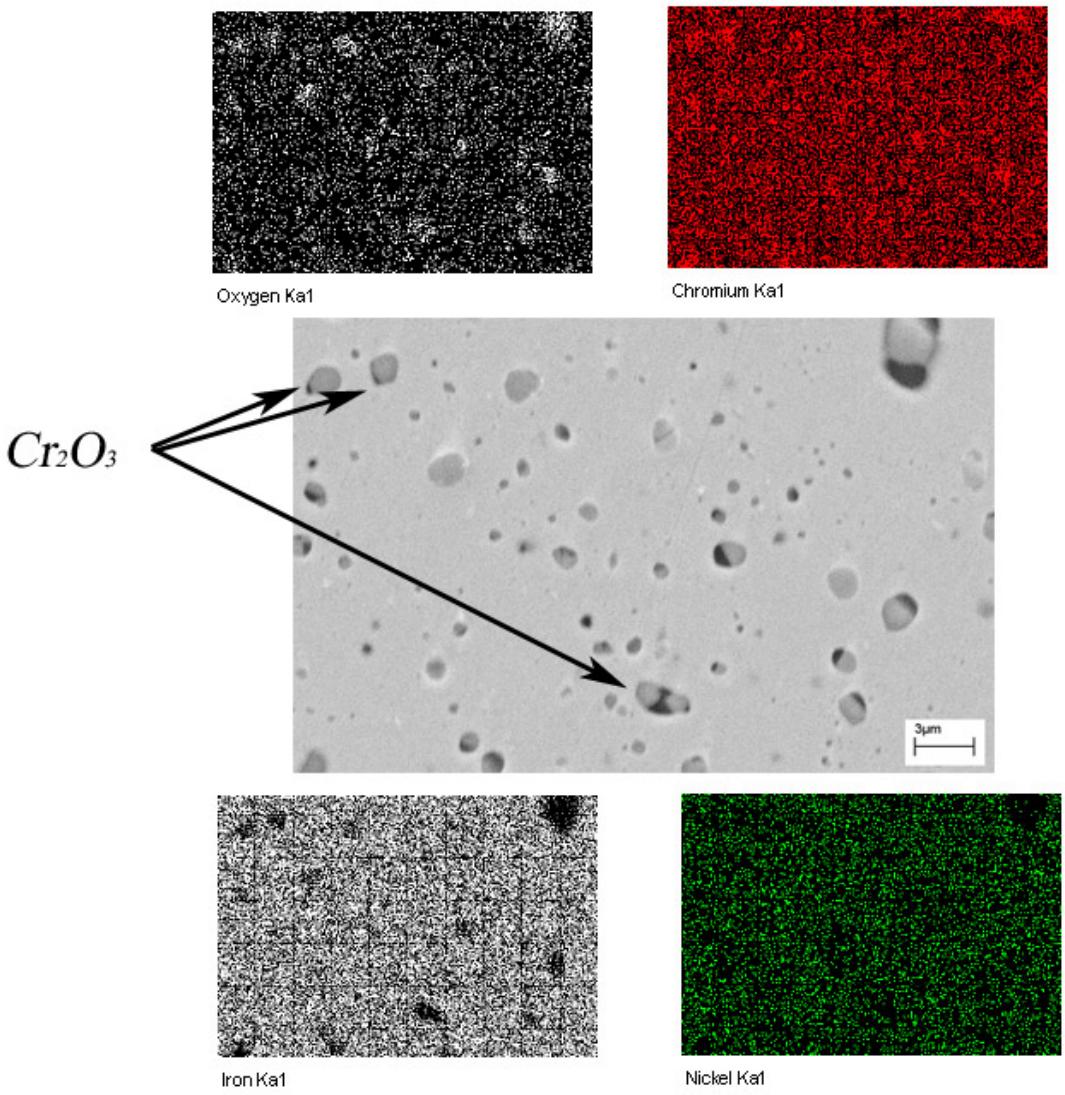

Figure 4.11: SEM micrograph and corresponding EDS map of 316 strip reduced following heating schedule 'e' (12 hr soak, 100% H_2). Several unreduced Cr_2O_3 particles are labelled in the image.

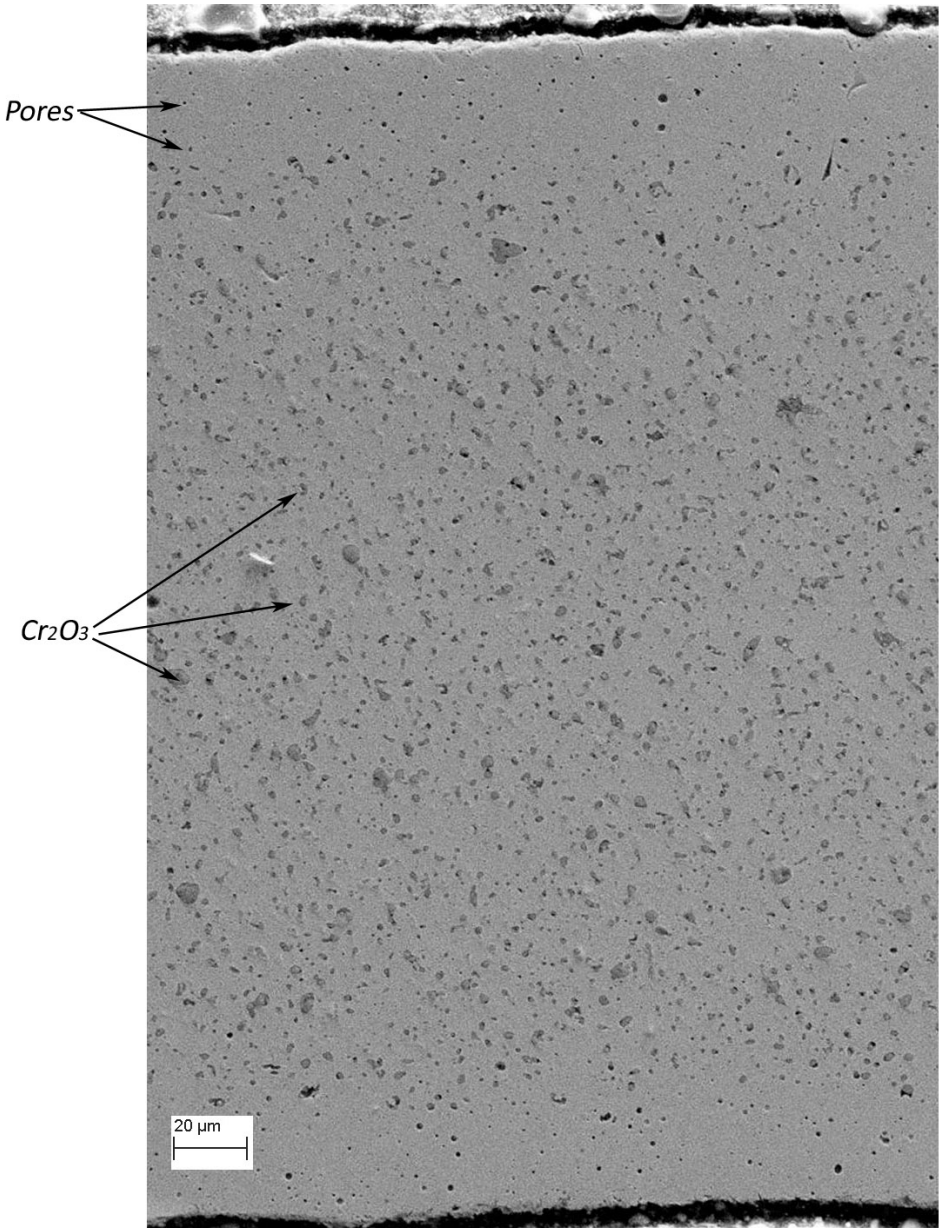

Figure 4.12: SEM micrograph of 316 strip reduced following heating schedule 'c' (2 hour soak, 100% H_2). Cr_2O_3 particles have fully reduced to depths of approximately 40 μm from the surface.

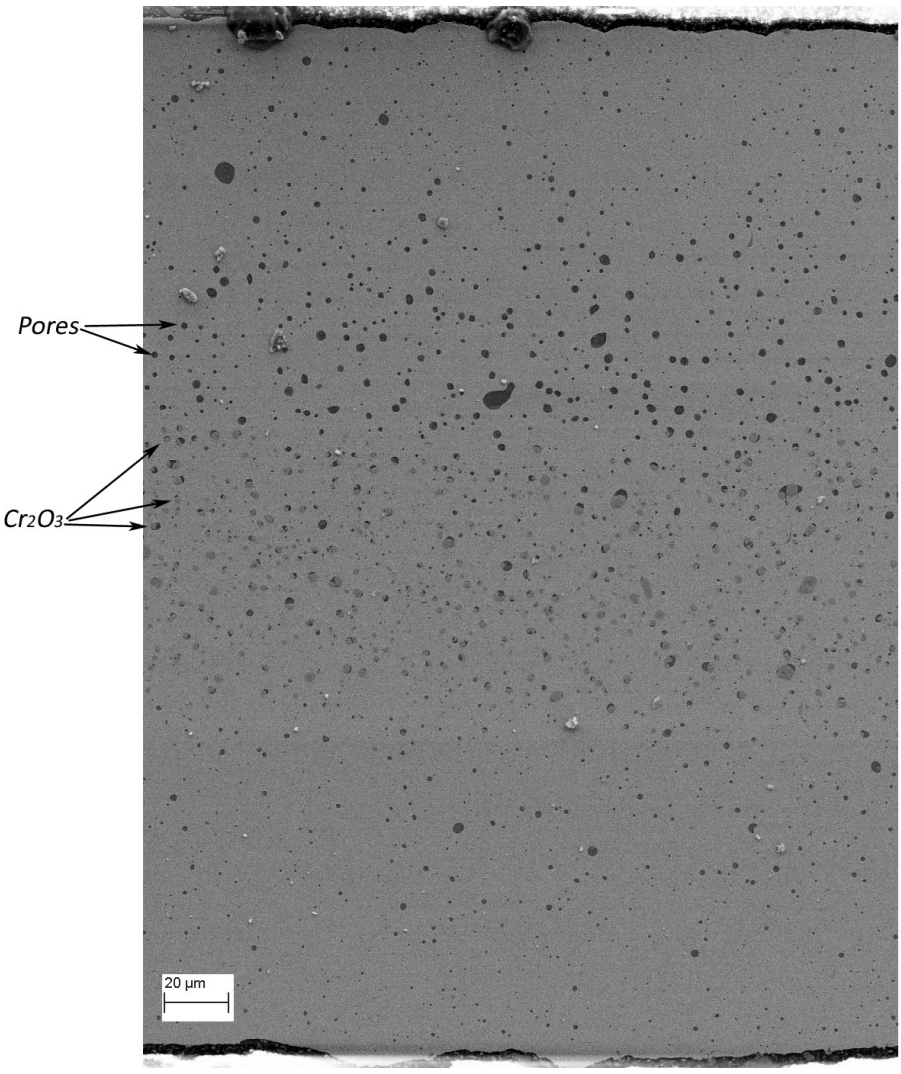

Figure 4.13: SEM micrograph of 316 strip reduced following heating schedule 'g'(30 hour soak, 100% H_2). Cr_2O_3 particles have fully reduced to depths of approximately 100 μm from the surface.

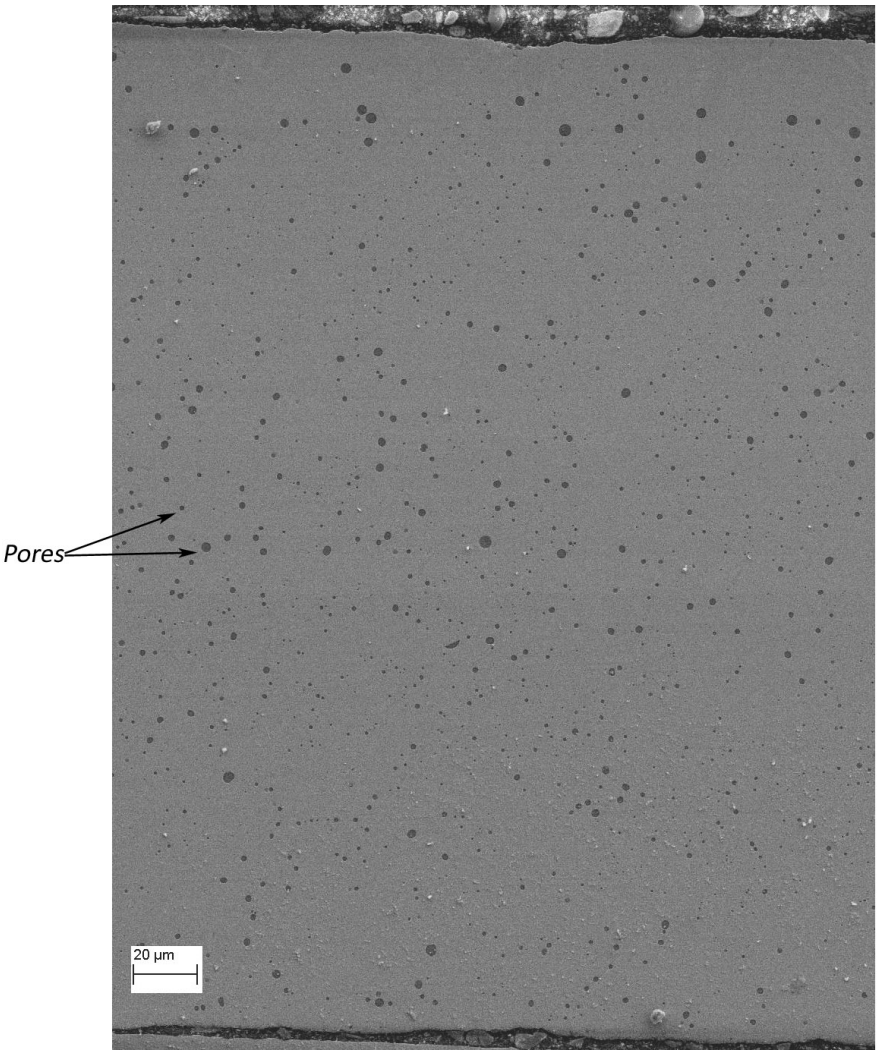

Figure 4.14: SEM micrograph of 316 strip reduced following heating schedule 'h' (40 hour soak, 100% H_2). All Cr_2O_3 particles have been fully reduced.

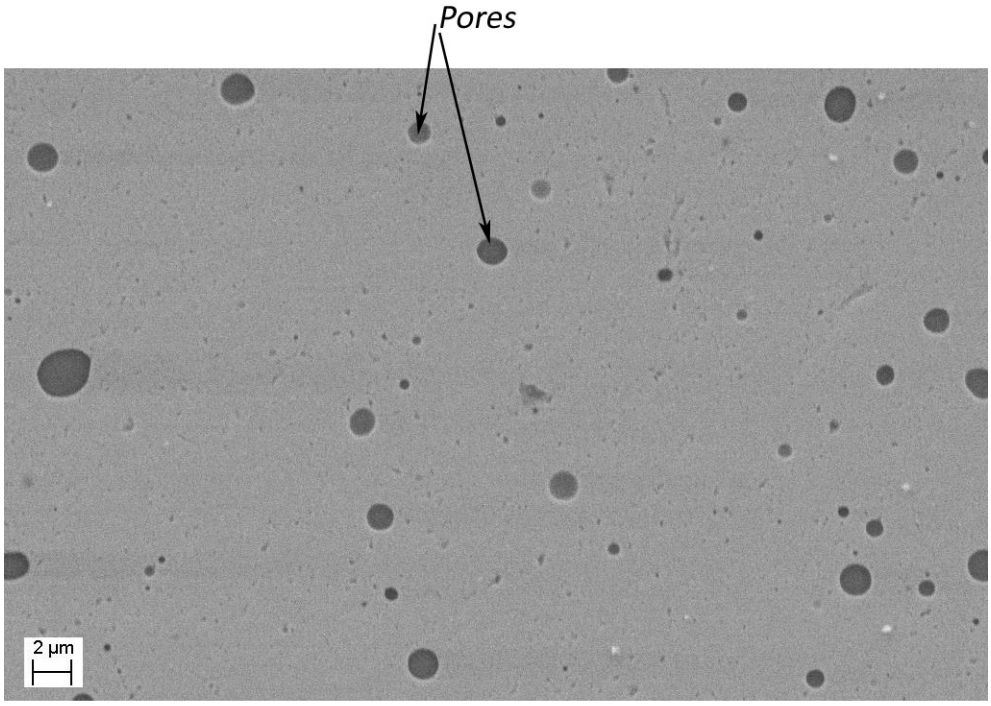

Figure 4.15: High magnification SEM micrograph of the center of the cross-section of a 316 strip reduced following heating schedule 'h' (40 hour soak, 100% H_2), showing that Cr_2O_3 particles are not present.

than the sample soaked for 40 hours (heating schedule 'h'), as a result of extended time for sintering to occur. More specifically, the volume percent of pores greater than 1 μm in diameter for the samples soaked for 40 and 50 hours were 1.3% and 0.5%, respectively.

4.5 Gas Carburization

4.5.1 Gas Carburization of Iron Strip

A plot of the TGA data taken during a gas carburization experiment of iron strip with C_s = 1.0 wt% C is shown in Figure 4.16. The blue line denotes the time period at which the sample is being heating in a 4% H_2/Ar atmosphere and the pink line denotes the time at which a carburizing atmosphere is present in the furnace chamber. It is evident during the carburization time period that the weight of the sample is increasing. The green line denotes the time period at which the furnace was cooling. It is important to note that TGA

data was not taken once the weight of the sample remained steady during cooling. It is also important to note that a sudden change of weight upon the introduction of different gaseous atmospheres is due to the changing flow within the furnace chamber, and gradual weight increase during heating is due to buoyancy changes of the gas upon heating.

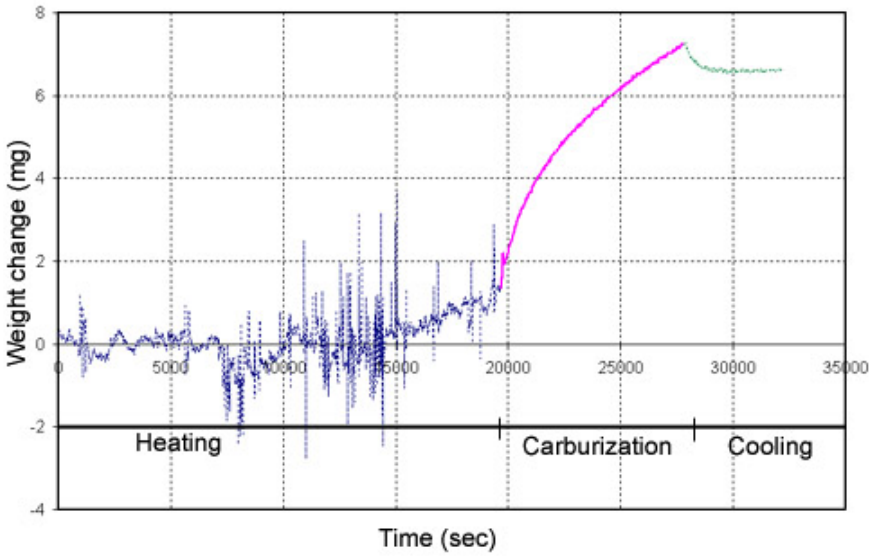

Figure 4.16: TGA plot of weight gain versus time for the carburization of an approximately 200μm thick sample of iron strip. The pink line denotes the time at which a carburizing atmosphere is in the furnace where appreciable weight gain is noted.

Figure 4.17 shows an optical micrograph of the cross-section of the tip of the carburized sample. The micrograph shows a decarburized layer around the outside of the sample, likely forming during cooling of the sample. Figure 4.18 shows a higher magnification image of an area of the same sample, such that the pearlite colonies and the decarburized layer are more easily seen. Microscopic investigation also did not show any signs of oxidation of the sample. Additionally, evidence of metal dusting of the sample was not observed.

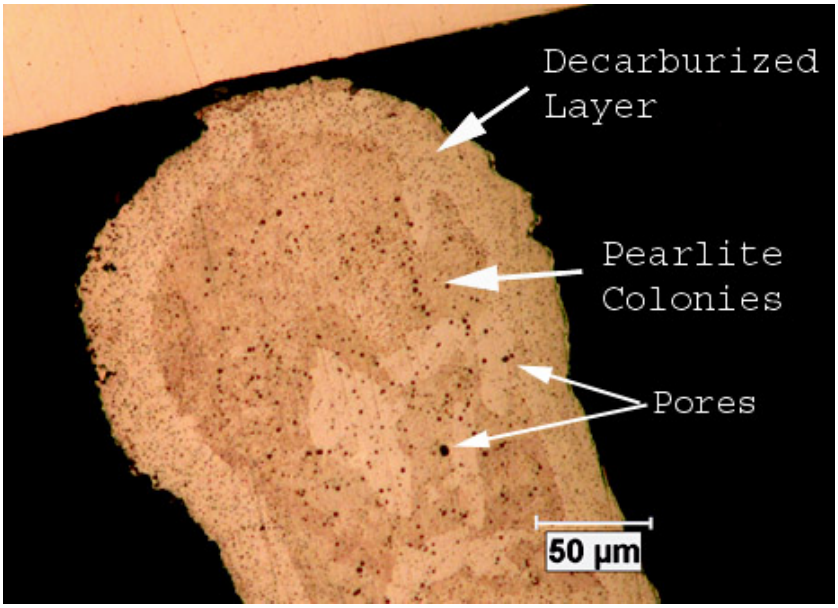

Figure 4.17: Optical micrograph of fully reduced Fe_3O_4 carburized for 2 hours and 15 minutes, in which pearlite colonies, pores, and a decarburized surface layer are evident.

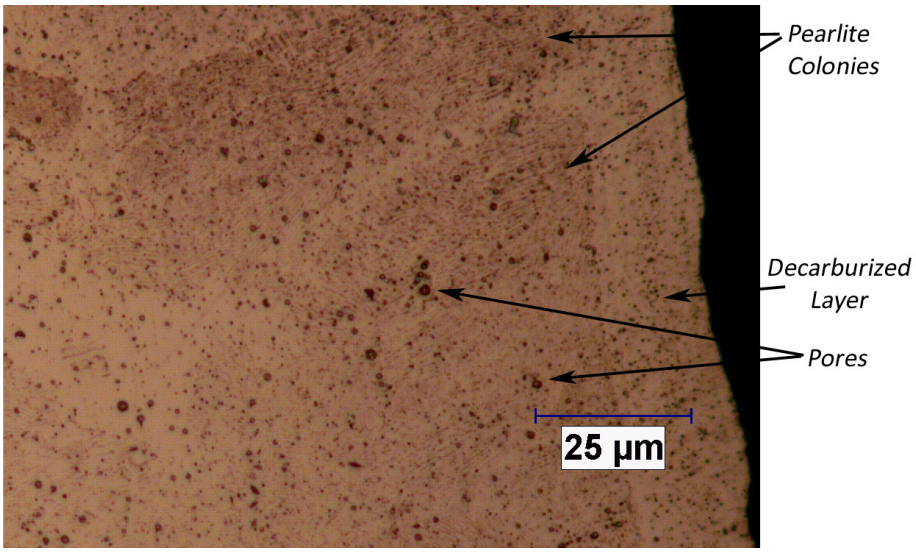

Figure 4.18: Optical micrograph of the edge of a fully reduced Fe_3O_4 strip carburized for 2 hours and 15 minutes. Pearlite colonies, pores, and a decarburized surface layer are evident in the micrograph.

The volume fraction of pearlite colonies was measured using point counting to be 0.64 ± 0.09. The large error in the calculation is due to the inclusion of the decarburized layer in the volume fraction calculation. The decarburized layer, which was measured to be of the order of 10-20 μm thick, is due to the fact that a decarburizing atmosphere (4% H_2/Ar) was present upon cooling of the sample. In addition to the formation of a decarburized layer, decarburization can also occur into the center of the sample, especially along fast diffusion paths, such as grain boundaries.

Additional measurement of the volume fraction of pearlite colonies without the consideration of the decarburized layer yielded a smaller error and higher volume fraction of pearlite: 0.82 ± 0.05. This suggests that if samples are quenched, rather than cooled slowly, a volume fraction of around 85% pearlite can be achieved in 2 hours and 15 minutes in the carburizing atmosphere that was detailed in the experimental methods. The lever rule along with an Fe-C phase diagram (Figure 2.19, Section 2.5.1), can be used to determine the carbon content in the sample. Equation 35 shows the lever rule as it was used for this problem.

$$V_f^{Pearlite} = \frac{X_{carb} - X_\alpha}{X_{eut} - X_\alpha} \tag{35}$$

where $V_f^{Pearlite}$ is the volume fraction of pearlite in the sample, X_α is the solid solubility of carbon in ferrite at the eutectoid temperature (0.025 wt% C), X_{eut} is the eutectoid carbon composition (0.76 wt% C) and X_{carb} is the composition of the alloy.

From this information, it was determined that a volume fraction of 0.85 pearlite suggests that during the carburizing experiment, a carbon content of at least 0.65 wt% carbon was achieved prior to the cooling and subsequent decarburization of the sample. It is important to point out that it is reasonable to believe that the eutectoid composition was reached in this sample prior to cooling, as was the goal of this individual experiment. For example, assuming the part reached a composition of 0.8 wt% C during carburization and was then cooled in 4% H_2/Ar, the erf solution to Ficks second law (Equation 8) predicts that the carbon content in the center would drop to approximately 0.5 wt%, a composition below

the eutectoid, by the time was sample was cooled from 1000°C to 700°C. Because decarburization upon cooling has the potential to greatly affect the final carbon composition of the part, decarburization studies were performed and results are discussed in Section 4.9.

4.5.2 Gas Carburization of Strip with 4140 Composition

4.5.2.1 Carburization with C_s = 1.0 wt% C

All samples carburized with C_s = 1.0 wt% C for 65 minutes showed areas of proeutectoid cementite and pearlite, as well as a decarburized layer of ferrite; evidence that compositions above the eutectoid were reached. Thus, carburization times were lowered to 30 minutes in order to determine if the erf solution was not an accurate prediction of carburization of the 4140 thin tape samples that were used in this study. Recall, the erf solution predicted that 65 minutes were necessary to reach eutectoid compositions in pure iron of the same thickness.

Figure 4.19 shows an SEM image from which EDS spectra were taken for a sample held at C_s = 1.0 wt% C and carburized for 30 minutes. Figures 4.20 - 4.22 depict the area from which the data was taken along with the corresponding EDS spectra. The figures show that the structures are mostly pearlitic with areas of pro-eutectoid cementite. EDS spectra confirm the presence of pro-eutectoid cementite (Figure 4.20), pearlite (Figure 4.21) and a surface layer of ferrite (Figure 4.22) due to decarburization upon cooling. It is important to note that in Figures 4.20 - 4.22, the quantitative results (part b in each figure) are not exact due to the limitations of EDS but can be used as a rough estimate of the composition. The significant differences of carbon composition in ferrite, pearlite, and cementite allow the confirmation of the presence of these phases using the quantitative data.

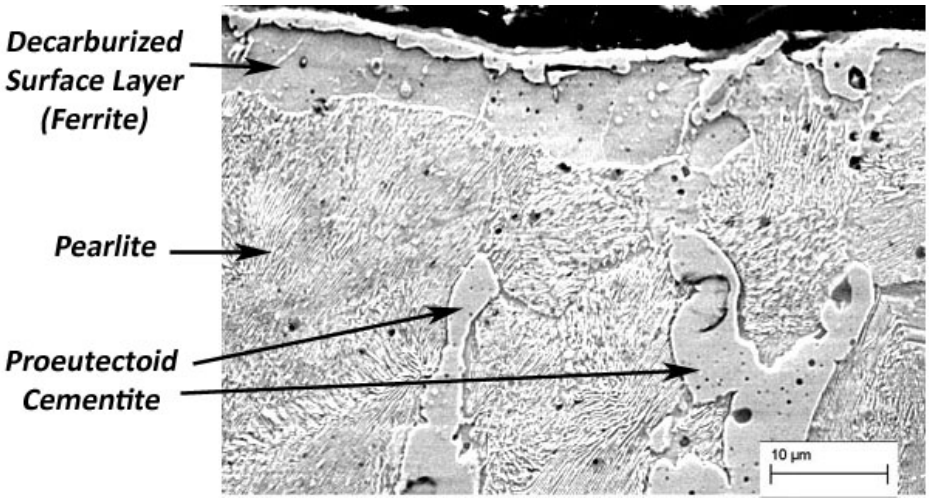

Figure 4.19: SEM image of the edge of the cross-section of a 4140 sample carburized with C_s = 1.0 wt% C for 30 minutes.

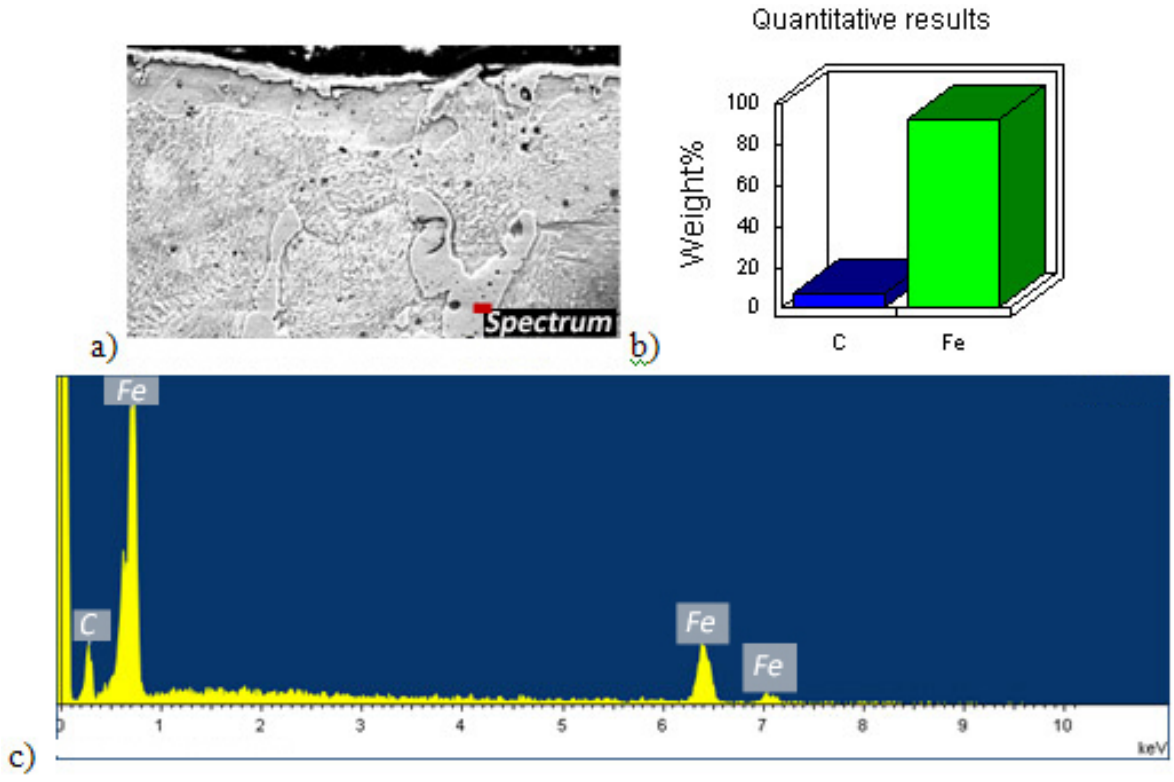

Figure 4.20: a) SEM image of the cross-section of 4140 strip carburized at C_s = 1.0 wt% C for 30 minutes denoting the area from which the spectra was taken (region of cementite). The results for carbon composition are shown in (b) while the spectrum is shown in (c).

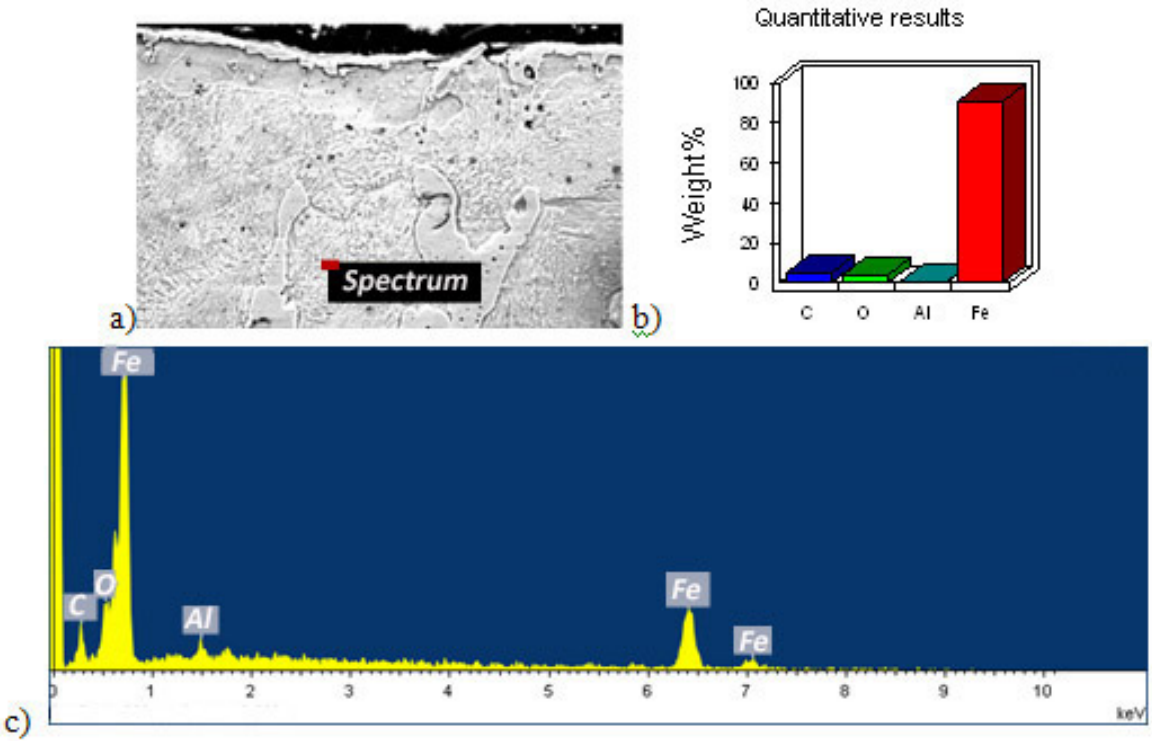

Figure 4.21: a) SEM image of the cross-section of 4140 strip carburized at C_s = 1.0 wt% C for 30 minutes denoting the area from which the spectra was taken (region of pearlite). The results for carbon composition are shown in (b) while the spectrum is shown in (c). The presence of oxygen and aluminum in (b) and (c) is resultant of the polishing media used.

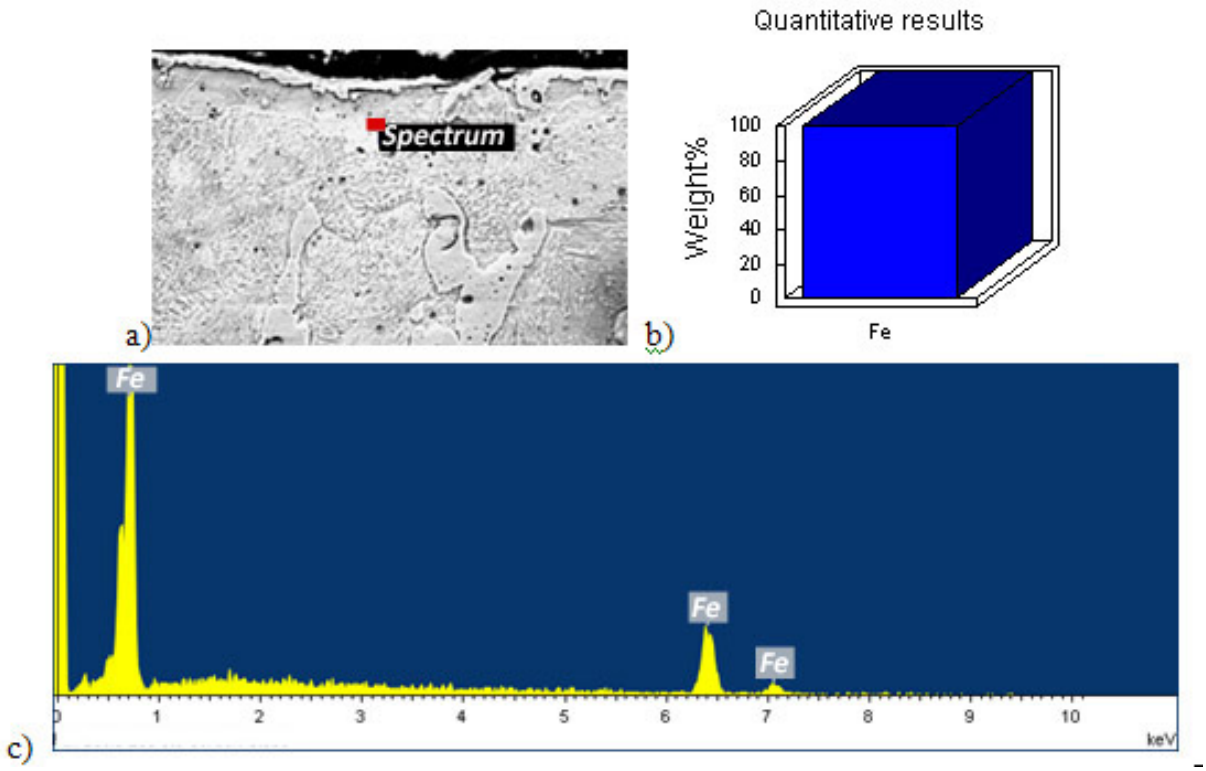

Figure 4.22: a) SEM image of the cross-section of 4140 strip carburized at C_s = 1.0 wt% C for 30 minutes denoting the area from which the spectra was taken (region of ferrite). The results for carbon composition are shown in (b) while the spectrum is shown in (c).

From the microstructures, it can be determined that the eutectoid composition can be reached in as little as 30 minutes using the carburization parameters as were detailed in Section 3.5.3.1. One possible reason for the ability for such compositions to be reached more quickly than predicted by the erf solution to Fick's second law is due to the Cr and Mo additions that are present in 4140 steel. As was presented in Section 2.2.1, while carbide forming elements reduce the diffusivity of carbon in iron, they ultimately increase carburization rates as they increase the mass transfer of carbon onto the surface of the part.

The resulting carbon contents for all samples carburized at C_s = 1.0 wt% C were determined through point counting volume fraction measurements of pearlite colonies, coupled with the lever rule. Equation 36 shows the lever rule as it is used to determine the volume fraction of pearlite when the composition lies above the eutectoid carbon content. The resulting carbon contents are shown in Table 4.3. This information is also presented graphically in Figure 4.23.

$$V_f^{Pearlite} = \frac{X_{Fe_3C} - X_{carb}}{X_{Fe_3C} - X_{eut}} \tag{36}$$

where $V_f^{Pearlite}$ is the volume fraction of pearlite in the sample, X_{Fe_3C} is the composition of iron carbide (6.7 wt% C), X_{eut} is the eutectoid carbon composition (0.76 wt% C) and X_{carb} is the composition of the alloy.

Table 4.3: Carbon contents measured in 4140 samples carburized with C_s = 1.0 wt% C.

Sample Name	Time (min)	Flow rate (mL/min)	Carbon Content (wt%)
4140_carb_4	65	400	1.5 ± 0.2
4140_carb_5	30	400	1.1 ± 0.3
4140_carb_9	30	400	3.6 ± 0.6
4140_carb_17	30	400	3.1 ± 0.6
4140_carb_18	30	800	1.1 ± 0.2
4140_carb_20	30	800	1.2 ± 0.3
4140_carb_21	30	800	1.2 ± 0.2
4140_carb_22	65	800	1.6 ± 0.4

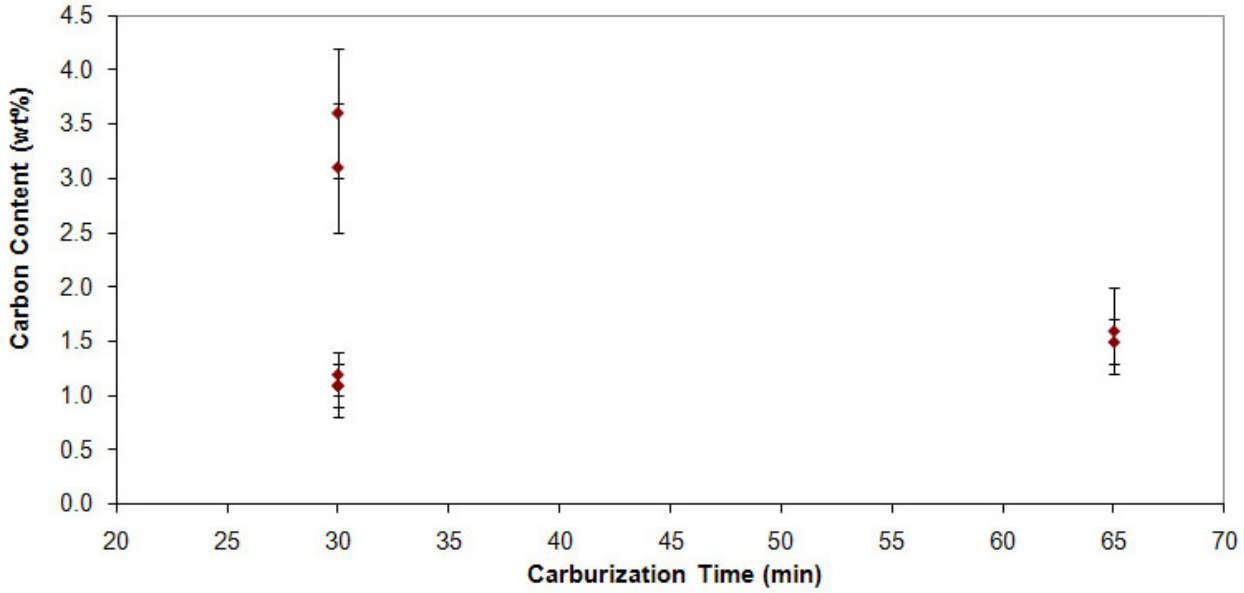

Figure 4.23: Final carbon contents achieved in 4140 samples treated at C_s = 1.0 wt% C as determined through point counting measurements.

Due to the low flow of CO_2 necessary in order to achieve atmospheres corresponding to C_s = 1.0 wt% C, slight changes in the flow of CO_2, and thus composition of the atmosphere, can significantly increase the equilibrium surface concentration of carbon during the experiment, resulting in higher carbon contents than expected (as was shown in Figure 3.6). Thus, large deviations from the desired carbon content for samples treated at lower flow rates (400 mL/min) can be attributed to the accuracy of the mass flow controllers used in the experiments. By increasing the flow rate into the tube furnace when relatively small percentages of CO_2 are necessary, the error associated with the mass flow controllers is lowered.

4.5.2.2 Carburization with C_s = 0.4 wt% C

Figure 4.24 shows an SEM micrograph of the cross-section of a sample carburized with C_s = 0.40 wt% C for 45 minutes. Pores are evident in the micrograph as well as areas of pearlite and ferrite. A decarburized layer is present along the surface of the sample, as well as unreduced Cr_2O_3 and MnO_2 through the cross-section. It is important to note that this sample was made using Batch 1 in Section 3.1.2 (using MnO_2 powder). Samples made with Mn metal powder only showed small amounts of unreduced Cr_2O_3. Table 4.4 shows the resulting carbon contents as determined through point counting for samples carburized with C_s = 0.4 wt% C. This information is also plotted graphically in Figure 4.25.

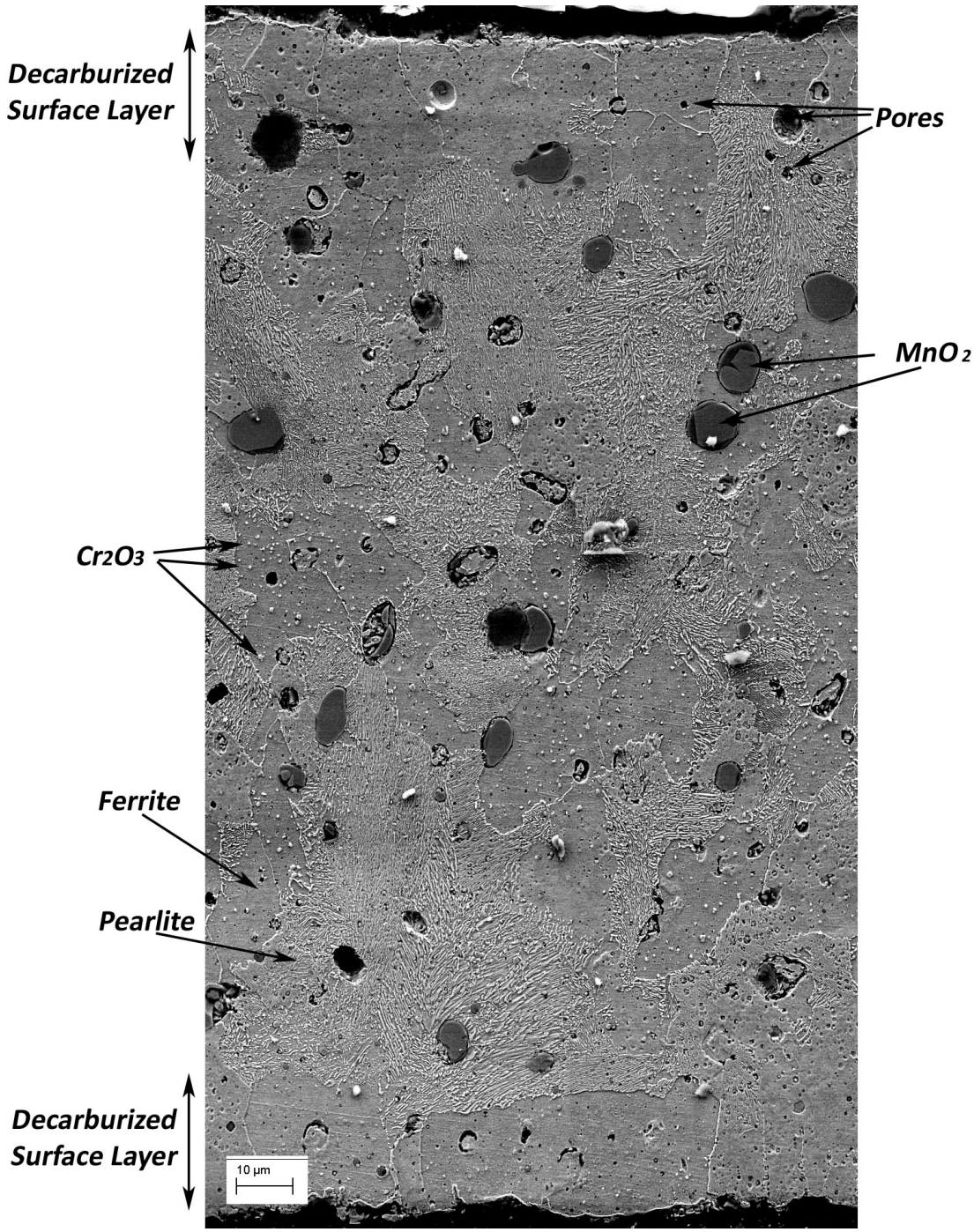

Figure 4.24: SEM montage of the cross-section of a 4140 sample (4140_carb_16) carburized with C_s = 0.40 wt% C for 45 minutes

Table 4.4: Carbon contents measured in 4140 samples carburized with C_s = 0.4 wt% C.

Sample Name	Time (min)	Flow rate (mL/min)	Carbon Content (wt%)
4140_carb_15	30	400	0.32 ± 0.06
4140_carb_16	45	400	0.52 ± 0.05
4140_2_carb_31	15	800	0.33 ± 0.05
4140_carb_23	30	800	0.52 ± 0.07
4140_2_carb_26	30	800	0.64 ± 0.06
4140_2_carb_27	30	800	0.65 ± 0.05
4140_2_carb_28	30	800	0.72 ± 0.02
4140_carb_24	45	800	0.36 ± 0.08
4140_2_carb_3	60	800	0.40 ± 0.04
4140_2_carb_25	60	800	0.70 ± 0.03
4140_2_carb_29	60	800	0.76 ± 0.00
4140_2_carb_30	60	800	0.60 ± 0.05

It can be seen in Table 4.4 that errors up to 0.07 wt% are seen in the final carbon content, which is likely due to the accuracy of using point counting as an estimate for the carbon content in the samples. What is important to observe in Figure 4.25 is that at carburization times of 30 minutes and greater, the calculated compositions are all very similar. While one sample carburized for 15 minutes did result in a calculated composition near those that were treated for longer times, others only showed very shallow layers of pearlite on one surface of the strip. Thus it is believed that at 15 minutes of carburization, the sample has not had the time to reach the composition of interest with repeatability.

Like the carburization of 4140 with C_s = 1.0 wt% C, carburization times significantly lower than what is estimated through the erf solution to Ficks second law are observed. In this case, in order to reach a carbon composition of 0.35 wt% C in the center of a 200μm thick sample, approximately 150 minutes in the carburizing atmosphere is predicted. As was stated previously, Cr and Mo additions should increase the carbon transfer to the surface of the part, thus increasing carburization. Due to the thin nature of the samples, as well as the relatively fast diffusion of carbon at high temperatures, the erf solution to Ficks second law does not give a reasonable estimate to the carburization time necessary for the conditions of interest to this study.

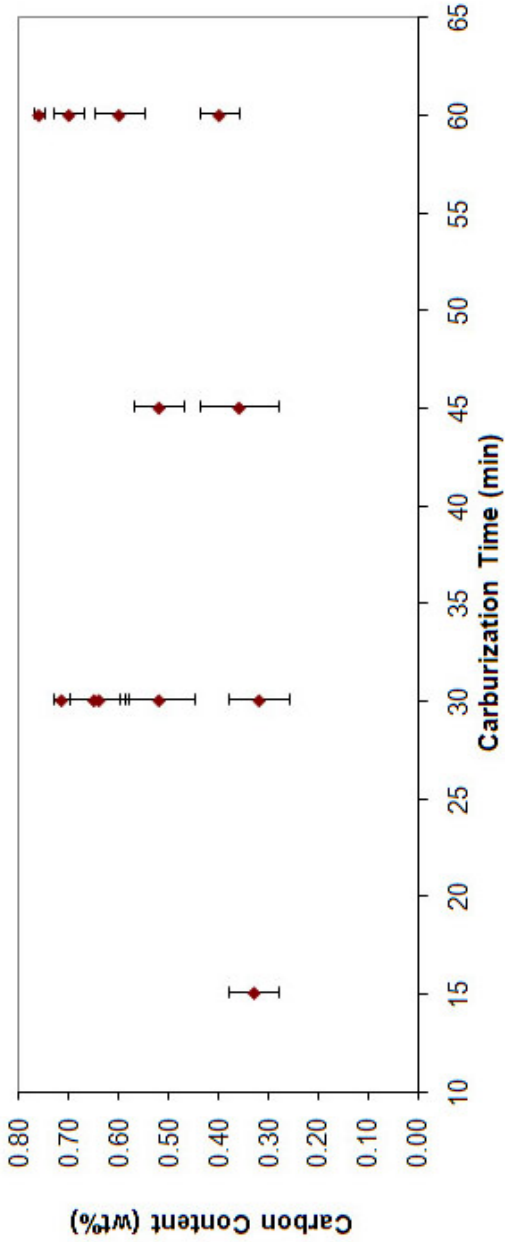

Figure 4.25: Final carbon contents of 4140 samples carburized with C_s = 0.40 wt% C at 1000°C, as determined through point counting

When comparing Figures 4.23 and 4.25, larger errors in point counting results for samples treated with C_s = 1.0 wt% C (Figure 4.23) are due to the high sensitivity of the carbon content as related to the volume fraction of pearlite at compositions above the eutectoid. Point counting measurement errors remained very similar to those measurements for samples carburized with C_s = 0.4 wt% C, but this translates to a larger error in the carbon content when using the lever rule above the eutectoid composition than when using it for carbon contents below the eutectoid composition.

4.5.3 Gas Carburization of Hollow Spheres with 4140 Composition

Figure 4.26 shows SEM images of the cross-sections of spheres carburized with 97% CO for 60 minutes. From Figure 4.26 a), it can be seen that at low magnification, the spheres are fairly uniform, though some variations in wall thickness can be seen. However, at higher magnifications, as shown in Figure 4.26 b), the large amounts of porosity in the sphere wall are clearly seen, demonstrating the need for a better coating technique for the fabrication of the spheres prior to carburization. Also in Figure 4.26 b), a pearlitic microstructure is not visible.

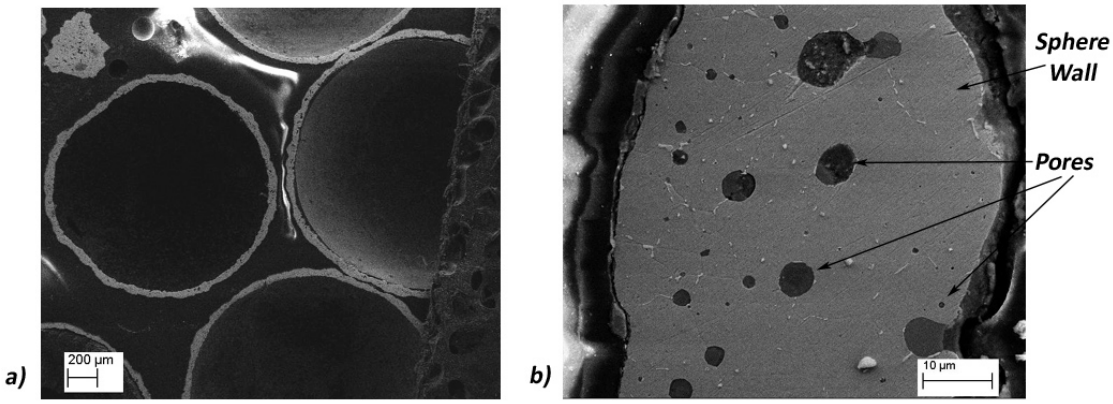

Figure 4.26: SEM images of the cross-sections of 4140 spheres carburized for 60 minutes in a 97% CO atmosphere at a) low magnification and b) higher magnification. In b) large pores are evident through the cross-section of the sphere wall.

Figure 4.27 shows a higher magnification image of a sphere wall. In the figure, areas of proeuctoid cementite are evident along the grain boundaries in the sample. Carburization experiments on 4140 strip showed decarburized surface layers on the order of 10-20 μm (see Figure 4.24, Section 4.5.2.2). However, due to the higher degree of porosity of the sphere wall, it is reasonable to believe that decarburization upon cooling has reached through the sphere wall and subsequently left only small areas of proeutectoid cementite visible in the microstructure.

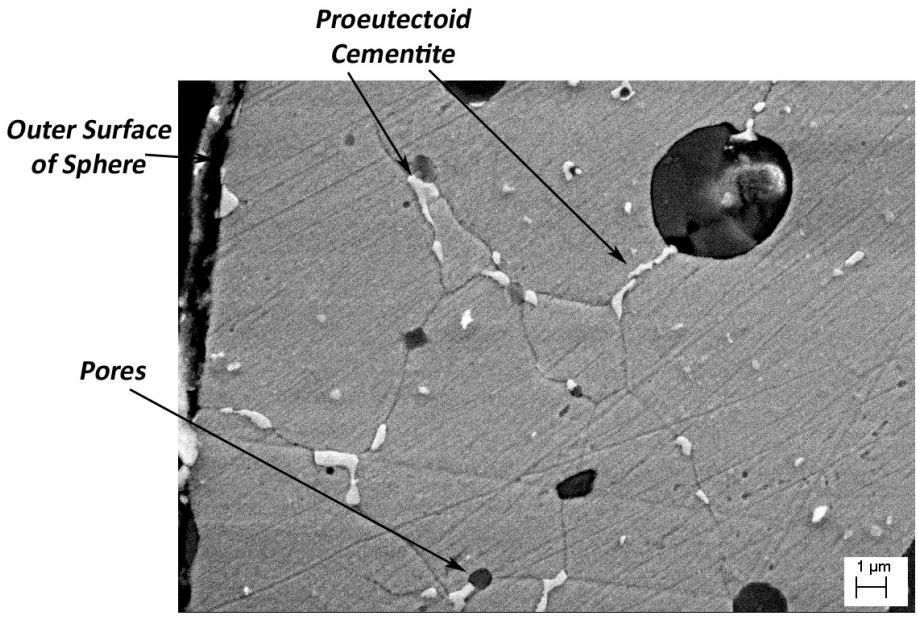

Figure 4.27: SEM image of the cross-section of a 4140 sphere carburized for 60 minutes in a 97% CO atmosphere. Areas of proeutectoid cementite are evident along the grain boundaries.

4.5.4 Gas Carburization of Strip with 316 Composition

Because 316 steel has an austenitic microstructure and the carburization process was chosen such that carbides did not form, microstructural evaluation cannot be used to estimate the carbon content of the samples. Figure 4.28 shows an optical micrograph of the cross-section of a 316 sample carburized for 25 hours. A metal soot was observed on both of

the carburized samples upon removal from the furnace, and areas where metal dusting was most severe is shown in the figure. As a result, if this technology is to be used for thin-walled structures, it is important to compensate for any material loss that will occur during carburization.

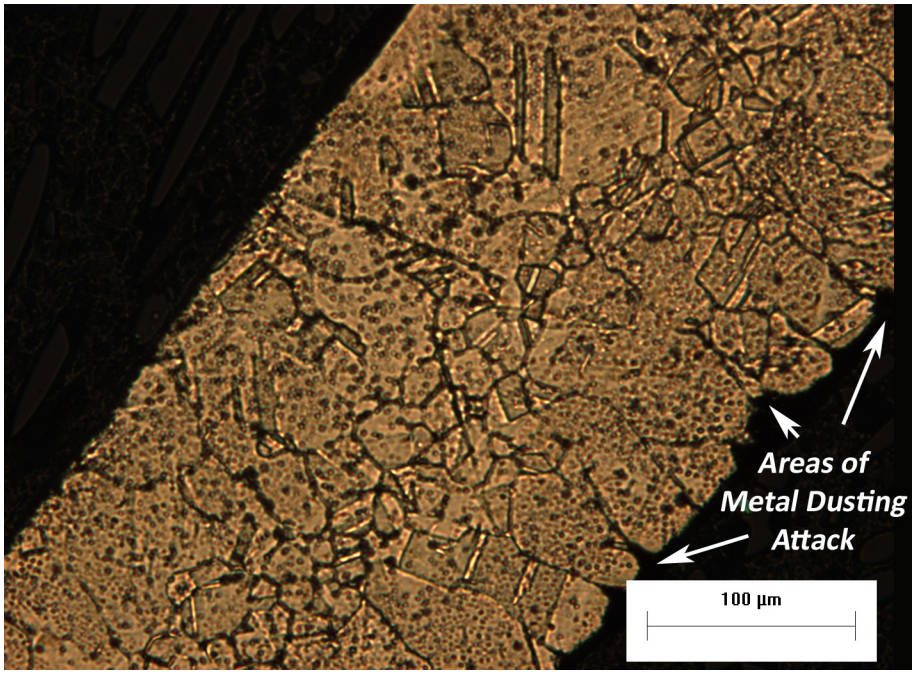

Figure 4.28: Cross-section of a 316 sample carburized for 25 hours at 525°C. Several areas where metal dusting attack into the surface of the part is evident are labelled.

4.6 Heat Treatment Studies

4.6.1 4140 Samples, Oil-Quenched

Figure 4.29 shows an SEM image of the cross-section of sample 4140_carb_16, after quenching in oil. The figure shows an overall martensitic microstructure, as well as significant porosity in the sample (as was discussed in Section 4.4). A decarburized layer is also present in the sample. In comparison, Figure 4.30 shows the control sample (4140_2M_Control) that was heat-treated simultaneously. The control sample shows a layer of oxidation, due to austenitizing of the sample in air, though no decarburized layer is visible. Thus, it can

be concluded that the decarburized layer did not measurably grow during quenching experiments, and the layer is due to slow cooling after gas carburization (as was shown in Section 4.5.2.2). Thus, if samples were quenched immediately after carburization, rather than cooling in argon, it is reasonable to believe that decarburization would not be observed. Additionally, if the CO/CO_2 atmosphere is controlled during cooling, it may be possible to cool quickly enough to avoid decarburization while also avoiding metal dusting.

Figure 4.31 shows higher magnification images of a portion of the cross-section of sample 4140_carb_23 (Figure 4.31 a) as compared to the control sample (Figure 4.31 b) such that the martensitic microstructure can be more easily observed. Pores and unreduced Cr_2O_3 are evident in the carburized sample, and the general size of the martensite laths are slightly smaller than in the control sample.

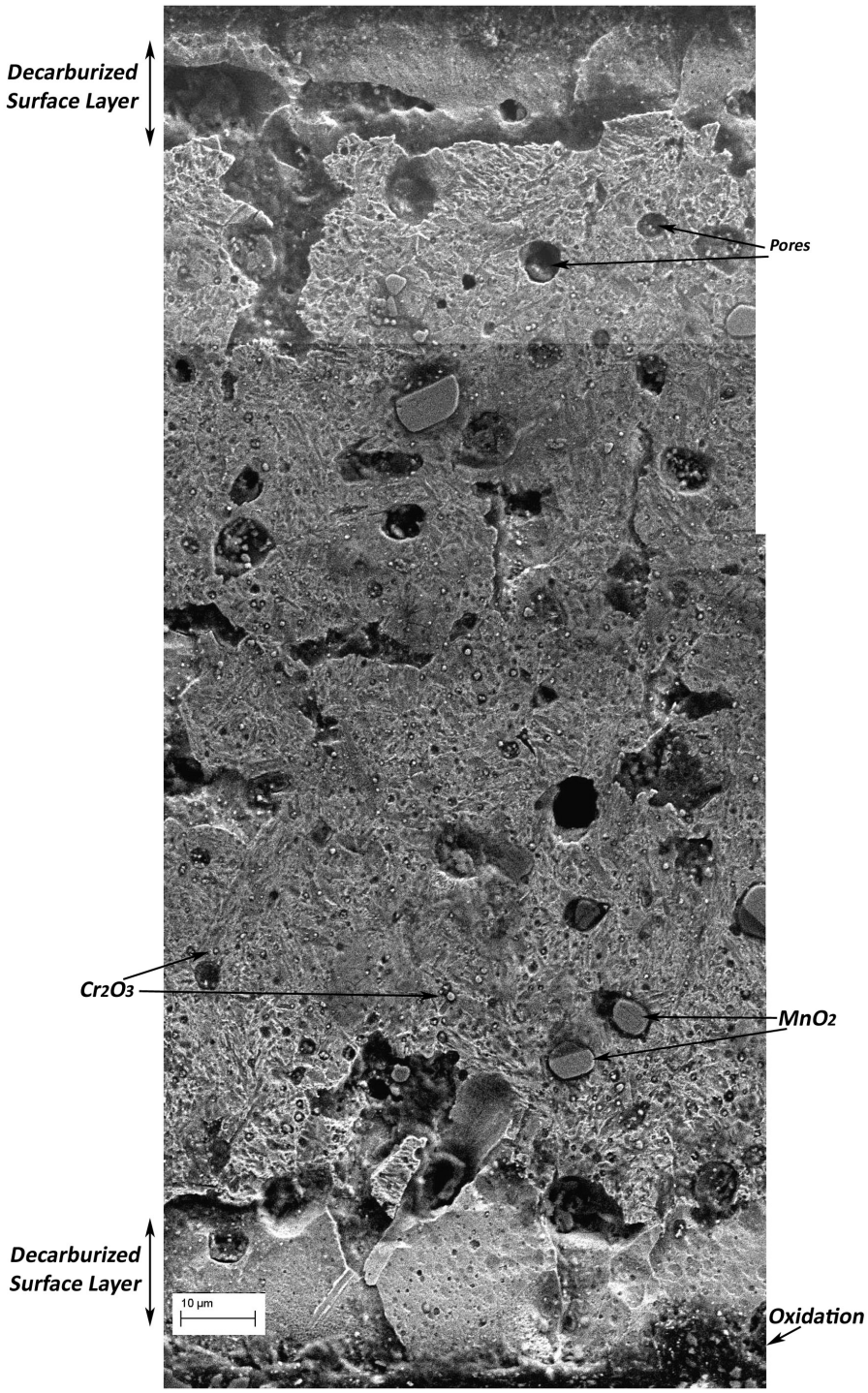

Figure 4.29: SEM image of the cross-section of 4140 strip (sample 4140_carb_16) oil-quenched to martensite.

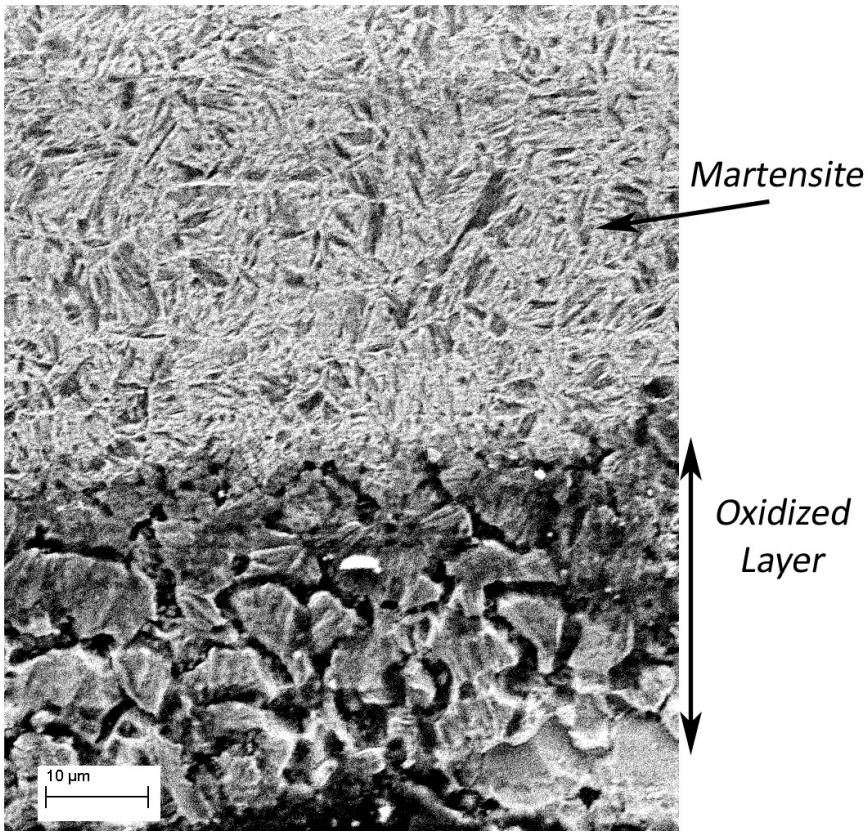

Figure 4.30: SEM image of a portion of the cross-section of a 4140 as-received sample oil-quenched to martensite simultaneously with sample 4140_carb_16.

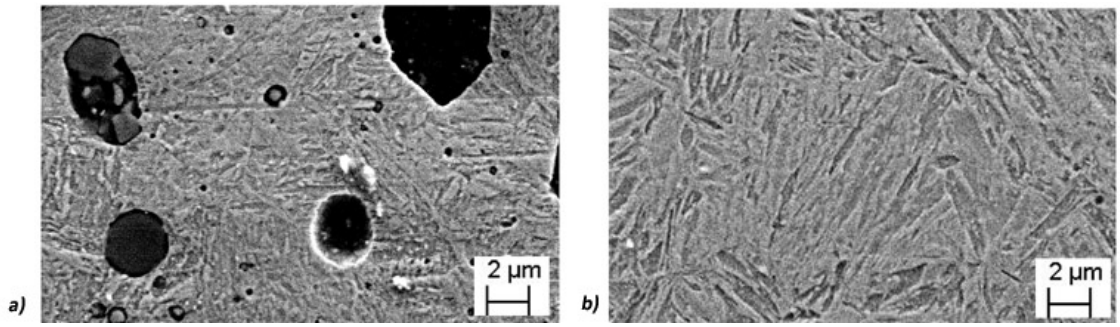

Figure 4.31: Comparison of the martensitic microstructure of an oil-quenched a) gas-carburized sample (4140_carb_23) with a simultaneously treated b) control sample (4140_M3_Control).

4.6.2 4140 Samples, Treated in Molten Salt

Figure 4.32 shows SEM micrographs of samples 4140_carb_23 and 4140_B1_Control, which were heat-treated at 400°C simultaneously to a bainitic structure. The figure shows that the structures are that of upper bainite. In comparison, Figure 4.33 shows SEM micrographs of samples treated at 375°C in molten salt. The figures show a microstructure consisting of a mixture of lower and upper bainite. Lower bainite is evidence by small carbides contained in ferrite plates, as labelled in the figure.

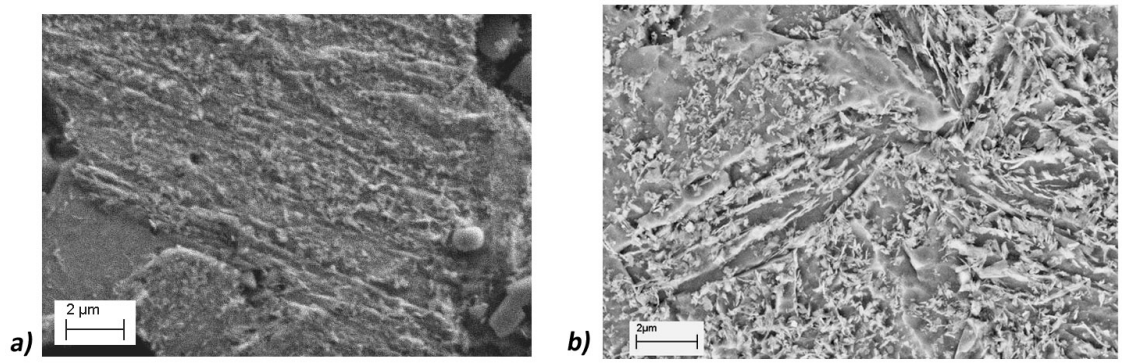

Figure 4.32: Comparison of the bainite microstructure of samples treated in a molten salt bath at 400°C. a) Gas-carburized sample (4140_carb_23) and b) control sample (4140_B1_Control).

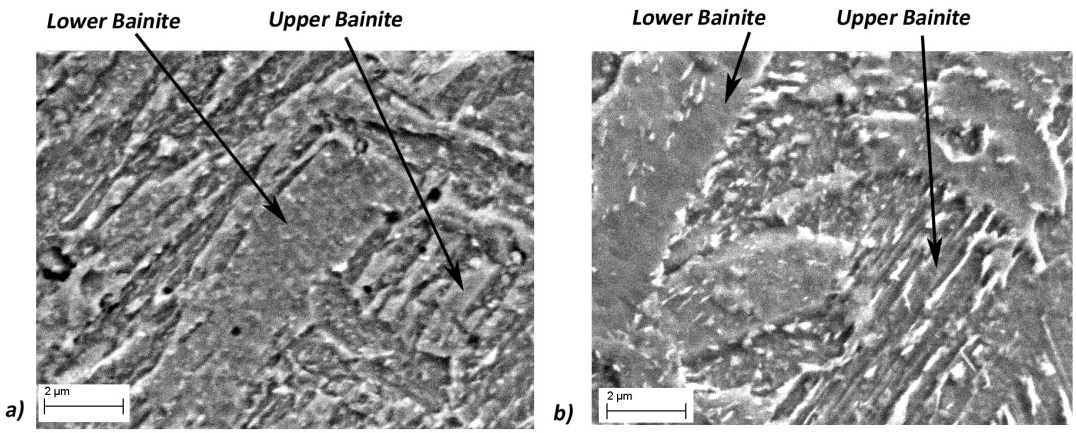

Figure 4.33: Comparison of the bainite microstructure of samples treated in a molten salt bath at 375°C. a) Gas-carburized sample (4140_carb_23) and b) control sample (4140_B2_Control). A mixture of microstructures characteristic of upper and lower bainite are present.

4.7 Mechanical Properties of Carburized Samples

4.7.1 Vickers Microhardness

4.7.1.1 4140 Samples, Cooled Slowly

Table 4.5 shows the average Vickers microhardness measurement for several samples carburized with C_s = 0.4 wt% C, whose calculated carbon content as determined through point counting was less than 0.52 wt% C. Average hardness values do not directly coincide with the carbon content as determined through point counting. For example, sample 4140_2_carb_3 shows a hardness of 162 HV and a carbon content of 0.40 ± 0.04 wt%, while sample 4140_carb_23 shows lower hardness reading of 135 HV though the carbon content as determined through point counting is higher. The control sample heated similarly to those that were carburized also shows good agreement with the values associated with the carburized samples.

In addition, Table 4.6 shows the average Vickers hardness measurement for samples carburized with C_s = 0.4 wt% C, whose calculated carbon content as determined through point counting was greater than 0.52 wt% C. In comparing this with Table 4.5, the Vickers hardness values are very similar to those found in the sample where point counting yielded

carbon contents less than 0.52 wt% C. Additionally, the hardness values measured from the samples shown in Table 4.6 are comparable to that measured in the control sample as well. Because hardness is highly correlated with the carbon content of a low alloy steel, it is reasonable to believe that the carbon contents of these samples are very similar, and point counting can only serve as an *estimate* to the carbon content that has been reached, though its accuracy must be determined. As such, combustion analysis is necessary to confirm the true carbon contents of the samples.

Table 4.5: Vickers microhardness values measured for 4140 samples carburized with C_s = 0.4 wt% C, whose point cointing results yielded an average carbon content less than 0.52 wt%.

Sample Name	Vickers Hardness (HV)	Carbon Content (wt%)
4140_carb_15	156	0.32 ± 0.06
4140_carb_16	167	0.52 ± 0.05
4140_2_carb_31	126	0.33 ± 0.05
4140_carb_23	135	0.52 ± 0.07
4140_carb_24	117	0.36 ± 0.08
4140_2_carb_3	162	0.40 ± 0.04
Control Sample	184	—

Table 4.6: Vickers microhardness values measured for 4140 samples carburized with C_s = 0.4 wt% C, whose point cointing results yielded an average carbon content greater than 0.52 wt%.

Sample Name	Vickers Hardness (HV)	Carbon Content (wt%)
4140_2_carb_25	158	0.70 ± 0.03
4140_2_carb_26	169	0.64 ± 0.06
4140_2_carb_27	122	0.65 ± 0.05
4140_2_carb_28	175	0.72 ± 0.02
4140_2_carb_29	150	0.76 ± 0.00
4140_2_carb_30	186	0.60 ± 0.05
Control Sample	184	—

4.7.1.2 4140 Samples, Oil-Quenched

4140 samples that were quenched in oil to a martensitic microstructure showed higher hardness values than slowly cooled samples, as expected. The three strip samples tested

(4140_2_carb_27, 4140_carb_16, and 4140_carb_23) showed an average hardness reading of approximately 428 HV. In comparison, the average hardness of the three control samples, heat-treated simultaneously with the 4140 strip samples, was 595 HV. The control sample that was heat-treated prior to the quenching experiment (4140_M3_Control) to mimic grain growth that can occur during carburization of the 4140 strip, yielded a hardness value between samples that were tested as-received (4140_M1_Control and 4140_M2_Control). Table 4.7 shows the average microhardness of samples treated in this study.

Table 4.7: Vickers microhardness of 4140 samples quenched to a martensitic microstructure.

Sample Name	Average Hardness (HV)
4140_2_carb_27	389
4140_M1_Control	504
4140_carb_16	429
4140_M2_Control	679
4140_carb_23	487
4140_M3_Control	601

Of the indentations measured on sample 4140_carb_23, four were in areas where large pores were at a minimum, whereas three indents were taken were large pores were evident. Indentations taken where porosity was a minimum (though still present) yielded an average hardness of 568 HV, whereas those taken were large pores were evident yielded a hardness of only 377 HV. The hardness of the control sample treated at the same time (4140_M3_Control) was 601 HV. From this information, it can first be concluded that lower hardness values in the 4140 strip samples as compared to the control samples is due to the porosity associated with the extrusions used in this study. Variations in the hardness measurements of the control samples is due to the time to quench the samples. As

was discussed in Section 3.6, the samples had to be lowered by hand as quickly as possible into the bath furnace, thus the cooling rates of the samples will be slightly different, where slower cooling rates result in lower hardness values. It is thus reasonable to believe that the quenching of these thin-walled structures can be used to produce martensitic microstructures where the hardness is similar to that of conventionally made 4140, provided extrusions are nearly free of pores.

4.7.1.3 4140 Samples, Treated in Molten Salt

Carburized samples, as well as control samples, that were heat-treated in molten salt at 400°C and 375°C showed higher hardness values that slowly cooled samples and lower hardness values than those quenched to martensite, as would be expected. Specifically, a portion of one sample (4140_carb_23) was both quenched in oil as well as treated in the salt bath furnace. As was shown in Table 4.5 and 4.7, the hardness of this sample after slow cooling and after quenching to martensite was 135 and 487 HV, respectively. The hardness of a portion of the same strip when treated in the molten salt at 400°C and 375°C for 60 minutes was 220 and 291 HV, respectively. The hardness of carburized samples treated in the molten salt bath, as well as conventionally produced samples that were treated simultaneously, are shown in Table 4.8.

Table 4.8: Vickers microhardness of 4140 samples treated in molten salt for 60 minutes at various temperatures.

Sample Name	**Temp (°C)**	**Average Hardness (HV)**
4140_carb_23	400	220
4140_B1_Control		321
4140_carb_23	375	291
4140_B2_Control		309

In the case of the control sample that was treated at 400°C (4140_B1_Control), the average hardness was significantly higher than the carburized strip that was treated simultaneously. However, for this sample, five indententations were taken to measure hardness, two of which were in areas where porosity was noticeably less than the other indentations. The average microhardness reading for these two indentations was 275 HV, much closer to the value (321 HV) of the control sample. Like samples quenched to martensite, it can be concluded that the carburized samples can be heat-treated to reach similar values to conventionally produced samples, provided extrusions are nearly defect free.

4.7.1.4 316 Samples

Figure 4.34 shows a micrograph of the cross-section of a sample carburized for 25 hours at 525°C, showing the indents through the cross-section as well as the corresponding hardness values of those indents. Note that error bars are not visible on the graph as the error associated with measurements was lower than the size of the data points used. In the figure, the indents closest to the edge of the sample were not measured, as they appeared to have indented the mounting epoxy slightly. It can be seen from the remaining indents that the hardness of the sample decreases toward the center, thus suggesting that carburization has successfully taken place.

Similarly, Figure 4.35 shows the hardness of indents taken through the cross-section of a 316 sample carburized for 7 hours at 525°C. Comparison of Figures 4.34 and 4.35 show that the sample carburized for 25 minutes resulted in higher hardness values, as would be expected due to the larger diffusion time allowed.

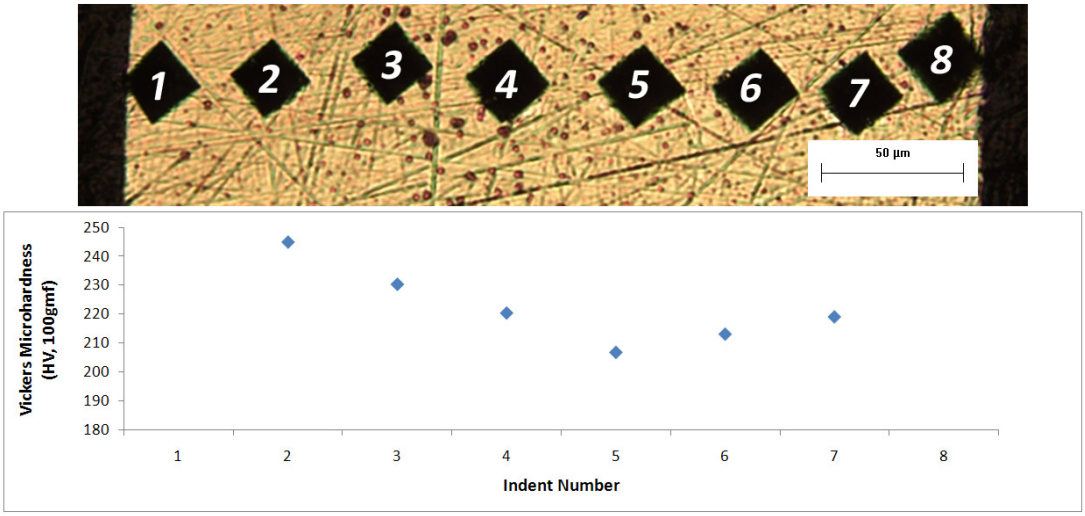

Figure 4.34: Optical micrograph of Vickers microhardness indents through the cross-section of a 316 sample carburized for 25 hours, shown with corresponding microhardness values.

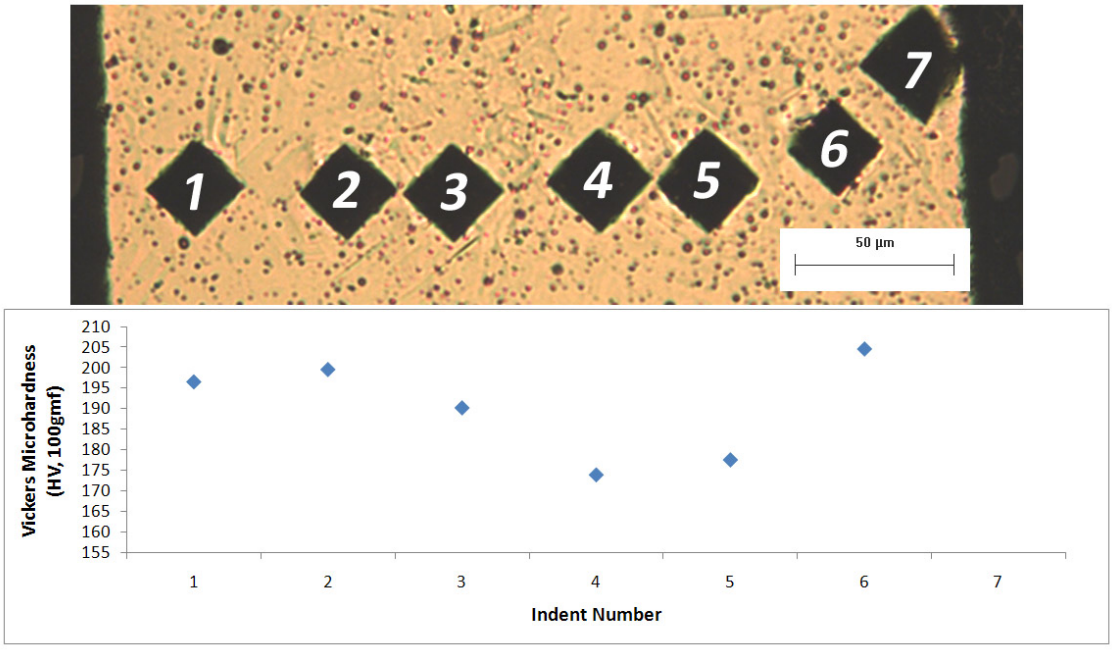

Figure 4.35: Optical micrograph of Vickers microhardness indents through the cross-section of a 316 sample carburized for 7 hours, shown with corresponding microhardness values.

For comparison, a sample of 316 strip that was not carburized was also indented and can be seen in Figure 4.36. From the figure, it can be seen that the hardness on the surface of the sample is not higher than the center, as was shown in the carburized samples. This data suggests that some successful carburization has taken place, though more analysis is necessary to determine the amount of carbon in the sample. It is important to note that the hardness values for the sample that was not carburized are at times higher than those that were carburized. This is because carburized samples were heated for 7 and 25 hours at 525°C, resulting in grain growth and lower hardness values, while the control sample was not heat-treated prior to indentation.

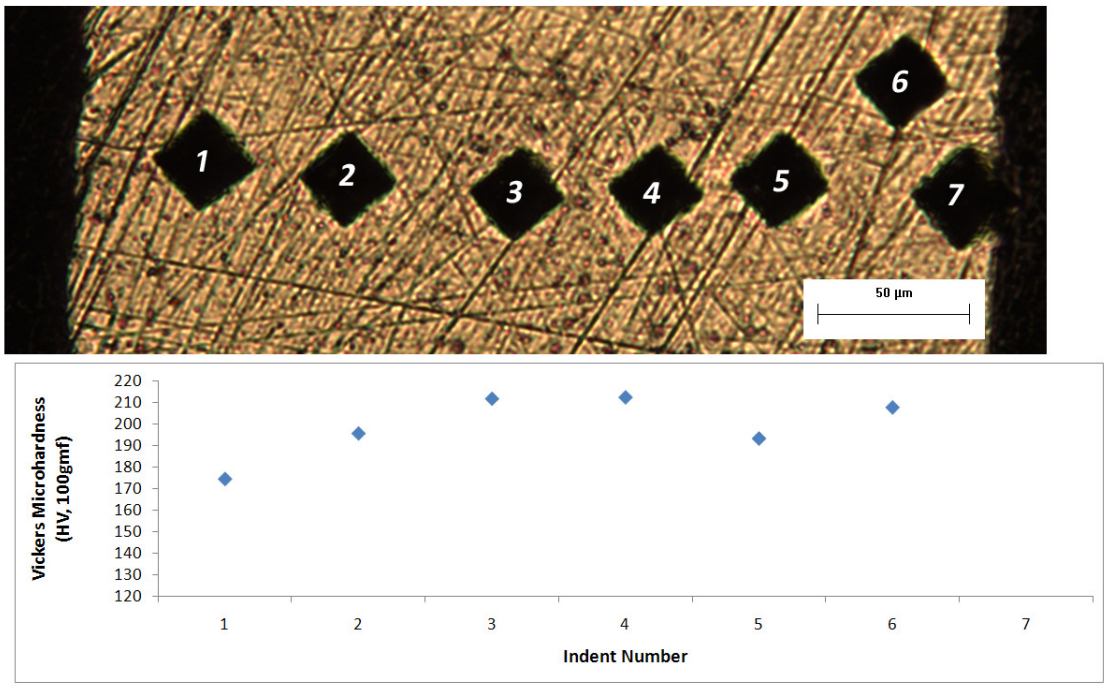

Figure 4.36: Optical micrograph of Vickers microhardness indents through the cross-section of a 316 sample that was not carburized, shown with corresponding microhardness values.

4.7.2 Compression Testing

Figures 4.37, 4.38 and 4.39 show the load vs. displacement curves obtained from compression testing for spheres with no carbon, spheres carburized with 97% CO for 60 minutes,

and spheres carburized with 98.7% CO for 60 minutes, respectively. The graphs have been corrected for compliance. Evident in the figures is the highly brittle nature of the spheres carburized with 98.7% CO (Figure 4.39), seen as large drops in the load over very small displacements. In Figure 4.38 the slightly brittle nature of spheres carburized with 97% CO is evident, though it is not to the extent as spheres carburized with 98.7% CO, as would be expected. The range of load values within each batch of spheres as is seen in the figures is due to the varying wall thicknesses and diameters of the spheres.

Figures 4.40, 4.41 and 4.42 show the wall stress vs. strain on spheres with no carbon, spheres carburized with 97% CO for 60 minutes, and spheres carburized with 98.7% CO for 60 minutes, respectively. From the figures, it can be seen that both sets of carburized spheres exhibit higher wall stresses than those that were not carburized.

Figure 4.43 shows a plot of the relative density of the spheres vs. the maximum stress observed during compression testing of each sphere. From the figure, it can be seen that there is a large variation of the maximum stress within each group of samples, and curve fitting of the behavior does not yield a very good fit. Behavior of the spheres is not very predictable, as the relative densities of the spheres are not consistent. Also, as was shown in Section 4.5.3, the sphere walls are highly porous and significant decarburization has occurred through the sphere walls upon cooling after carburization. As a result, it is reasonable to believe that if decarburization can be controlled through the cooling of the spheres, as well if nearly defect free sphere walls can be produced, the maximum stresses on the spheres can be significantly increased.

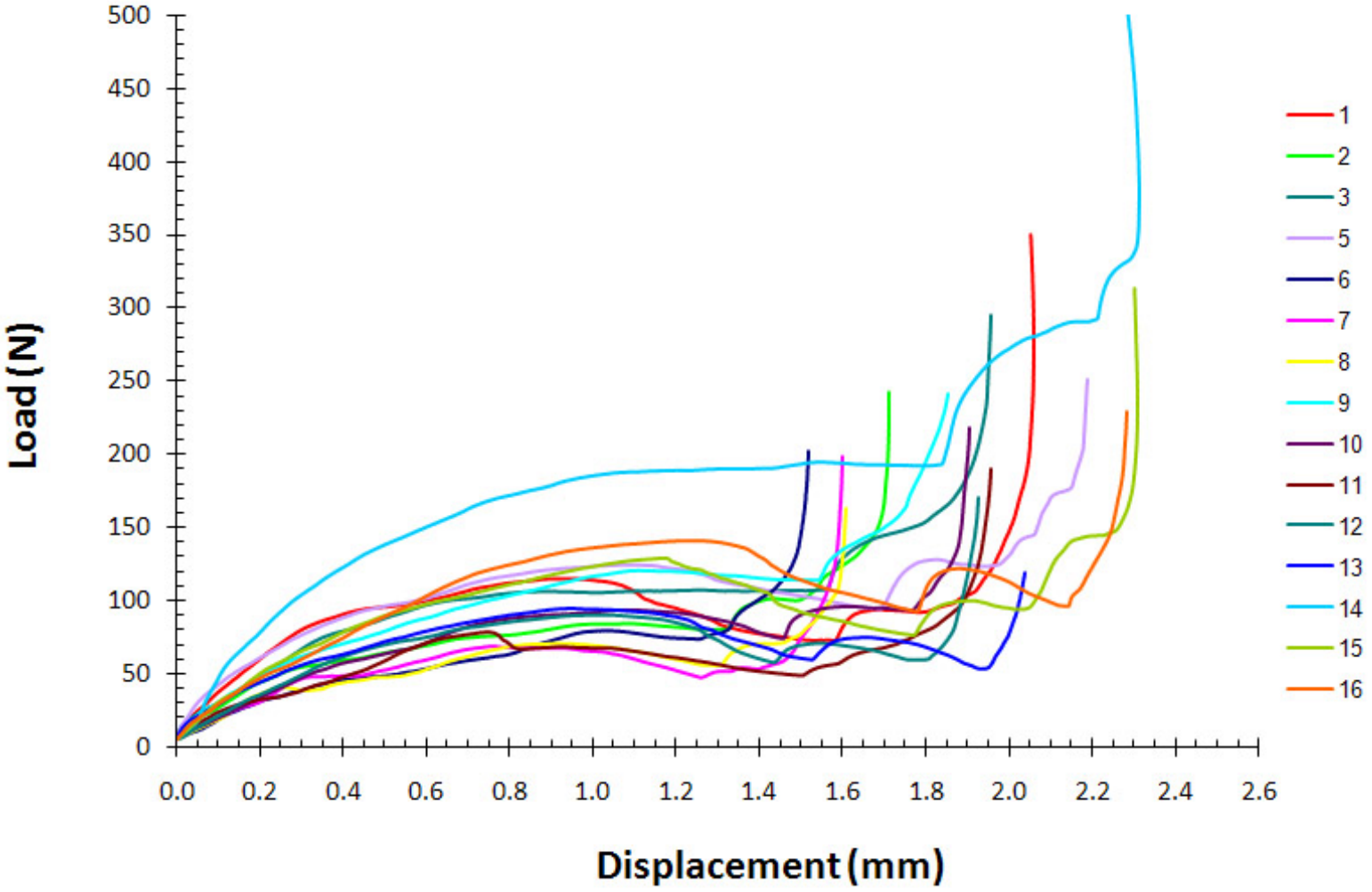

Figure 4.37: Load vs. displacement for 4140 hollow spheres without carbon, corrected for compliance.

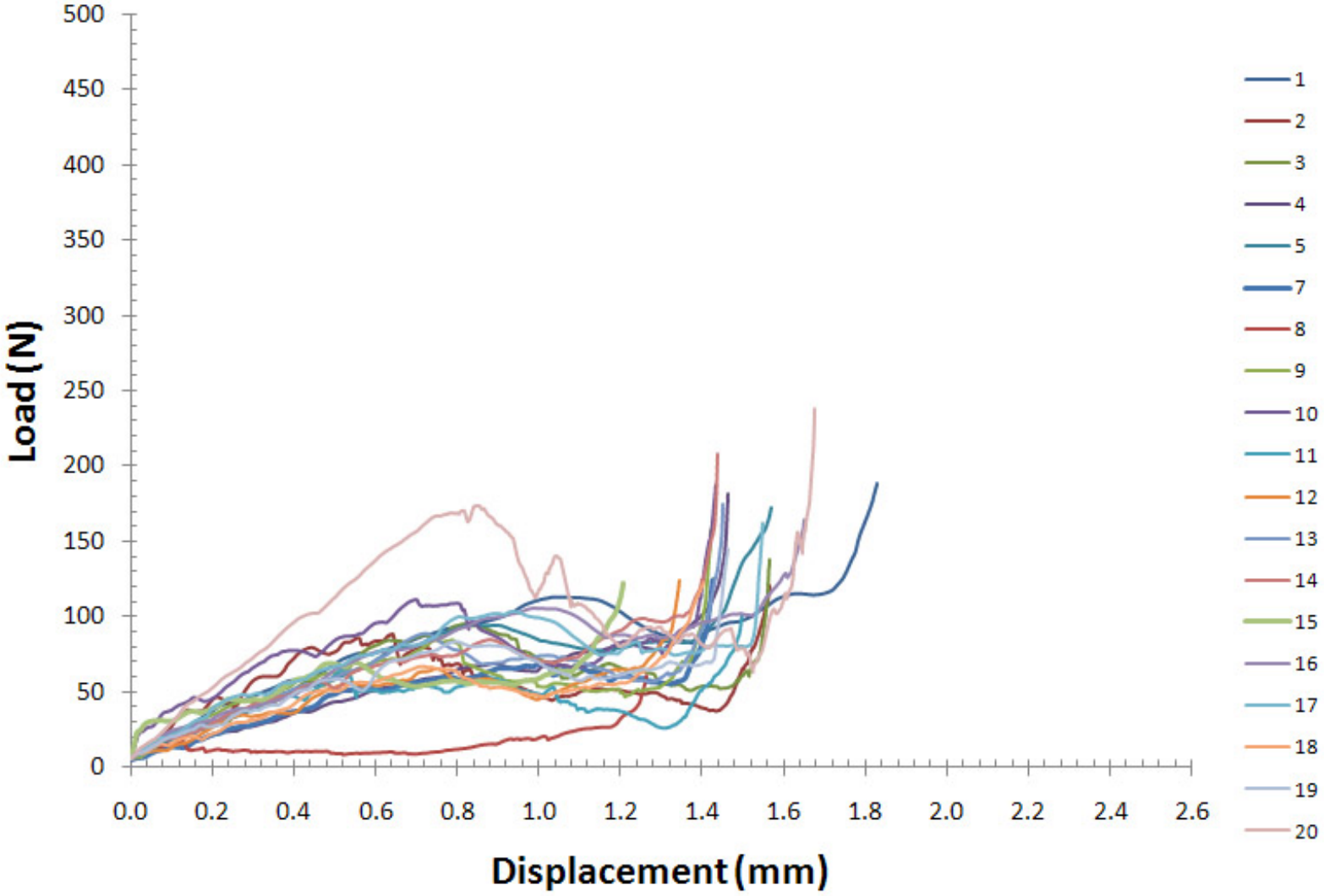

Figure 4.38: Load vs. displacement for 4140 hollow spheres carburized with 97% CO for 60 minutes at 1000°C, corrected for compliance.

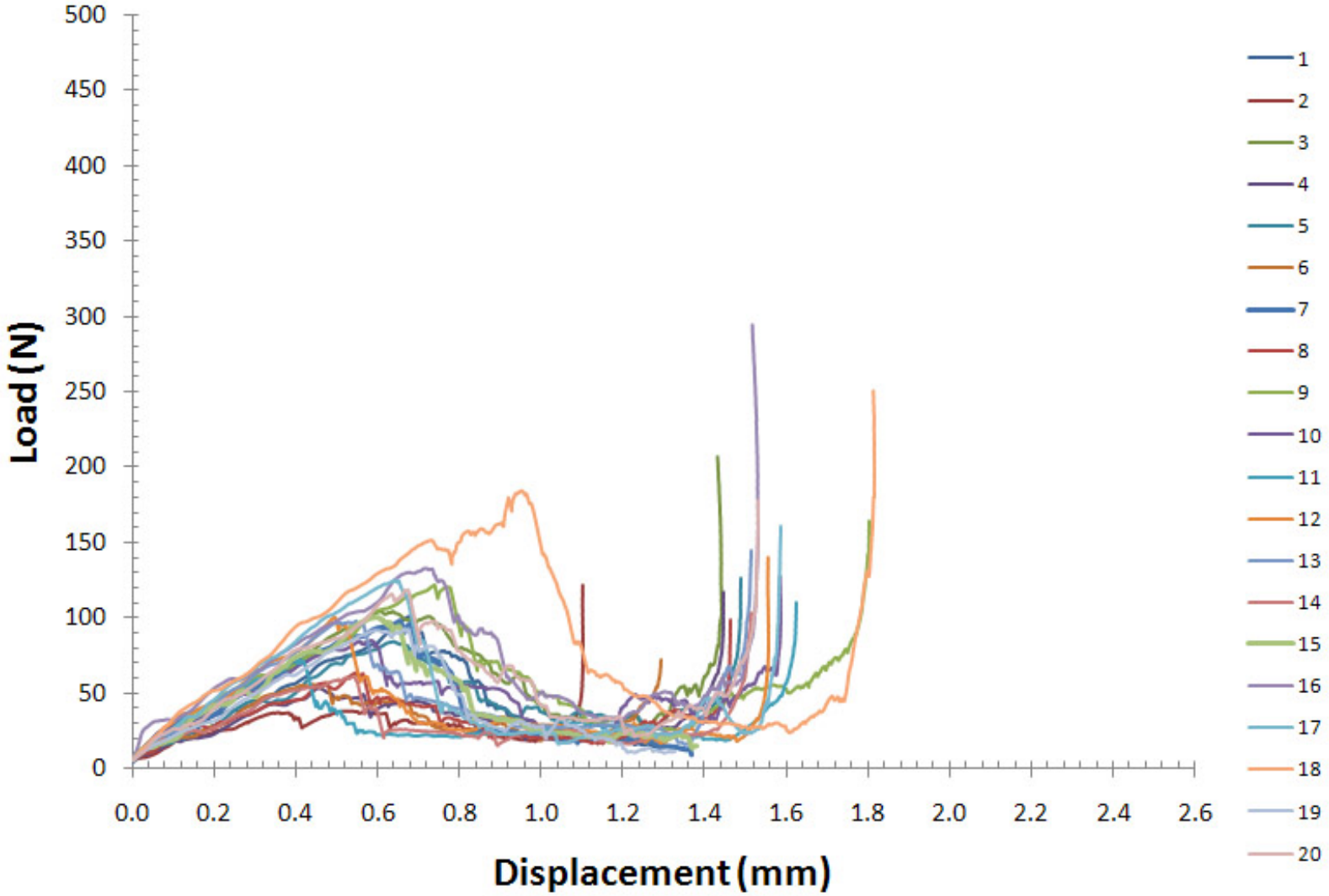

Figure 4.39: Load vs. displacement for 4140 hollow spheres carburized with 98.7% CO for 60 minutes at 1000°C, corrected for compliance.

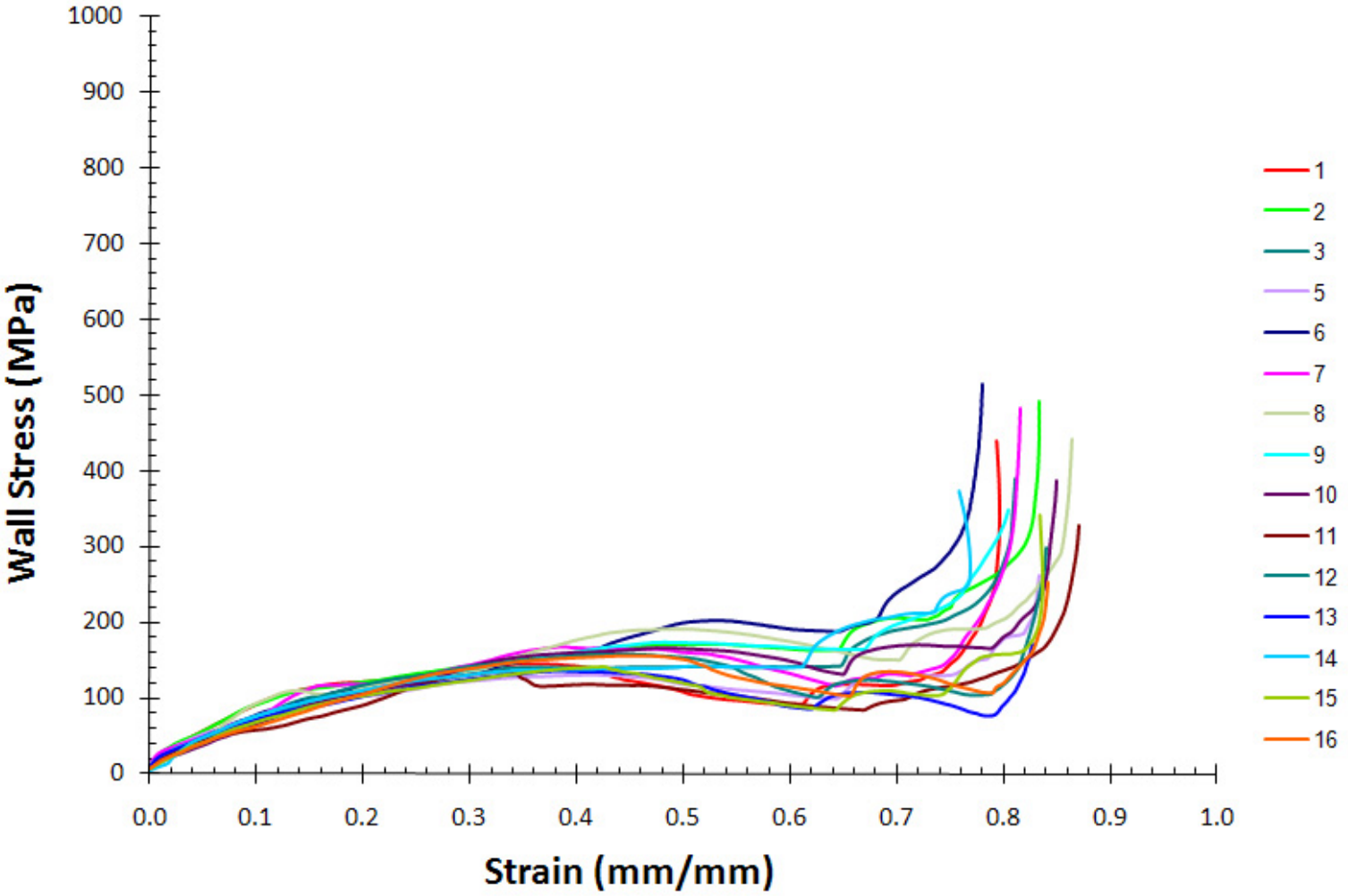

Figure 4.40: Wall stress vs. sphere strain for 4140 hollow spheres without carbon.

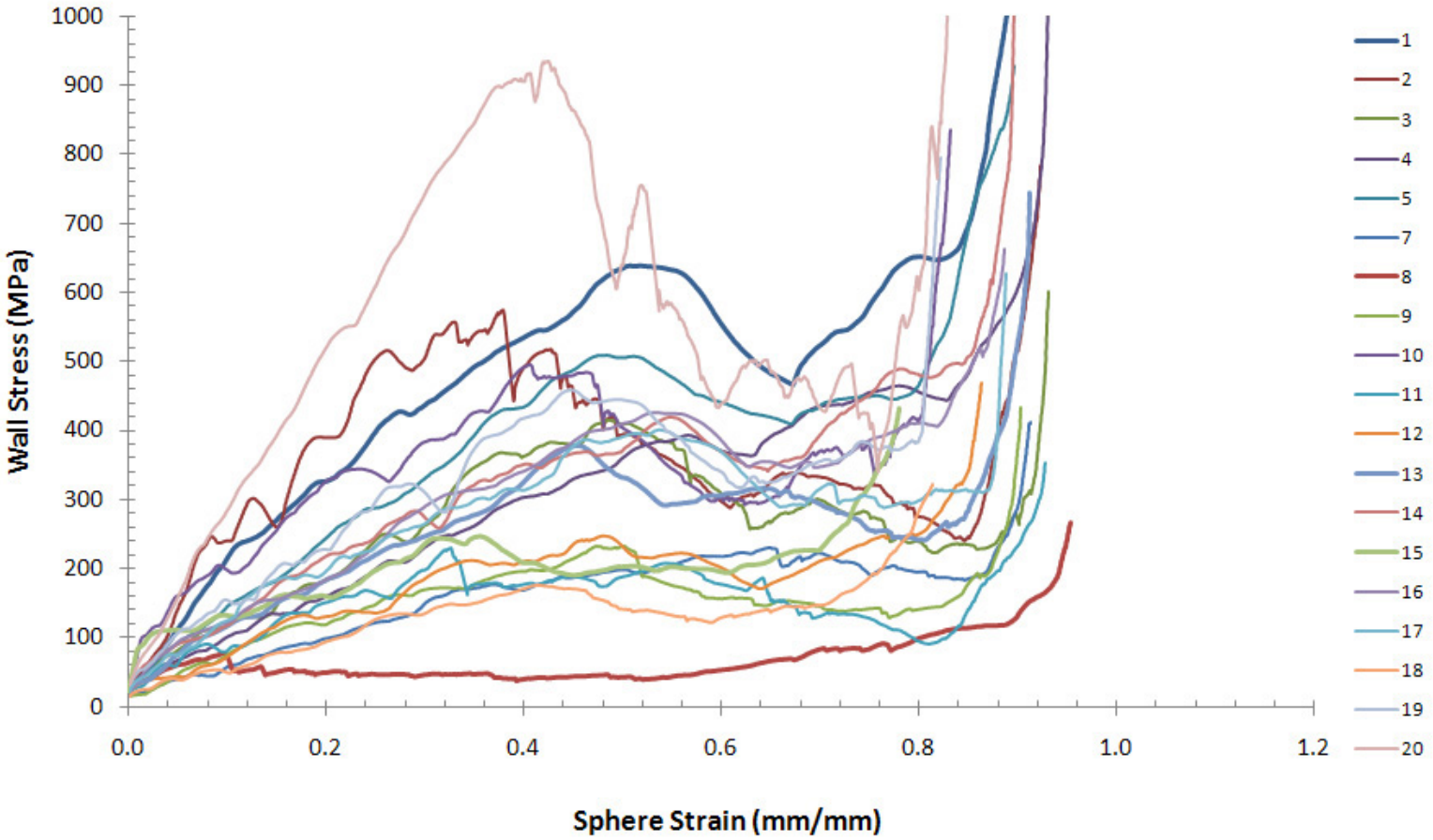

Figure 4.41: Wall stress vs. sphere strain for 4140 hollow spheres carburized with 97% CO for 60 minutes at 1000°C.

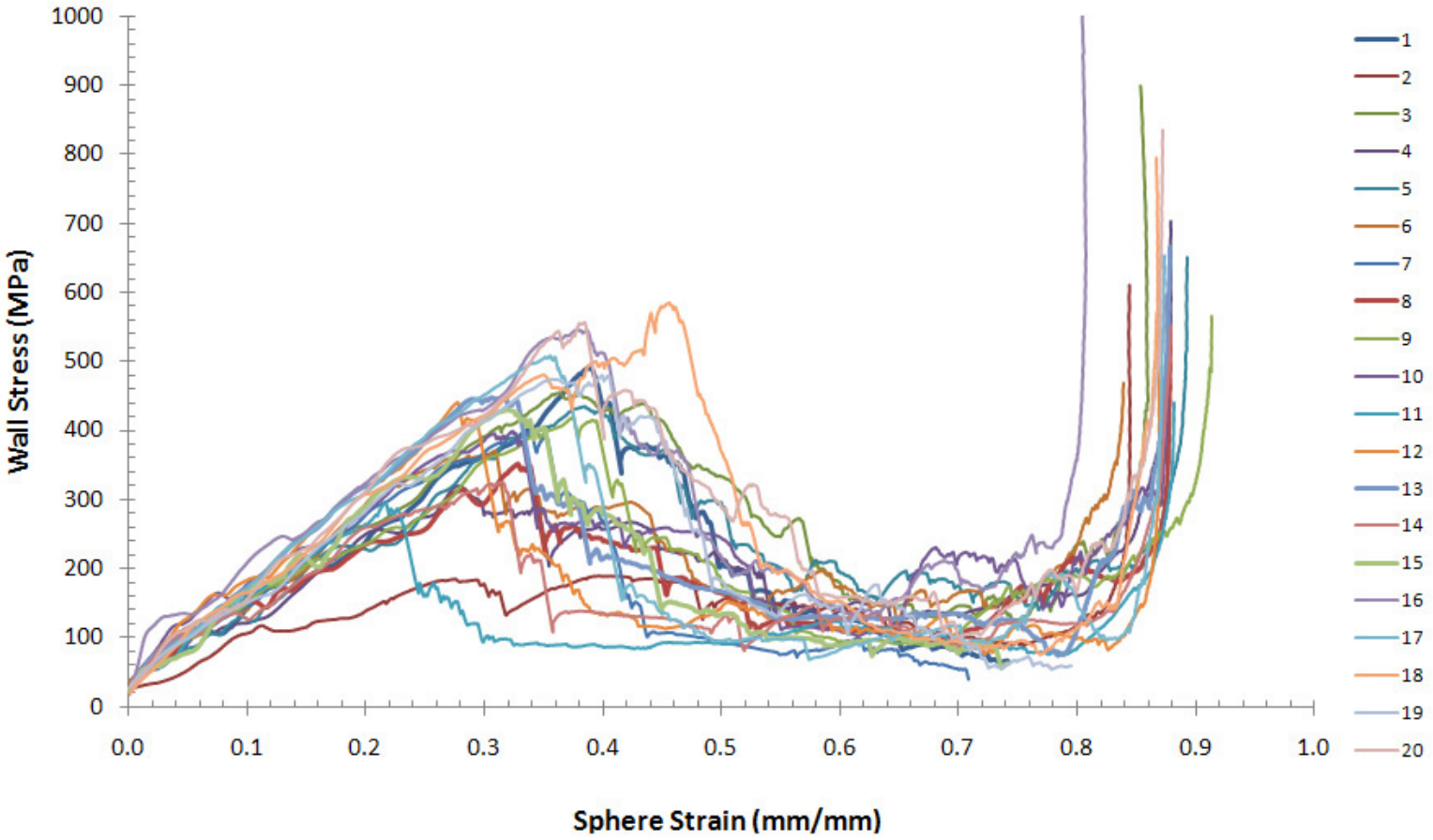

Figure 4.42: Wall stress vs. sphere strain for 4140 hollow spheres carburized with 98.7% CO for 60 minutes at 1000°C.

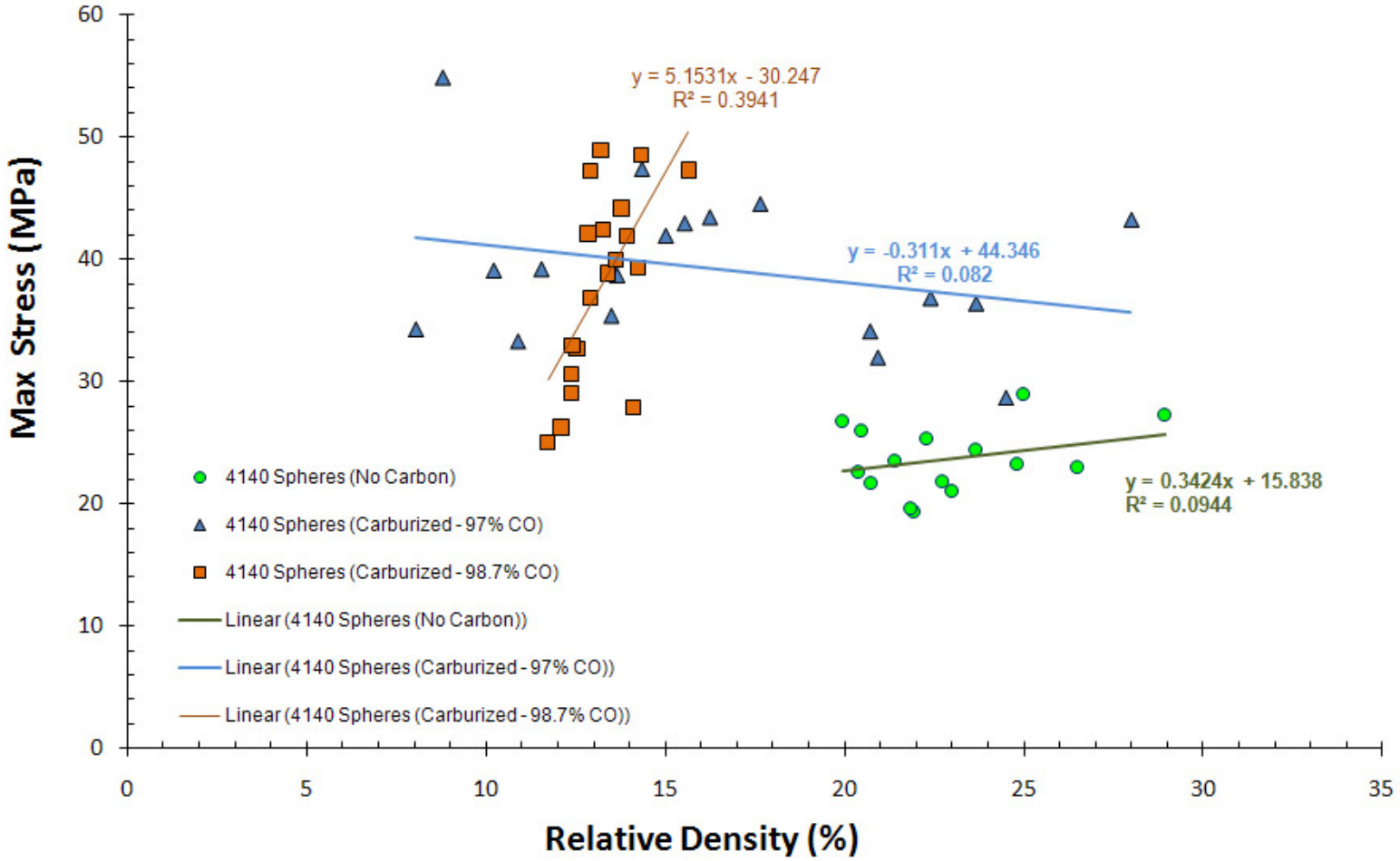

Figure 4.43: Maximum stress upon loading vs. relative density for 4140 spheres without carbon and those carburized with 97% and 98.7% CO for 60 minutes at 1000°C.

4.8 Combustion Analysis of Carburized 4140 Samples

Figure 4.44 shows a plot of the carbon content as determined through combustion techniques vs. that which was determined through point counting for several samples carburized with a 96.15% CO - 3.85% CO_2 atmosphere (such that C_s = 0.40 wt% C according to Smith [38]). From the figure, it can be seen that in general, point counting overestimated the actual carbon content of the carburized part. In all cases, the true carbon content as determined through combustion analysis was closer to the expected value (0.37-0.43 wt% C) than what was estimated through point counting. It is important to note that error bars are not visible on the figure for samples that were tested via combustion analysis as errors are only on the order of 0.02-0.04%. Of the six samples tested, the carbon contents range from 0.379 to 0.586 wt%. However, it was also previously concluded (see Section 4.5.2.2) that samples carburized for 15 minutes did not show results with reliable repeatability. Thus, the true range of carbon contents for samples carburized using the outlined technique (samples carburized for times greater than 30 minutes) is 0.427-0.586 wt%.

Several samples that were carburized with C_s = 1.0 wt% C were also sent for combustion analysis. Like those treated with C_s = 0.4 wt% C, the true carbon content of these samples is lower than what was determined through point counting, as is shown in Figure 4.45. Larger errors in point counting results are due to the high sensitivity of the carbon content as related to the volume fraction of pearlite at compositions above the eutectoid. As was discussed in Section 4.5.2.2, point counting measurement errors remained very similar to those measurements for samples carburized with C_s = 0.4 wt% C, but this translates to a larger error in the carbon content when using the lever rule above the eutectoid composition.

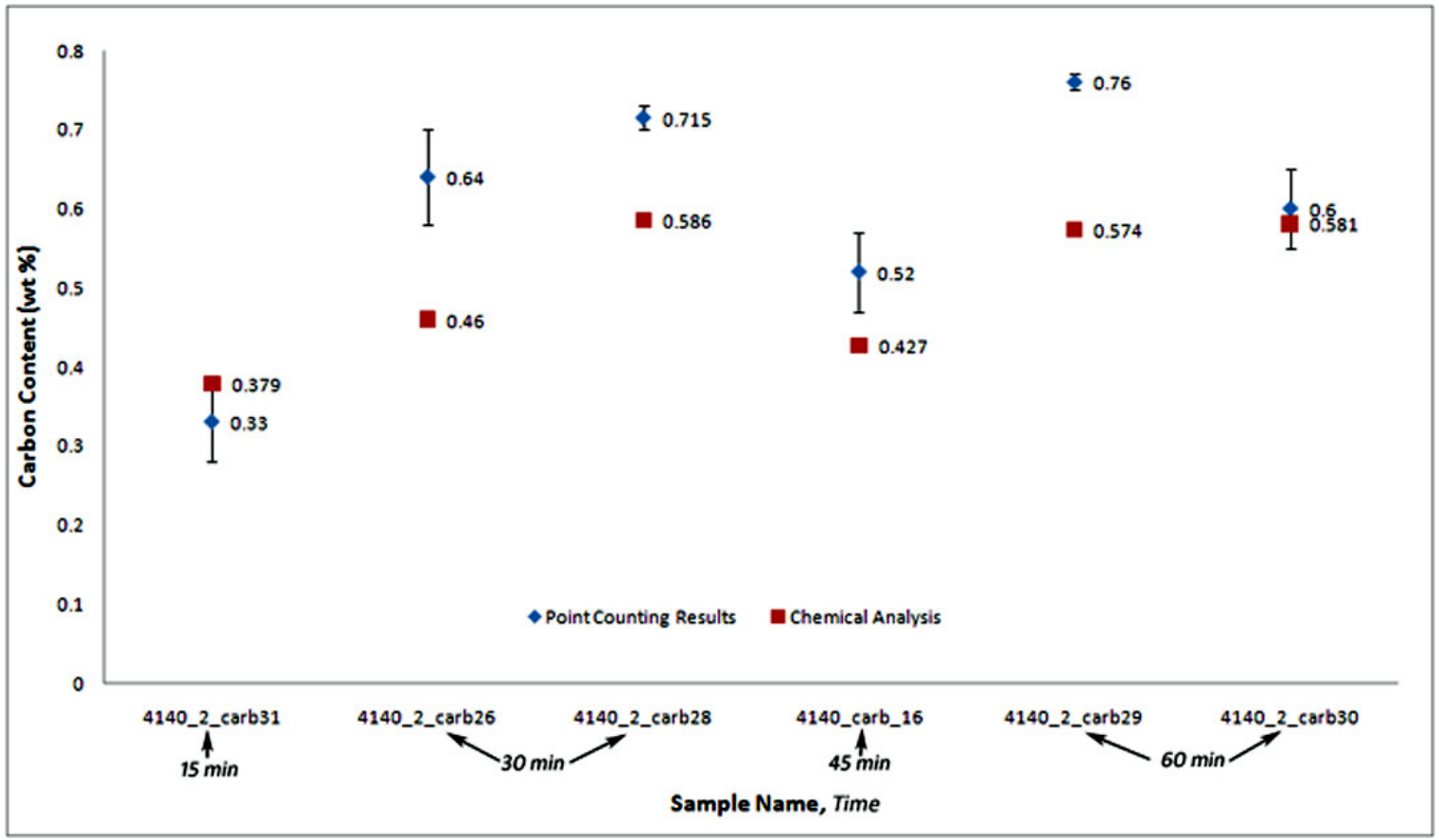

Figure 4.44: Comparison of point counting results vs. the carbon content, as determined through combustion analysis, of several 4140 samples carburized with C_s = 0.40 wt% C.

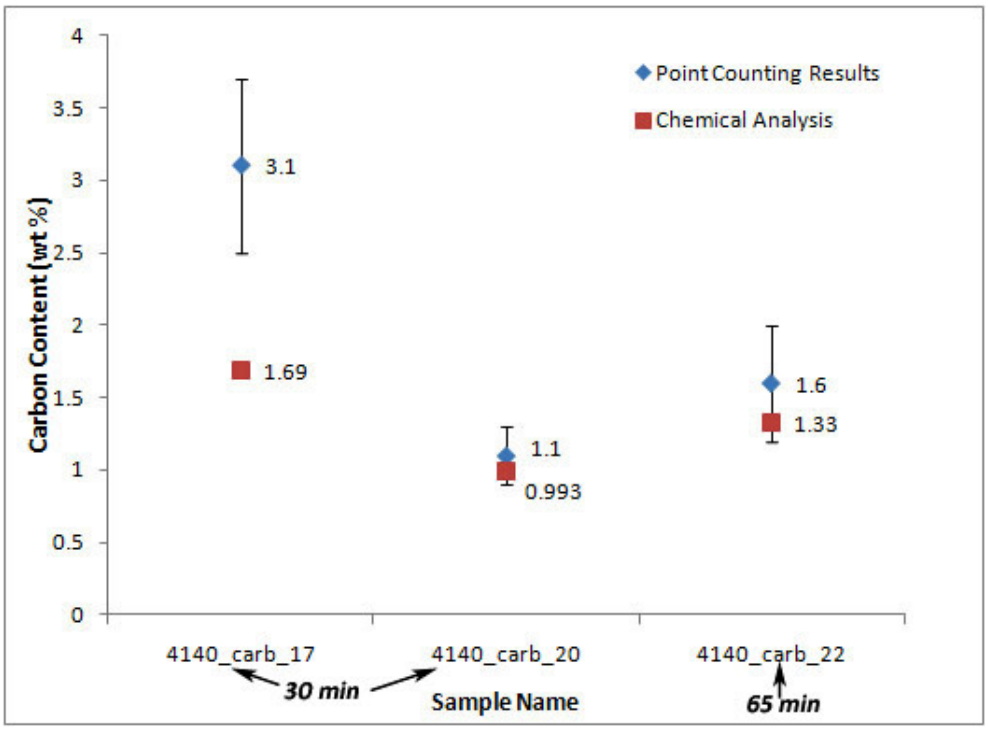

Figure 4.45: Comparison of point counting results vs. the carbon content, as determined through combustion analysis, of several 4140 samples carburized with C_s = 1.0 wt% C.

4.8.1 Experimental Results vs. Previously Published Results

Figure 4.46 shows the carbon content as determined through combustion analysis of samples carburized with C_s = 0.40 wt% C according to both Smith [38] and Stanley [25], for 30 minutes. From the figure, it can be seen that samples carburized according to Smith's predictions (96.15% CO - 3.85% CO_2) are much closer to the composition of interest (0.37-0.43 wt% C) than those carburized according to the mathematical predictions outlined by Stanley (97.2% CO - 2.8% CO_2).

Also of interest is Figure 4.47, which plots the equilibrium surface concentration as determined by Smith and Stanley for different atmospheres at 1000°C, compared to the results of combustion analysis experiments done on the samples carburized in this study. From this figure, it is also shown that the equilibrium surface concentration as determined by Smith are closer to the values obtained in gas carburization experiments in this study,

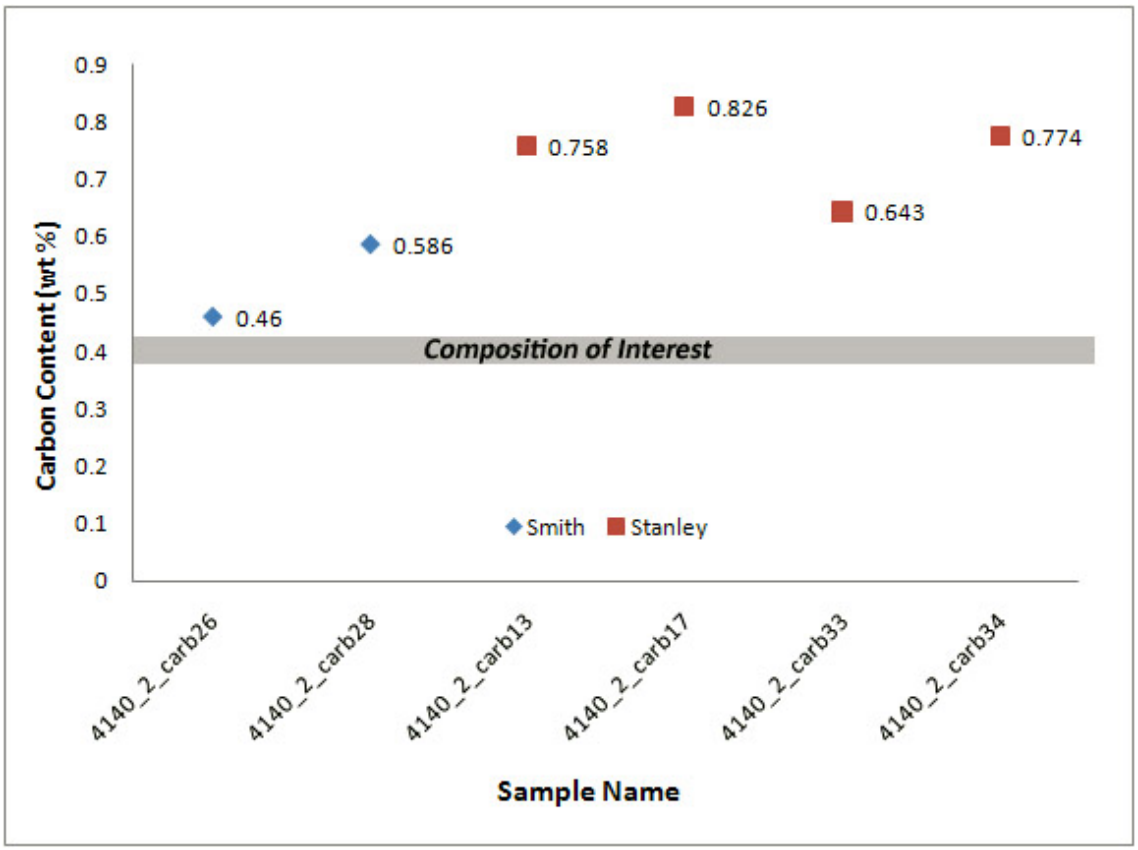

Figure 4.46: Comparison of the carbon content of samples, as determined through combustion analysis, for samples carburized with C_s = 0.40 wt% C according to R. Smith vs. according to Stanley. The carbon content of a 4140 steel is shown as a shaded region in the figure.

than those predicted mathematically by Stanley.

The most likely factor for the true carbon contents being slightly higher than the target composition is due to the sensitivity of the equilibrium surface concentration to the atmosphere composition. Slight changes in the flow of CO or CO_2 at compositions near that necessary for both C_s = 0.40 wt% C and C_s = 1.0 wt% C can greatly alter the equilibrium surface concentration of the part (see Figure 3.6, Section 3.5.3.1). Also, the temperature during carburization can also affect the equilibrium surface concentration as well. For example, according to the calculations presented in Section 2.2.1.1 as outlined by Stanley, for a 96.15% CO/CO_2atmosphere, the equilibrium surface concentration of carbon increases by 0.06 wt% when dropping the temperature only 20°C. Thus the carburization process is highly sensitive to both fluctuations in the mass flow of the carburizing gases as well as to the temperature during carburization.

Alternate factors also play a role in the carburizing behavior of 4140 steel. For example, the mass transfer of carbon to the surface of the part increases over that of a plain carbon steel due to the Cr and Mo additions that are present in 4140, thus carburization is faster. Also, the tendency for Cr and Mo to form carbides in the temperature range in which carburization takes place can also play a role in the carburization of the strip. Lastly, researchers have used Thermo-Calc software to show that, at temperatures similar to those used in this study, the equilibrium surface concentration for steels containing Cr and Mo contents that are similar to that of a 4140 steel result in values that are slightly higher (approximately 0.01 wt%) than a plain carbon steel in the same atmosphere [37].

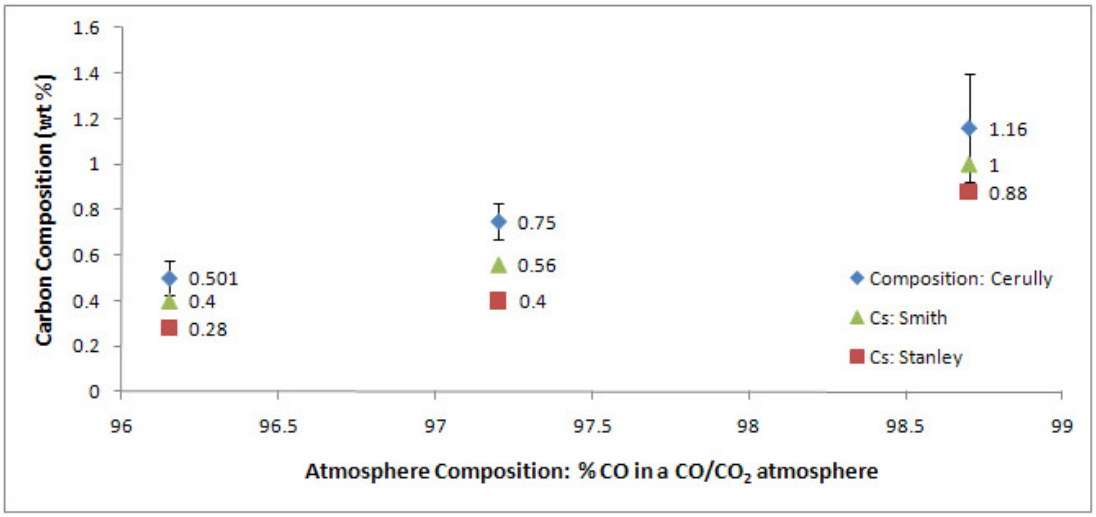

Figure 4.47: Comparison of the equilibrium surface concentration as determined by Smith and Stanley for different atmospheres at 1000°C, compared to the results of combustion analysis experiments done on 4140 samples carburized in this study (Cerully).

4.9 Decarburization Studies

4.9.1 Decarburization in Air

Samples heat-treated in air for 100 minutes showed significant amounts of oxidation. Figures 4.48 a) and b) show SEM images of samples treated at 700°C and 950°C, respectively. The increase in oxidation layer thickness is evident in the micrographs.

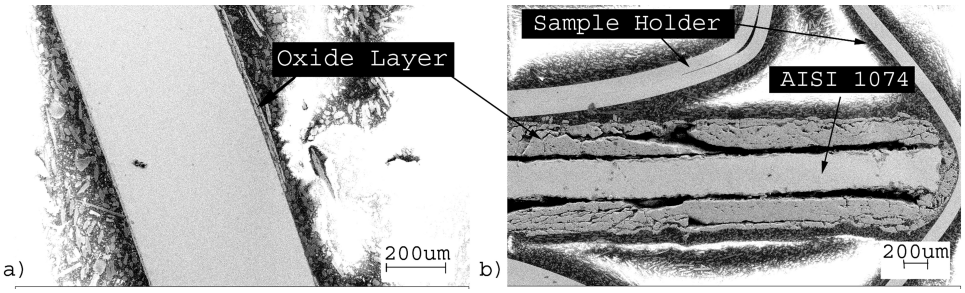

Figure 4.48: Optical micrographs of the cross-sections of AISI 1074 samples heated in air for 100 minutes at a) 700°C and b) 950°C. A large oxidation layer is evident in the sample treated at 950°C.

Figure 4.49 shows an optical micrograph of a sample treated in air at 800°C, where light areas depict areas of decarburization. Elongated grains are evident in the decarburized layer, which can be explained through the Fe-Fe_3C phase diagram as was previously shown in Figure 2.19 (Section 2.5.1). At 800°C, during decarburization, the carbon composition reaches the two-phase, ferrite (α) + austenite (γ), region prior to cooling. As a result, ferrite grains grow into the austenite region during the dwell at 800°C. Subsequent cooling of the sample results in elongated ferrite grains in the decarburized layer and homogenously nucleated pearlite colonies in areas which have not been decarburized. At temperatures greater than the peak of the ferrite/austenite two-phase field (912°C), grain elongation is not expected, as ferrite nucleates upon cooling, rather than during heat treatment. Figure 4.50 shows optical micrographs of a sample treated at 950°C. Decarburization through the entire sample cross-section (Figure 4.50 a) and the absence of elongated grains (Figure 4.50 b) are evident in the micrographs.

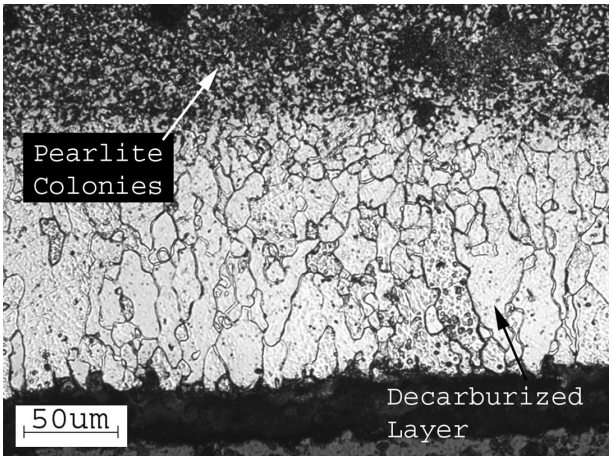

Figure 4.49: Optical micrograph of the edge of an AISI 1074 sample heated in air for 100 minutes at 800°C. A decarburized zone (approximately 135 μm thickness) is evident along the edge of the sample with pearlite colonies toward the interior of the sample.

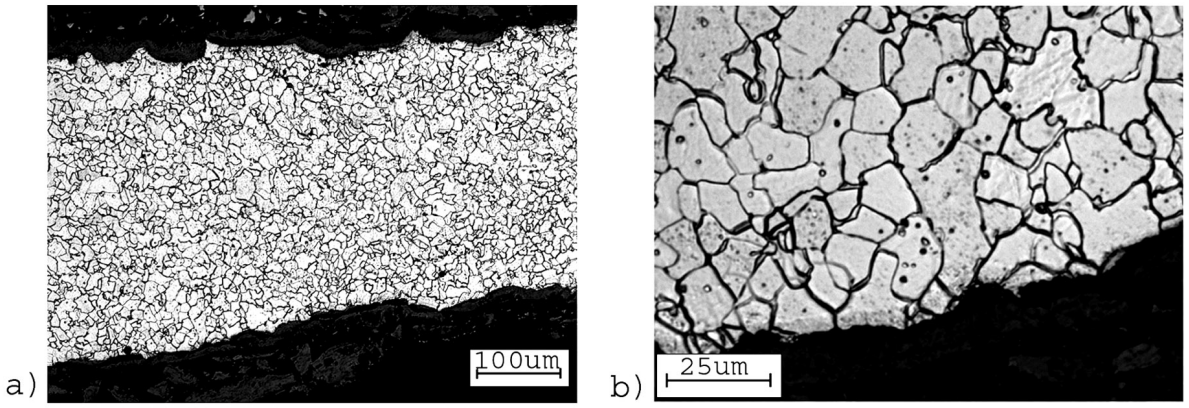

Figure 4.50: Optical micrographs of the cross-section of an AISI 1074 sample heated in air for 100 minutes at 950°C. Complete decarburization of the sample is evident (a) as well as the absence of elongated grains (b).

The decarburization measured in each of the samples was compared to that predicted through Equation 18, as was previously discussed in Section 2.4. For the calculations, the preexponential factor (D_o) and activation energy (Q) were 0.394 mm^2/sec and 80.22 kJ/mol, respectively. For this study, C_b was estimated using the Fe-Fe_3C phase diagram.

Good agreement was seen between the model's predictions and the sample treated at 800°C (Figure 4.49); however, at temperatures below the eutectoid (727°C), the model does not hold. Figure 4.51 shows such a sample, which was treated at 700°C in air for 100 minutes. Equation 18 predicts a decarburization depth of approximately 300 μm. However, it is evident that this magnitude of decarburization has not occurred in the specimen. The micrograph shows a small decarburized layer (in most areas, approximately 10-20 μm thick) and an increase in the volume fraction and size of carbides toward the center of the sample. The microstructure itself is spheroidite, as was discussed in Section 2.5.1.1. Due to the presence of carbides below the eutectoid temperature, a different model to predict decarburization depth must be developed. Specifically, the model must account for the dissolution of carbides which occurs prior to the diffusion of carbon through ferrite in the case of a spheroidite microstructure.

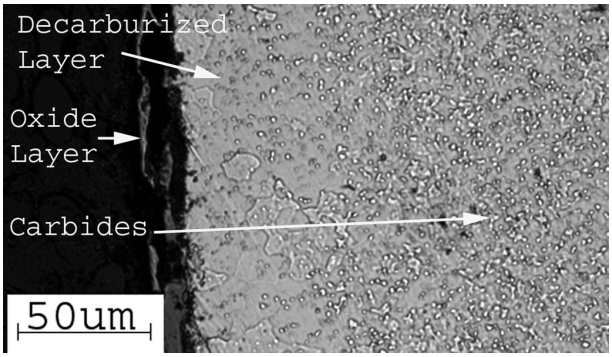

Figure 4.51: Optical micrographs of the cross-section of an AISI 1074 sample heated in air for 100 minutes at 700°C. An oxide layer and a layer of decarbuization are evident in the micrograph. The volume fraction and size of carbides increases toward the interior of the sample.

4.9.2 Decarburization in 4% H_2/Ar

Figures 4.52 to 4.55 show micrographs of the cross-sections of AISI 1074 samples heated to 700°C, 850°C, 950°C, and 1050°C, respectively in a 4% H_2/Ar atmosphere. An optical micrograph and SEM image of the specimen heated to 700°C for 60 minutes is shown in

Figures 4.52 a and b, respectively. Decarburization has occurred along the edge of the sample, and some channels of decarburization are evident throughout the cross-section of the sample. Figures 4.53 a and b show an optical micrograph and SEM image, respectively, of the sample heated to 850°C for 60 minutes. It is evident from these images that at 850°C, decarburization has occurred throughout the cross-section of the sample and along the edge of the sample as well.

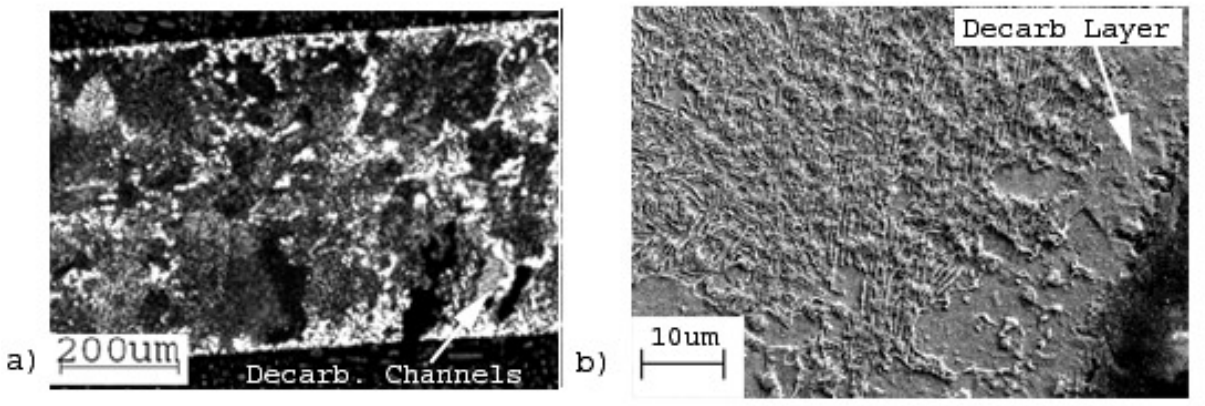

Figure 4.52: (a) Optical micrograph of the cross-section and b) SEM image of the edge of an AISI 1074 sample heated to 700°C for 60 minutes in 4% H_2/Ar. Light areas depict areas of ferrite while dark areas are pearlite. Decarburization channels are evident through the sample (a) as well as a decarburized layer along the edge of the sample (b).

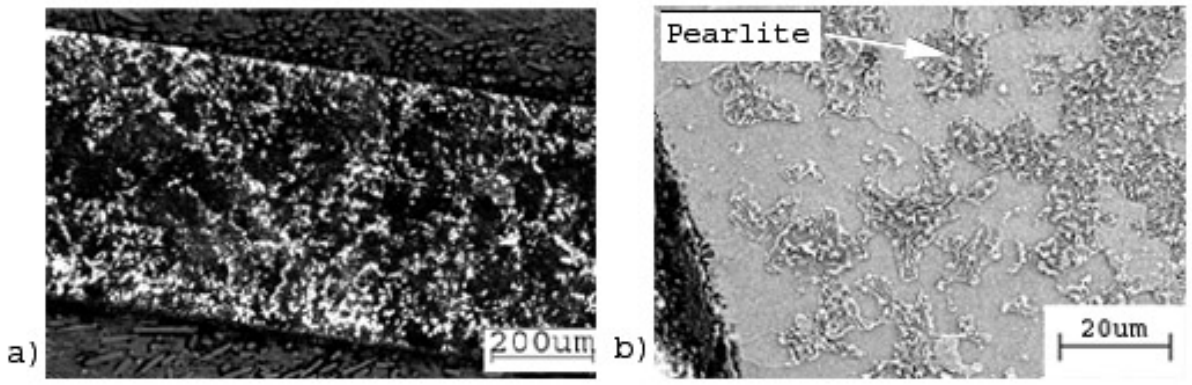

Figure 4.53: a) Optical micrograph of the cross-section and b) SEM image of the edge of an AISI 1074 sample heated to 850°C for 60 minutes in 4% H_2/Ar, showing areas of decarburization throughout the sample.

Optical micrographs of an AISI 1074 sample held for 60 minutes at 950°C are shown in Figures 4.54 a and b. Note the decarburization layer is not continuous, though diffusion channels are evident in the sample. Figure 4.55 shows a specimen heated to 1050°C for 60 minutes. A continuous decarburization layer was not observed, though a small amount of decarburized grains were noted. The largest of those observed reached a depth of approximately 5 μm.

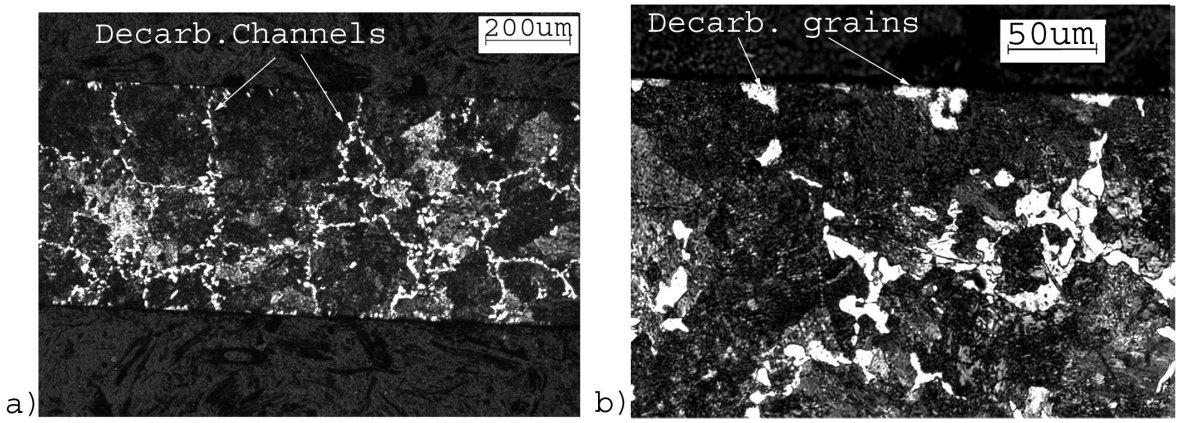

Figure 4.54: Optical micrographs of the cross-section of an AISI 1074 sample heated to 950°C for 60 minutes in 4% H_2/Ar. Decarburization channels are evident through the sample(a), and a discontinuous decarburization olayer along the edge of the sample is present(b).

The half width of the decarburized layer for specimens heat-treated for 60 minutes was measured and plotted against the temperature of heat treatment (Figure 4.56). The data exhibits a curve behavior with a maximum decarburization depth occurring at approximately 850°C. Above this temperature, the reaction as was shown in Equation 16 is not favored ($\Delta G^0 > 0$), thus carbon is not readily removed from the sample surface such that it can combine with the hydrogen in the atmosphere. At temperatures above the eutectoid temperature, the nucleation of ferrite from austenite is the dominating mechanism for microstructural evolution, while below the eutectoid temperature, the coarsening of cementite from pearlite and the dissolution of carbides become dominant, thus resulting in a smaller decarburization thickness at lower temperatures as well.

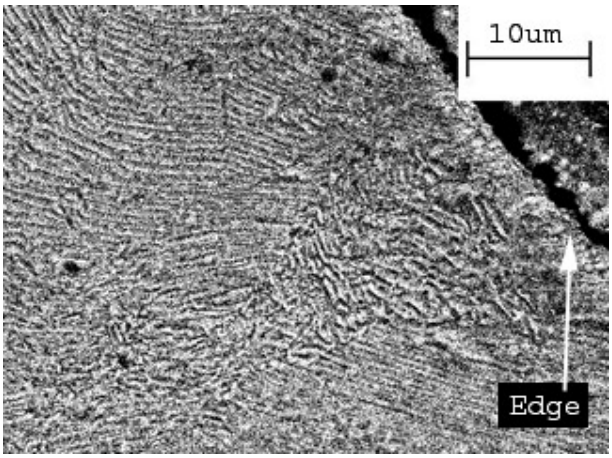

Figure 4.55: SEM image of the edge of an AISI 1074 sample heated in 4% H_2/Ar for 60 minutes at 1050°C. The micrograph does not depict any areas of decarburization, and the sample has a pearlitic microstructure.

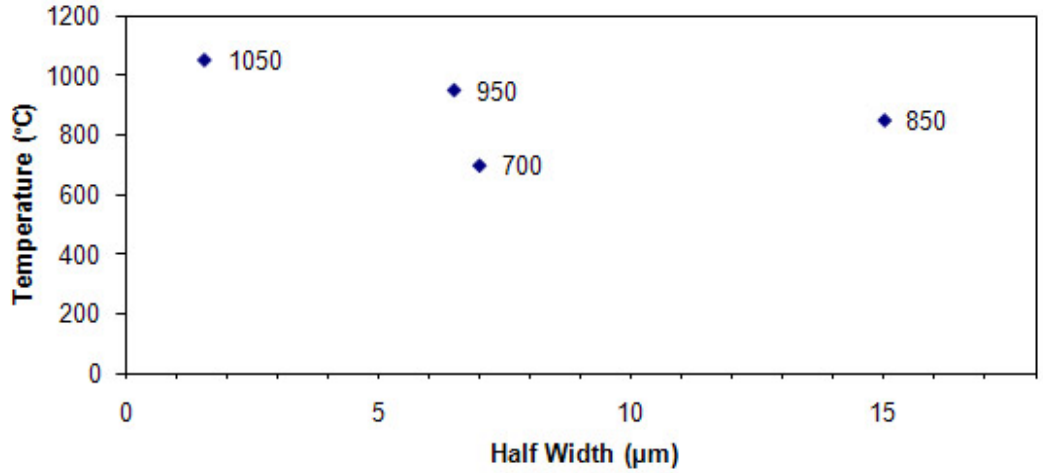

Figure 4.56: Plot of the decarburizing depth vs. temperature of AISI 1074 after heating samples for 60 minutes in 4% H_2/Ar. Below the eutectoid temperature (727°C), the dominant mechanism for microstructural evolution changes, which results in a decrease in the decarburized layer thickness.

CHAPTER V

CONCLUSIONS

In the fabrication of 4140 strip prior to carburization, it can be concluded from the research that MnO_2 powder is not reduceable under the conditions used in this study, and thus cannot be used to produce extrusions of 4140 composition. Manganese metal powder has proven to be a suitable alternative. Due to the low amounts of chromium necessary in an alloy of 4140 composition (0.8-1.1 wt%), Cr_2O_3 does not fully reduce. This is because the lower temperature, faster reduction of Fe_3O_4 creates a barrier to the diffusion of oxygen such that Cr_2O_3 cannot reduce completely. In the case of the fabrication of a 316 metal part (without carbon), full reduction is achieved, as higher amounts of chromium (16-18.5 wt%) are necessary in the alloy.

Gas carburization at high temperatures, as tested on extrusions of 4140 composition, has proven to be a successful technique for the alloying of thin-walled structures (approximately 250-300 μm thickness) with carbon. Carbon contents of up to 1.69 wt% were achieved in 30 minutes using the techniques outlined in this study. In addition, metal dusting, a catastrophic form of carburization, has been completely avoided. Reasonable compositional control near 0.4 wt% carbon, as is necessary for a 4140 alloy, has also been demonstrated in the study.

The heat treatment of 4140 samples produced through the techniques outlined in this study showed hardness values as well as microstructures comparable to conventionally produced 4140 samples that were heat-treated in the same manner. Thus, it can be concluded that the high temperature carburization process can be used for the alloying of thin-walled, low alloy steels with repeatability, and heat treatment of the parts results in mechanical and microstructural properties that are expected of a conventionally produced alloy.

Compression testing of carburized hollow spheres of 4140 composition showed greater maximum stresses upon loading than spheres tested prior to carburization. However, variations in the relative densities of the spheres result in the somewhat unpredictable mechanical behavior of each batch of spheres. Also contributing is the decarburization of the spheres upon cooling and the high degree of porosity in the sphere walls.

In the case of gas carburization at low temperatures on an alloy of 316 composition (without carbon), preliminary investigation suggests that carburization of the part has taken place, as evidenced by hardness variations through the cross-section. Unlike high temperature carburization, conditions are such that metal dusting is thermodynamically favorable. This cannot be avoided due to the temperature regime that is necessary for carburization to occur without the formation of carbides.

The results of these investigations yield a novel method for the production of steel parts of various compositions from metal oxide powders, as was the key objective of the research. It was shown that low alloy steels and more highly alloyed steels, demonstrated through the investigations of 4140 and 316 compositions, respectively, can be made using the process. The speed and low cost of the process, coupled with the proven ability of the process to yield parts with similar microstructural and mechanical characteristics as conventionally fabricated alloys, allows for the techniques presented in this study to be used for the development of steel alloys which could not be previously done economically.

CHAPTER VI

SUGGESTIONS FOR FUTURE WORK

For the formation of low alloy steels through the process described in this study, the full reduction of Cr_2O_3 has not been achieved. The use of a chromium carbide, Cr_3C_2, may prove to alleviate this problem and thus needs further investigation. Cr_3C_2 is reduceable by hydrogen, but it will be important to determine if H_2O, formed from the reduction of Fe_3O_4, oxidizes chromium particles to Cr_2O_3. Also in the formation of parts nearing 100% theoretical density, it is necessary to investigate further the extrusion of metal oxide pastes, as residual porosity in the samples in this study suggest that compaction of the paste needs to be improved. Further investigation of mechanical properties is also suggested. For example, tensile and bend tests of samples made through the process described in the study would allow for further comparison with conventionally produced parts. In order to better understand the gas carburization process, studies on the effect of residual porosity on the carburization rate would be very beneficial in determining the kinetics of the process.

In the formation of proppants, further investigations into production of the sphere prior to carburization are necessary. Large variations in relative density, wall thickness and wall integrity need to be eliminated in order to improve the mechanical behavior of the proppants. One such method that may prove useful to create more uniform spheres is the use of ultrasonic atomization as a technique for spray coating metal oxide powders onto a sacrificial core. Also, investigations of the heat treatment of strip should be extended to the hollow spheres, such that maximum loading stresses can be achieved. Because decarburization presents significant issues in the production of proppants, an investigation into the control of the CO/CO_2 atmosphere upon cooling would be very useful.

The low temperature carburization of 316 steel requires further investigation as well.

While mechanical property testing suggests that carburization has occurred, significantly higher hardness values at the surface of conventionally produced 316 carburized using a similar process has been shown in previous research. While hardness measurements can serve as an estimate to the carbon profile in a sample, a more direct technique, such as Optical Emission Spectroscopy or Auger Electron Spectroscopy should be used to determine an accurate carbon profile measurement.

In studies where hardness values greater than 1000HV have been reported in samples undergoing the LTCSS process, the successful depassivation of the Cr_2O_3 surface layer has been through the use of HCl gas, applied several times through the carburization process. Thus, it is suggested that the use of HCl gas be employed in further experimentation as means for depassivation of the Cr_2O_3 surface layer, rather than the use of electroplating, which was used in this study. In addition, further experiments should be performed such that gas carburization occurs at the highest temperatures possible during early stages, such that maximum diffusion is possible without the risk of carbide formation. For example, in this study carburization was carried out at 525°C for up to 25 hours. However, a carburization schedule beginning 600°C for 45 minutes then lowering to 525°C over 4 hours would still prevent the formation of carbides, but also allow for diffusion at higher temperatures. Because metal dusting was observed during the low temperature carburization of 316 samples in this study, it is also necessary to investigate the extent to which metal dusting occurs during this process if it is to be used with thin-walled samples. Significant metal dusting results in the loss of integrity of the part, so it is important that this be understood when designing further experiments.

Decarburization studies on low alloy steels concluded that in the case of a spheroidite microstructure, accurate modeling of the decarburization behavior is not available in the literature. Thus, further experimentation and modeling of the decarburization of steels with this microstructure should be investigated. Also, the decarburization of austenitic steels should be investigated such that the behavior of the steel can be predicted through the

entire carburization process.

REFERENCES

[1] J.H. Nadler, T.H. Sanders Jr, and R.F. Speyer. Oxide reduction and sintering of Fe-Cr alloy honeycombs. *Journal of Materials Research*, 18(8):1787–1794, Aug 2003.

[2] J.H. Nadler, T.H. Sanders Jr, J.K. Cochran, and S.S. Kim. Oxide reduction and diffusion of Fe-Cr alloy honeycombs. *Journal of Physics IV France*, 120:47–54, 2004.

[3] J. Nadler. *The hydrogen reduction of iron and chromium oxides*. PhD thesis, Georgia Institute of Technology, 2003.

[4] B.C. Church, T. Sanders Jr., R. Speyer, and J. Cochran. Interconnect thermal expansion matching to solid oxide fuel cells. *Journal of Materials Science*, 40:4893–4898, 2005.

[5] B. Church. *Fabrication and characterization of solid oxide fuel cell interconnect alloys*. PhD thesis, Georgia Institute of Technology, 2004.

[6] J.K. Cochran, K.J. Lee, D. McDowell, and T.H. Sanders Jr. Multifunctional metallic honeycombs by thermal chemical processing. In A. Ghosh, T.H. Sanders Jr., and D. Claar, editors, *Processing and Properties of Lightweight Cellular Metals and Structures*, pages 127–136. TMS, 2002.

[7] K.M. Hurysz, R. Oh, J.K. Cochran, T.H. Sanders Jr, and K.J. Lee. Modeling powder extrusion pastes for forming light weight multifunctional structures. In A. Ghosh, T.H. Sanders Jr., and D. Claar, editors, *Processing and Properties of Lightweight Cellular Metals and Structures*, pages 167–176. TMS, 2002.

[8] J.L. Clark, J.K. Cochran, T.H. Sanders Jr, and K.J. Lee. Metal honeycomb from oxide paste: Maraging steel and super invar structure and properties. In A. Ghosh, T.H. Sanders Jr., and D. Claar, editors, *Processing and Properties of Lightweight Cellular Metals and Structures*, pages 137–146. TMS, 2002.

[9] D. Mader. *Hydraulic proppant fracturing and gravel packing*. Elsevier, 1989.

[10] T. Nasu, K. Tokumitsu, T. Konno, and K. Suzuki. Reduction of iron-oxide by ball-milling with hydrogen gas flow. *Materials Science Forum*, 343-346:435–440, 2000.

[11] R.J. Pollard. Hydrogen reduction of fine iron-oxide particles. *Hyperfine Interactions*, 40:417–420, 1988.

[12] F.D. Richardson and J.H.E. Jeffes. The thermodynamics of substances of interest in iron and steel making from 0°C to 2400°C. *Journal of the Iron and Steel Institute*, pages 261–270, Nov 1948.

[13] H.J.T. Ellingham. Reducibility of oxides and sulphides in metallurgical processes. *Journal of the Society of Chemical Industry*, 63:125–133, 1944.

[14] A. Pineau, N. Kanari, and I. Gaballah. Kinetics of reduction of iron oxides by H_2 Part I: Low temperature reduction of hematite. *Thermochimica acta*, 447(1):89–100, 2006.

[15] A. Pineau, N. Kanari, and I. Gaballah. Kinetics of reduction of iron oxides by H_2 Part II: Low temperature reduction of magnetite. *Thermochimica acta*, 456(1):75–88, 2007.

[16] K. Piotrowski, K. Mondal, H. Lorethova, L. Stonawski, T. Szymański, and T. Wiltowski. Effect of gas composition on the kinetics of iron oxide reduction in a hydrogen production process. *International Journal of Hydrogen Energy*, 30(15):1543–1554, 2005.

[17] S. Hayashi and Y. Iguchi. Influence of several factors on synthesis of iron carbide from iron ore. *Ironmaking & Steelmaking*, 27(2):111–116, 2000.

[18] M.M. Khader, B.E. El-Anadouli, E. El-Nagar, and B.G. Ateya. Kinetics of the reduction of Fe_2O_3 with hydrogen. *Journal of Solid State Chemistry*, 93:283–290, 1991.

[19] D.R. Gaskell. *Introduction to the thermodynamics of materials*. Taylor and Francis, Washington, DC, third edition, 1995.

[20] O. Kubschewski and C.B. Alcock. *Metallurgical thermochemistry*. Robert Maxwell, M.C., New York, NY, fifth edition, 1956.

[21] M. Khedr. Isothermal reduction kinetics of Fe_2O_3 mixed with 1-10% Cr_2O_3 at 1173-1473K. *ISIJ International*, 40(4):309–314, 2000.

[22] T. Takayama and N. Hamasaka. High surface pressure resistant steel parts and methods of producing same. *US Patent 6447619*, Sep 2002.

[23] H. Onoe. High strength screw. *US Patent 6386810*, May 2002.

[24] H. Deimel. Base material for producing blades for circular saws, cutting-off wheels, mill saws as well as cutting and scraping devices. *US Patent 6375762*, April 2002.

[25] J.K. Stanley. Steel carburization and decarburization. A theoretical analysis. Part I. *Iron Age*, 151(3):31–35, Jan 1943.

[26] K. Palaniradja, N. Alagumurthi, and V. Soundararajan. Optimization of process variables in gas carburizing process- an experimental investigation with AISI 3310 steel material. *Materials and Manufacturing Processes*, 21:111–113, 2006.

[27] K. Palaniradja, N. Alagumurthi, and V. Soundararajan. Optimization of process variables in gas carburizing process: A taguchi study with experimental investigation on SAE 8620 and AISI 3310 steels. *Turkish Journal of Engineering and Environmental Science*, 29:279–284, 2005.

[28] G. Matamala and P. Cañete. Carburization and decarburization kinetics of iron in CH_4-H_2 mixtures between 1000-1100°C. *Materials and Manufacturing Processes*, 21:111–113, 2006.

[29] V.A. Munts and A.P. Baskakov. Rate of carburizing of steel. *Metal Science and Heat Treatment*, 22(5):358–360, 1981.

[30] S. Forseth and P. Kofstad. Carburization of Fe-Ni-Cr steels in CH_4-H_2 mixtures at 850-1000°C. *Materials and Corrosion*, 49:266–271, 1998.

[31] G. Tibbetts. Diffusivity of carbon in iron and steels at high temperatures. *Journal of Applied Physics*, 51(9):4813–4816, Sep 1980.

[32] J.K. Stanley. Steel carburization and decarburization. A theoretical analysis. Part II. *Iron Age*, 151(4):49–55, Feb 1943.

[33] K.E. Blazek and J.R. Cost. Carbon diffusivity in iron-chromium alloys. *Japan Institute of Metals, Transactions*, 17:630–636, 1976.

[34] W.D. Callister, Jr. *Materials science and engineering: An introduction*. John Wiley & Sons, 2000.

[35] J.P. Schaffer, A. Saxena, S. Antolovish, T. H. Sanders Jr., and S. Warner. *The Science and Design of Engineering Materials*. Boston, MA, second edition, 1999.

[36] ASM Committee on Gas Carburizing. *Gas Carburizing*. American Society for Metals, Metals Park, OH, 1964.

[37] O.K. Rowan and R.D. Sisson Jr. Effect of alloy composition on carburizing performance of steel. *Journal of Phase Equilibria and Diffusion*, 30(3):235–241, 2009.

[38] R.P. Smith. Equilibrium of Iron-Carbon Alloys with Mixtures ofCO-CO_2 and CH_4-H_2. *Journal of the American Chemical Society*, 68(7):1163–1175, 1946.

[39] H. Dunwald and C. Wagner. Thermodynamic Investigations on the System Iron-Carbon-Oxygen. *Z. anorg. allgem. Chem*, 199:321–346, 1931.

[40] A. Bramley and H.D. Lord. The equilibria between mixtures of carbon monoxide and carbon dioxide at various pressures in contact with steels of different carbon concentrations at 750–1150°C. *Journal of the Chemical Society (Resumed)*, 1932:1641–1669, 1932.

[41] M.L. Becker and B. Met. Carburising and graphitising reactions between iron-carbon alloys, carbon monoxide and carbon dioxide. *Journal of the Iron and Steel Institute*, 1930.

[42] A. Johansson and R. von Seth. The carburization and decarburization of iron and some investigations on the surface decarburization of steel. *Journal of the Iron and Steel Institute*, pages 295–352, 1926.

[43] G. Takahashi. On the equilibrium between austenite and the carbon oxides. *Tohoku Imperial University Science Reports*, 15:157–175, 1926.

[44] H.J. Grabke. Mechanisms and prevention of corrosion of carbonaceous gases. *Materials Science Forum*, 369-372:101–108, 2001.

[45] T. Christiansen and M.A.J Somers. Low temperature gaseous nitriding and carburising of stainless steel. *Surface Engineering*, 21(5-6):445–455, 2005.

[46] F.J. Martin, E.J. Lemieux, T.M. Newbauer, R.A. Bayles, P.M. Natishan, G.M. Kahn, H.and Michal, F. Ernst, and A.H. Heuer. Carburization-induced passivity of 316L austenitic stainless steel. *Electrochemical and Solid-State Letters*, 10(12):C76–C78, 2007.

[47] G.M. Michal, F. Ernst, H. Kahn, Y. Cao, F. Oba, N. Agarwal, and A.H. Heuer. Carbon supersaturation due to paraequilibrium carburization: Stainless steels with greatly improved mechanical properties. *Acta Materialia*, 54:1597–1606, 2006.

[48] F.J. Martin, P.M. Natishan, E.J. Lemieux, T.M. Newbauer, R.J. Rayne, R.A. Bayles, H. Kahn, G.M. Michal, F. Ernst, and A.H. Heuer. Enhanced corrosion resistance of stainless steel carburized at low temperature. *Metallurgical and Materials Transactions A*, 40(8):1805–1810, 2009.

[49] S. Collins and P. Williams. Low-Temperature Colossal Supersaturation. *Advanced Materials and Processes*, 164(9):32–34, 2006.

[50] G.M. Michal, X. Gu, W.D. Jennings, H. Kahn, F. Ernst, and A.H. Heuer. Paraequilibrium carburization of duplex and ferritic stainless steels. *Metallurgical and Materials Transactions A*, 40(8):1781–1790, 2009.

[51] P.C. Williams and S.V. Marx. Modified low temperature case hardening processes. *US Patent 6547888*, Apr 2003.

[52] P.C. Williams and S.V. Marx. Low temperature case hardening processes. *US Patent 6461448*, Oct 2002.

[53] P.C. Williams and S.V. Marx. Selective case hardening processes at low temperature. *US Patent 6165597*, Dec 2000.

[54] F. Ernst, A. Avishai, H. Kahn, X. Gu, GM Michal, and AH Heuer. Enhanced carbon diffusion in austenitic stainless steel carburized at low temperature. *Metallurgical and Materials Transactions A*, 40(8):1768–1780, 2009.

[55] E. Pippel, J. Woltersdorf, H.J. Grabke, and S. Straub. Microprocesses of metal dusting on iron. *Steel Research*, 66(5):217–221, 1995.

[56] H.J. Grabke, R. Krajak, and J.C. Nava Paz. On the mechanism of catastrophic carburization: Metal dusting. *Corrosion Science*, 35(5-8):1141–1150, 1993.

[57] R.F. Hochman. Catastrophic deterioration of high temperature alloys in carbonaceous atmospheres. In *Symposium on Properties of High Temperature Alloys with Emphasis on Environmental Effects, Las Vegas, Nev; United States*, pages 715–732. Princeton, N. J, Electrochemical Society, Inc., 1976.

[58] R.F. Hochman. Basic studies of metal deterioration ("metal dusting") in carbonaceous environments at elevated temperatures. In *Proceedings of the Fourth International Congress on Metal Corrosion, NACE, Houston*, page 258, 1972.

[59] H.J. Grabke, C.B. Bracho-Troconis, and E.M. Muller-Lorenz. Metal dusting of low alloy steels. *Materials and Corrosion*, 45(4):215–221.

[60] H.J. Grabke. Metal dusting of low-and high-alloy steels. *Corrosion*, 51(09), 1995.

[61] R. Yin. Thermodynamic aspects of iron in metal dusting. *Oxidation of Metals*, 60(1-2):103–116, Aug 2003.

[62] C.M. Chun, J.D. Mumford, and T.A. Ramanarayanan. Mechanisms of metal dusting corrosion of iron. *Journal of the Electrochemical Society*, 149(7):B348–B355, 2002.

[63] H.J. Grabke and E. M. Muller-Lorez. Effect of sulfur on the stability of cementite. *Steel Research*, 66(6):254–258, 1995.

[64] H.J. Grabke. Thermodynamics, mechanisms and kinetics of metal dusting. *Materials and Corrosion*, 49:303–308, 1998.

[65] S.R. Shatynski. The thermochemistry of transition metal carbides. *Oxidation of Metals*, 13(2):105–118, 1979.

[66] C.M. Chun and T.A. Ramanarayanan. Metal dusting corrosion of austenitic 304 stainless steel. *Journal of the Electrochemical Society*, 152(5):B169–B177, 2005.

[67] J. Zhang, A. Schneider, and G. Inden. Initiation and growth of iron metal dusting in CO-H_2-H_2O gas mixtures. *Corrosion Science*, 50:1020–1034, 2008.

[68] J.A. Colwell and R.A. Rapp. Reactions of Fe-Cr and Ni-Cr alloys in CO/CO_2 gases at 850 and 950°C. *Metallurgical Transactions A*, 17A:1065–1074, 1986.

[69] H.J. Grabke, D. Moszynski, E.M. Muller-Lorenz, and A. Schneider. Role of sulphur in carburization, carbide formation and metal dusting of iron. *Surface and Interface Analysis*, 34(1):369–374, 2002.

[70] M. Maier and J.F. Norton. Studies concerned with the metal dusting of Fe-Cr-Ni materials. *Corossion*, 1999.

[71] N. Birks. Mechanism of decarburization. In *Decarburization*, pages 1–12. Iron and Steel Institute, 1969.

[72] M. McKimpson and P.G. Shewmon. Initial hydrogen attack kinetics in a carbon steel. *Metallurgical Transactions A*, 12A:825–834, 1981.

[73] K.M. Marra, E.A. Alvarenga, and V.T.L Buono. Decarburization kinetics during annealing of a semi-processed electrical steel. *ISIJ International*, 44(3):618–622, 2004.

[74] K. Sachs. Decarburization–Definition and measurement. In *Decarburization*, pages 13–33. Iron and Steel Institute, 1969.

[75] M. Haiduga and H. Kucera. Oxidation and decarburization of Fe-Cr-C steels at high temperatures. *Defect and Diffusion Forum*, 66-69:1383–1388, 1989.

[76] M. Nomura, H. Morimoto, and M. Toyama. Calculation of ferrite decarburizing depth, considering chemical composition of steel and heating condition. *ISIJ International*, 40(6):619–623, 2000.

[77] R. Smith. The diffusivity and solubility of carbon in alpha-iron. *Transactions of the Metallurgical Society of AIME*, 224:105–111, Feb 1962.

[78] H.B. Aaron. Precipitate dissolution and its dependence on growth mode. *Acta Metallurgica*, 17:407–418, Apr 1969.

[79] H.B. Aaron and G.R. Kotler. The effects of curvature on the dissolution kinetics of spherical precipitates. *Metal Science Journal*, 4:222–225, 1970.

[80] J. Agren. Kinetics of carbide dissolution. *Scandinavian Journal of Metallurgy*, 19:2–8, 1990.

[81] H.B. Aaron and G.R. Kotler. Second phase dissolution. *Metallurgical Transactions*, 2:393–408, Feb 1971.

[82] R.R. Judd and H.W. Paxton. Kinetics of austenite formation from a spheroidized ferrite-carbide aggregate. *Transaction sof the Metallurgical Society AIME*, 242(2), 1968.

[83] G. Krauss. *Steels. Processing, Structure, and Performance*. ASM International, Materials Park, OH, 2005.

[84] H. Bhadeshia and R. Honeycombe. *Steels. Microstructure and Properties*. Elsevier, Burlington, MA, third edition, 2006.

[85] H.E. Boyer. Atlas of isothermal transformation and cooling transformation diagrams. 1977.

[86] J.R. Davis. *Metals handbook*. ASM International, 1998.

[87] P. Marshall. *Austenitic stainless steels: Microstructure and mechanical properties*. Springer, 1984.

[88] G.V. Raynor and V.G. Rivlin. Phase equilibria in iron ternary alloys (phase diagrams of ternary iron alloys) IV. *The Institute of Metals,*, page 485, 1988.

[89] R.F. Speyer. *Thermal analysis of materials*. CRC, 1994.